

Investigation of Pressure Assisted Nanosilver Sintering Process for Application in Power Electronics

Zhang, Hao

DOI

[10.4233/uuid:49ccc901-a128-424f-9e9d-e2f8c63ad31b](https://doi.org/10.4233/uuid:49ccc901-a128-424f-9e9d-e2f8c63ad31b)

Publication date

2019

Document Version

Final published version

Citation (APA)

Zhang, H. (2019). *Investigation of Pressure Assisted Nanosilver Sintering Process for Application in Power Electronics*. [Dissertation (TU Delft), Delft University of Technology]. <https://doi.org/10.4233/uuid:49ccc901-a128-424f-9e9d-e2f8c63ad31b>

Important note

To cite this publication, please use the final published version (if applicable). Please check the document version above.

Copyright

Other than for strictly personal use, it is not permitted to download, forward or distribute the text or part of it, without the consent of the author(s) and/or copyright holder(s), unless the work is under an open content license such as Creative Commons.

Takedown policy

Please contact us and provide details if you believe this document breaches copyrights. We will remove access to the work immediately and investigate your claim.

**INVESTIGATION OF PRESSURE ASSISTED NANOSILVER
SINTERING PROCESS FOR APPLICATION
IN POWER ELECTRONICS**

INVESTIGATION OF PRESSURE ASSISTED NANOSILVER SINTERING PROCESS FOR APPLICATION IN POWER ELECTRONICS

Proefschrift

ter verkrijging van de graad van doctor
aan de Technische Universiteit Delft,
op gezag van de Rector Magnificus Prof. dr. ir. T.H.J.J. van der Hagen,
voorzitter van het College voor Promoties,
in het openbaar te verdedigen op
dinsdag 25 juni 2019 om 15:00 uur

door

Hao ZHANG

Master of Engineering in Materials Processing Engineering
Harbin University of Science and Technology, China
geboren te Changtu, China

Dit proefschrift is goedgekeurd door de:

Promotor: Prof. dr. G.Q. Zhang

Promotor: Prof. dr. ir. W.D. van Driel

Samenstelling promotiecommissie:

Rector Magnificus,	voorzitter
Prof. dr. G.Q. Zhang,	Technische Universiteit Delft
Prof. dr. ir. W.D. van Driel,	Technische Universiteit Delft

Onafhankelijke leden:

Prof. dr. F.L. Sun	Harbin University of Science and Technology
Prof. dr. X.J. Fan	Lamar University
Prof. dr. H. Fremont	University of Bordeaux
Prof. dr. ir. K.M.B. Jansen,	Technische Universiteit Delft
Dr. ir. R.H. Poelma	Nexperia B.V.

Reserve:

Prof. dr. M. Zeman	Technische Universiteit Delft
--------------------	-------------------------------



Keywords: nanosilver sintering, pressure, shear strength, nanoindentation, stress distribution

Printed by: IPSKAMP Printing

Copyright © 2019 by Hao Zhang

ISBN: 978-94-6366-176-8

An electronic version of this dissertation is available at

<http://repository.tudelft.nl/>.

To my parents

CONTENTS

1	Introduction	1
1.1	Background	1
1.2	Review of die attach technologies	3
1.2.1	Lead free soldering technology	3
1.2.2	Transient liquid phase bonding	6
1.2.3	Silver sintering technology	8
1.2.4	Comparison of three main die attach technologies	12
1.3	Research objectives	14
1.4	Thesis outline	15
	References	16
2	Bonding mechanisms analysis of nanosilver sandwich sintered package	28
2.1	Introduction	29
2.2	Methodology	30
2.3	Effects of pressure on the mechanical properties	31
2.4	Effects of temperature on the mechanical properties	35
2.5	Effects of time on the shear mechanical properties	37
2.6	Densification mechanisms of silver nanoparticles	39
2.7	Summary	40
	References	41
3	Micro mechanical properties of pressure sintered nanosilver joint	45
3.1	Introduction	46
3.2	Methodology	47
3.3	Effects of strain rate on the indentation hardness	48
3.4	Plastic stress-strain constitutive model at room temperature	49
3.5	Effects of temperature on the micro mechanical properties	50
3.5.1	Evolution of indentation depth	50
3.5.2	Temperature dependence of hardness	52
3.5.3	Temperature dependence of elastic modulus	53
3.6	Initial creep behavior of nanosilver sintered joint	55
3.7	Summary	56
	References	56

4	Mechanical properties of nanosilver double side sintered package	61
4.1	Introduction	62
4.2	Methodology	64
4.3	Characterization of sintered nanosilver film	66
4.3.1	Pressure-free sintered nanosilver film	66
4.3.2	Comparison of sintered silver nanoparticles	68
4.4	Effects of sintering pressure on the shear strength	68
4.5	Effects of sintering pressure on the fracture morphology	70
4.6	Summary	73
	References	73
5	Stress analysis of nanosilver double side sintered package using FEA method	78
5.1	Introduction	79
5.2	Experimental set-up	80
5.3	Simulation model	82
5.4	Results experiments	84
5.5	Results simulations	86
5.6	Summary	90
	References	90
6	Application of nanosilver sintering in ceramic packages	95
6.1	Introduction	96
6.2	Experimental set-up	97
6.3	Simulation methodology	98
6.4	Evaluation of bonding quality	100
6.5	Stress distribution analysis of sintered cavity	102
6.6	Summary	105
	References	106
7	Conclusions and recommendations	111
7.1	Conclusions	111
7.2	Recommendations	113
	Summary	116
	Samenvatting	119
	Acknowledgements	123
	List of Publications	127
	Curriculum Vitæ	128

1

INTRODUCTION

1.1. BACKGROUND

Power electronics are the applications of solid state electrical devices whose primary function is to converse, control and process electric power [1-3]. Until now, the commercially available power electronic devices in the market are mainly silicon (Si) based, which has a limited operation temperature and power density around 175°C and 200 W/cm², respectively [4, 5]. However, wide band gap semiconductors, which are typically represented by silicon carbide (SiC) and gallium nitride (GaN), have been extensively investigated for power electronic packages and modules in the past few years [6, 7]. These semiconductors offer larger band gap, higher break down voltage and operation temperature when compared with Si based semiconductors. The GaN power electronic devices are mainly used for low voltage devices (600 V), due to its growth dependence on Si, SiC, or sapphire substrates [8, 9]. In contrast, the SiC power electronic packages and modules are designed for medium to high voltage (1.2 kV-20 kV) applications, such as bipolar junction transistors (BJTs), metal oxide semiconductor field effect transistor (MOSFETs), diodes, and insulated gate bipolar transistor (IGBT) [9, 10]. The major applications of power electronic packages and modules are shown in Figure 1.1. Along with the development of wide band gap semiconductors, advanced packaging methods and technologies are also needed to meet the new demands resulted from the operation process.

Increasing demands for power electronic packages and modules have been proposed to be higher in efficiency (>200 kHz), higher in voltage (>1.2 kV), and capable of operating at temperatures over 350°C [11, 12]. The interface between the power chip and its application circuit is always given by die attach layer. This layer provides the stable mechanical adhesion, internal stress compensation, heat dissipation, and electrical connection within the package [13]. Therefore, the die attach layer plays an important role to ensure the entire system works consistently. Figure 1.2(a) is the schematic

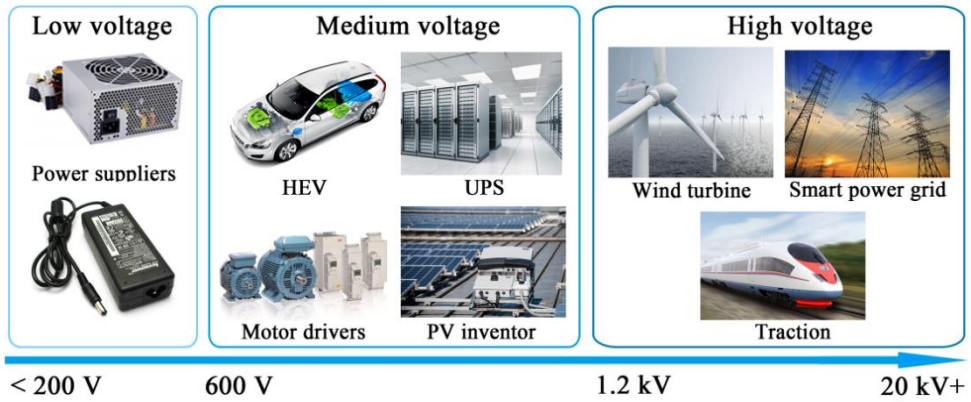


Figure 1.1: Major applications of power electronic devices

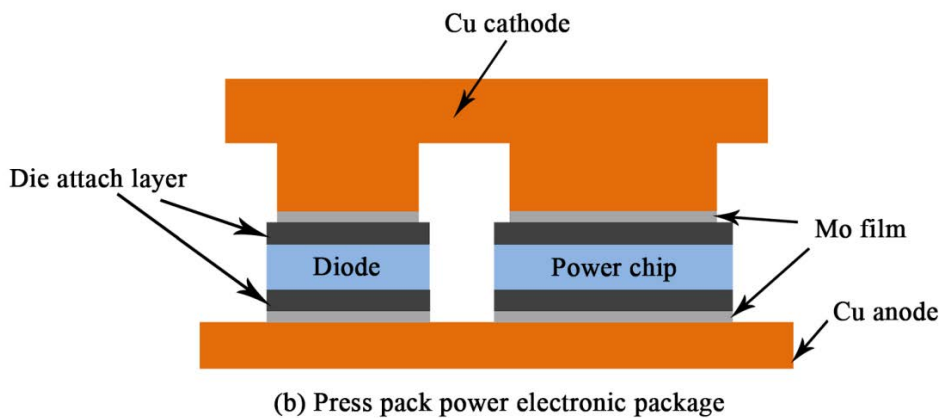
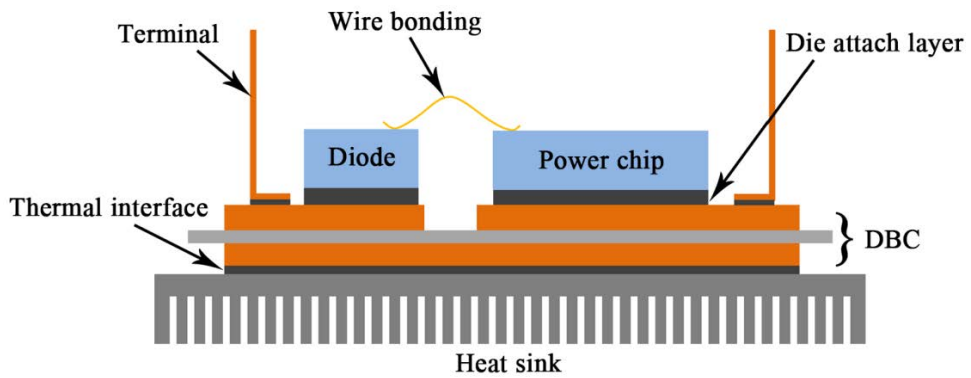


Figure 1.2: Schematic diagrams of wire bonding and press pack package (not drawn to scale)

diagram of mainstream power electronic with wire bonding technology. The power die and DBC (Direct Bond Copper) are bonded by die attach layer, and the main function of die attach layer in this structure is heat dissipation. But the wire-bonded power electronic package has high failure rate resulted from the bondwire and solder layer connections of internal chips [14, 15]. In comparison, the die attach layer in press pack power electronic package is responsible for both thermal and electrical conduction, as seen in Figure 1.2(b). The press pack power module is mainly used for high current density areas because of its higher reliability and better cooling capability when comparing with the wire-bonded package [14].

In the following section, the three main die attach technologies used for power packages, which are i) lead free soldering, ii) transient liquid phase (TLP) bonding and iii) silver sintering, are respectively reviewed in detail. Firstly, the fabrication process of die attach material is introduced. Then the processing technologies are discussed accordingly. Thirdly, the properties of typical materials used for each technology is summarized. Finally, a general comparison of lead free soldering, TLP bonding and silver sintering is given.

1.2. REVIEW OF DIE ATTACH TECHNOLOGIES

1.2.1. LEAD FREE SOLDERING TECHNOLOGY

The high lead (Pb) based solder alloys, with more than 85 wt% (by weight percentage, wt%) of Pb element and melting temperatures around 300°C, have historically been used as die attach materials for power electronic packages and modules [16]. Among which, Pb-5Sn-2.5Ag solder alloy has been used in the industry for decades as a standard die attach material, offering high melting temperature, acceptable thermal conductivity (23 W/(m·K)) and electrical conductivity ($0.35 \times 10^7 / (\Omega \cdot \text{m})$) [4]. However, the toxicity of lead in solder alloys limited their wide application, which resulted in the development of lead free solder alloys.

Lead free solders, typically referring to Sn based solder alloys, have been applied for low power electronic packages and modules. The Sn-Ag-Cu (SAC) lead free solders have been proven to be suitable for Si based low power devices, due to their favorable wettability and mechanical properties [17-19]. However, the operation temperature of SiC based power modules can reach more than 200°C, which indicates that these lead free solders are no longer applicable. Gold (Au) based high temperature lead-free solders with melting temperature above 280°C have been widely used as die attach materials in high power devices. While several disadvantages of Au based solder alloys are known, such as the high cost, coarsening of microstructure, brittle nature of interfacial

intermetallic compounds (IMCs) and void issues, especially for the purpose of attaching large dies [19].

FABRICATION OF LEAD FREE SOLDERS

Solder paste is one of the most widely used forms of solder alloys for electronic assembling and it is usually mixed by solder powders and corresponding flux. The gained paste can be printed or dispensed on various substrates, such as DBC (Direct Bond Copper) and AMB (Active Metal Brazing). However, the limitation of stencil thickness, as well as the contamination of flux evaporation, restricts the application of solder paste in some occasions, especially for press pack packages.

Solder preform is one of the most potential candidates for jointing various dies, substrates and lead frames. The solder preform is usually described as a two-dimensional film or sheet with ultrathin thickness. Solder preforms show many advantages over solder paste, such as high accuracy in thickness distribution after soldering, flux free processing, and repeatable production with complex sizes and shapes [20]. The fabrication process of solder preform is presented in Figure 1.3, which mainly consists of three steps: casting, rolling and stamping [21]. The molten solder is first poured into the mold and the solder ingot is obtained after cooling down to room temperature, as shown in Figure 1.3(a). Then the solder ingot is rolled into thin sheet with various thicknesses via adjusting the distance between two rollers, as indicated in Figure 1.3(b). The solder sheet is furtherly punched into small pieces according to the dimension of solder pad and the schematic diagram is shown in Figure 1.3(c). The complicated shapes of preform can be gained by the designing of mold.

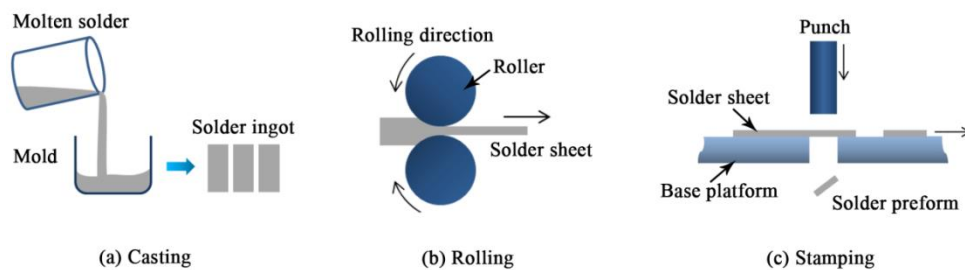


Figure 1.3: Schematic diagrams of solder preform fabrication (not drawn to scale)

LEAD FREE SOLDERING PROCESS

Currently, several technologies have been developed for soldering process, such as reflow soldering, ultrasonic soldering, laser soldering, wave soldering, induction soldering [22].

The reflow soldering is regarded as the primary processing method for attaching power dies on substrate. Normally, prior to the reflow soldering, the solder paste / preform is first printed or dispensed / placed on the DBC, and then the die is placed onto the solder paste / preform. The reflow process usually consists of four continuous processes: preheating, soaking, reflow and cooling. Firstly, the assembled die/solder/DBC is quickly heated up from room temperature in the preheating step. During soaking process, the flux inside the paste begins to evaporate and removes the oxidation layer on the surfaces of solders and bonding pads. Then the solder is melting to form a liquid, and wet on bonding pads in the reflow process. Finally, the bonded package will be cooled down to room temperature in the cooling process.

During reflow, chemical reactions occur between the Sn based lead-free solder alloys and coating materials on substrate, such as Cu, Ni, Ag, and Au, and result in the formation of intermetallic compounds (IMCs) at the interface [23, 24]. It is well known that the presence of IMCs between solder alloys and substrate provides a good metallurgical bonding. However, an excessive layer of IMCs at the interface may cause reliability problems due to the brittleness of IMCs and their tendency to form defects [23, 25].

HIGH TEMPERATURE LEAD FREE SOLDER ALLOYS

Various lead free solders have been explored for high temperature applications with high thermal conductivity and reliability. The typical high melting temperature solders are represented by Sn-5Sb [26, 27], Au-20Sn [28, 29], Au-12Ge [30, 31], Au-3.2Si [32], Bi-Ag-X [33-35], Al-Zn-Mg [36], Al-Zn-Ge [36, 37] and Al-Zn-Cu [38], details are summarized in Table 1.1. Among which, the Au-20Sn eutectic solder alloy has been extensively applied in power electronic packages modules, due to its advantages of high electrical ($1.64 \times 10^{-7} / (\Omega \cdot m)$ [28]) and thermal conductivity (57 W/(m·K) [29, 39]), superior high temperature reliability, and possibility of flux free soldering [40, 41]. According to Au-Sn phase diagram, stable intermetallic compounds (IMCs) including Au_5Sn , AuSn, $AuSn_2$, $AuSn_4$ are formed at room temperature [16, 42], and Au_5Sn and AuSn are the two intermetallic compounds at the eutectic point. However, the high cost and poor resistance to thermomechanical stress also limited the application of Au-20Sn eutectic solder alloy [43].

Table 1.1: Summary of lead free solders used in power electronic packages and modules

Solder (wt%)	Bonding temp. (°C)*	Re-melting temp. (°C)**	Thermal conductivity W/(m·K)	CTE 10 ⁻⁶ K ⁻¹	Ref.
Sn-5Sb	245+30	245	28	27	[26, 27]
Au-20Sn	278+30	278	57	18	[29, 39]
Au-12Ge	356+30	356	52	12	[30]
Au-3.2Si	363+30	363	27	12	[32]
BiAgX	265+30	265	-	15.4	[33]
Zn-Al-Mg	350+30	350	42.94	23.58	[36]
Zn-Al-Ge	362+30	362	60.46	20.03	[36]
Zn-Al-Cu	~380+30	~380	-	-	[38]

*Bonding temperature is 30~50°C higher than the liquid temperature

**Only slight increase is induced due to the formation of small amount of IMCs in solder bulk

1.2.2. TRANSIENT LIQUID PHASE BONDING

Following the traditional soldering technology, transient liquid phase (TLP) bonding or termed as solid-liquid interdiffusion (SLID) bonding has been developed and offers low bonding temperature (around 250°C), flux free joining and high temperature reliability [44, 45]. The TLP bonding technology consists of at least one low and one high melting temperature metal, or a solder alloy with special designed constituent. After TLP bonding process, full IMCs are formed within the whole die attach layer. The formation of IMCs between die and substrate provides a stable bonding when they services at temperatures higher than the processing temperature [46]. However, the TLP bonding is a time-consuming process time due to the required isothermal solidification and sufficient bond homogenization, which usually takes more than 30 min per process [47]. In addition, and the evolution of formed IMCs will cause performance issues in the service process.

PREPARATION OF METAL LAYERS

There are three main methods used for fabricating the intermediate layers for TLP bonding. The first one is the solder preform with designed compositions according to the

phase diagram. The preform can be prepared by applying the similar method as described in section 1.2.1. The second method is depositing several single metal layers on the die backside or on the top of substrate or on both two areas. Comparing with physical vapor deposition (PVD) method, the metal layers fabricated by electroplating method are more simple and cost effective, and the gained layer structure is reproducible and uniform [44]. The third method uses the mixed pure metal powders (average diameter of 5–20 μm) which consist of a lower melting temperature one and a higher melting temperature one [48, 49]. The powders will be firstly mixed with certain amount of organics to form paste and then it can be printed or dispensed on substrate.

TLP BONDING PROCESS

The TLP bonding process (taking Cu-Sn system as an example) can be achieved by several steps [50], as shown in Figure 1.4. Firstly, the Cu substrates and Sn layer are brought into contact, and then certain heat and pressure are applied. Secondly, the bonding process occurs when heating temperature upon the melting temperature of Sn. Once reached, the molten Sn diffuses and reacts with Cu, and results in the formation of IMCs (mainly Cu_6Sn_5) at the interface. Vacuum or inert gas may also be needed for promoting the diffusion of Sn. Thirdly, the isothermal solidification process is needed to ensure the complete formation of IMCs within the whole joint. The final joint consists of two main phases: Cu_6Sn_5 and Cu_3Sn , with melting temperature of 415°C and 676°C, respectively. Therefore, the re-melting temperature of TLP bonded joint is expected to increase from 232°C (Sn) to 415°C (Cu_6Sn_5).

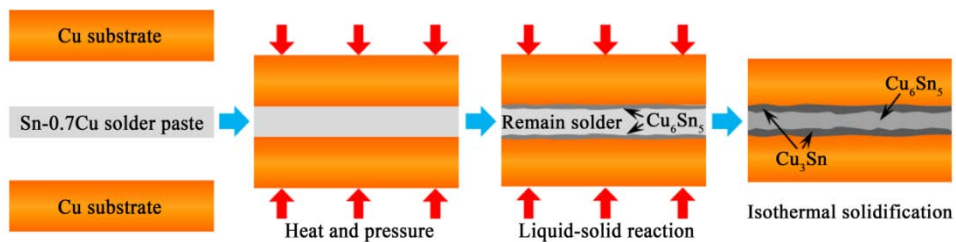


Figure 1.4: Schematic diagram of Cu-Sn TLP bonding process

MATERIALS FOR TLP BONDING

Different TLP bonding systems have been developed for attaching power die, such as Ag-In [51], Sn-Cu [52], Sn-Ag [53], Au-In [54, 55], Sn-Au [56], Cu-In [55] and Sn-Ni [57]. Figure 1.5 summarizes the temperature changes during TLP bonding process. Among the material systems, the Si-Ni system gained the highest re-melting temperature of 794°C

after bonding, which consists of Ni_3Sn_4 and residual Ni. Besides, the Sn-Ni system got the highest increase of melting temperature (re-melting temp. minus first melting temp.). Besides, comparable electrical performances were gained for Sn-Ni TLP bonded IGBTs and commercial soldering ones [57]. The comprehensive comparison of various TLP bonding processes is summarized in Table 1.2.

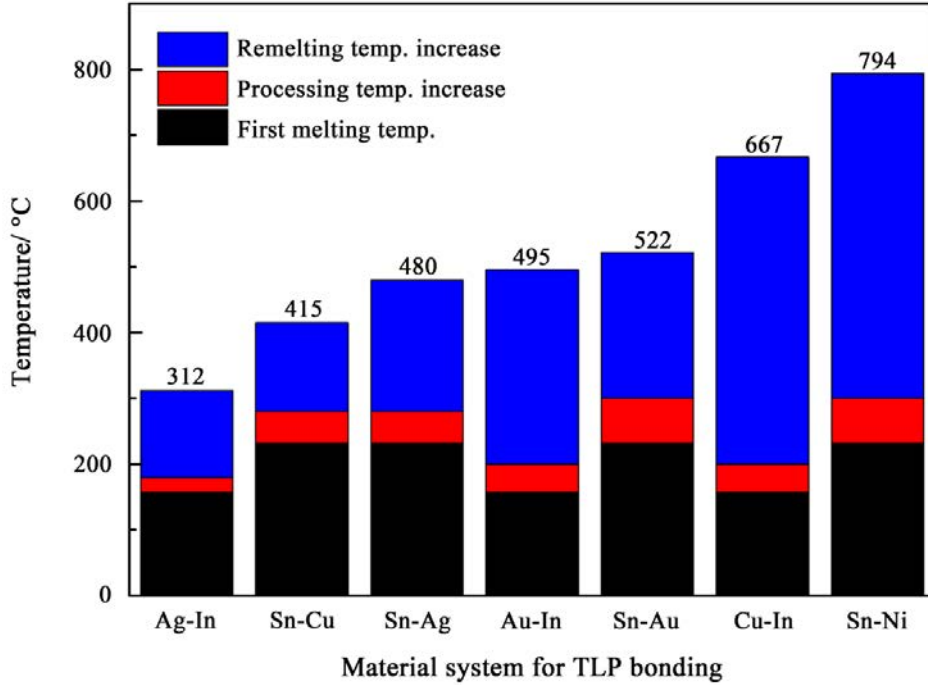


Figure 1.5: Summary of temperature changes during TLP bonding

1.2.3. SILVER SINTERING TECHNOLOGY

Sintering with metal nanoparticles has attracted increased attention in the die attach process [58-60]. The nanosilver sintering technology has been used as a die attach method in power devices since early 2000s [61]. The nanoparticles can be sintered as a bulk at relative lower temperatures when comparing with the melting point of pure metals. The simplified sintering process is shown in Figure 1.6. Several advantages in nanosilver sintered joints have been proven, such as low processing temperature (around 250°C), high thermal conductivity (240 W/(m·K)) and electrical conductivity ($2.6 \times 10^7 / (\Omega \cdot \text{m})$), good thermal stability and favorable bonding strength [30, 62]. This method has been successfully applied in SiC and GaN based transistors and amplifiers with junction temperatures above 200°C [63]. Besides, the nano-copper sintering technology has also been developed for die attach process [64-67]. However, the highly oxidation of Cu nanoparticles during sintering limits the practical application in die attach process [68].

Table 1.2: Summary of TLP bonding technology

Material system	Bonding requirements	Resulted phases	Re-melting temp. (°C)	Ref.
Ag-In	180°C, 3 MPa, 8 min, vacuum	Ag ₂ In	312	[51]
Sn-Cu	280°C, 0.05 MPa, 20 min, nitrogen	Cu ₆ Sn ₅ & Cu ₃ Sn	415	[52]
Sn-Ag	280°C, 0.3 MPa, 30 min	Ag ₃ Sn & Ag	480	[53]
Au-In	200°C, 5 MPa, 10 min, argon	AuIn ₂ & Au ₉ In ₄	495	[54, 55]
Sn-Au	350°C, 2.5 MPa, 30 min, vacuum	Au _{0.85} Sn _{0.15}	522	[56]
Cu-In	200°C, 50 MPa, 5 min, air	Cu ₇ In ₃	667	[55]
Sn-Ni	300°C, 0.3 MPa, 120 min	Ni ₃ Sn ₄	794	[57]

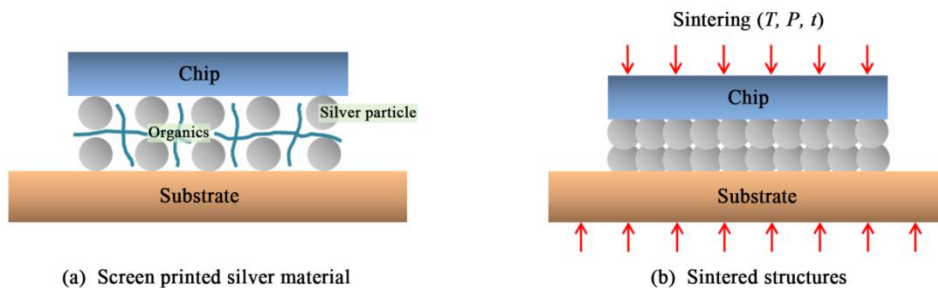


Figure 1.6: Schematic diagram of sintering process, T, P and t represents the temperature, pressure and time, respectively

FORMATION OF SILVER PASTE

The Carey Lea's colloidal approach is one of the most commonly used ways to synthesis silver nanoparticles [69]. Generally, the silver nitrate (AgNO_3) and sodium citrate dihydrate ($\text{Na}_3\text{C}_6\text{H}_5\text{O}_7 \cdot 2\text{H}_2\text{O}$) are used as ionic precursor and reducing agent, respectively. Firstly, a precursor is gained by dissolving AgNO_3 into deionized water and then the solution is heated to 80°C. Secondly, the reducing agent of $\text{Na}_3\text{C}_6\text{H}_5\text{O}_7 \cdot 2\text{H}_2\text{O}$ is added slowly into the precursor under magnetic stirring, then the solution is heated to 90°C and kept for 1 hour. After this process, the solution is cooled down to room temperature in ambient atmosphere. Thirdly, the solution is concentrated by centrifugation and only water was left on the top. The nanosilver particles are obtained by removing the upper water.

The silver nanoparticles will be further mixed with binders and thinners to form

nanosilver paste. Binders are long chain polymers and mainly used for supporting the nanoparticles and preventing the cracking of sintered paste during heating process. The sintered nanosilver joint with binder system of low burnout temperatures showed a denser microstructure [70]. Thinners are used for controlling the viscosity of silver paste, which will be further used for screen/stencil printing or syringe dispensing.

SILVER SINTERING PROCESS

Generally, there are two main methods used for nanosilver sintering: pressureless sintering and pressure assisted sintering. The pressureless sintering of silver paste is usually achieved in a heating plate, furnace or even the reflow oven. The whole heating process mainly consists of three stages, the preheating (initial heating and drying), sintering and cooling stage. Since the silver paste contains certain amount of organics, the preheating process is necessarily needed for the drying of some organics, which will last for around 30 min [71, 72]. The silver paste is usually heated up to 250~300°C during sintering stage and kept for 5~30 min. The whole sintering process can be finished in air. The most significant advantage of pressureless sintering is the simple operation process. However, obvious disadvantages are also proposed and the first one is the time-consuming process of this technology. Secondly, the incomplete evaporation of organics inside the silver paste will result in the increase of porosity. Meanwhile, the contamination issue of organic burnout is another concern for the reliability of power packages. Thirdly, the pressureless sintered joint usually has a high porosity, which will decrease the thermal and electrical performance of power package. Besides, the pressureless sintering is only suitable for the sintering of chips that is smaller than 3×3 mm² [73, 74].

It has been proven that the application of pressure during sintering improved the properties of sintered joints [75, 76]. Firstly, the applied pressure helps to increase the number of interactions between different nanoparticles. Secondly, the pressure acted as a mechanical force to help the evaporation of organic shells except thermal load. It is suggested that the application of 5 MPa pressure during sintering can help the joints to get a high shear strength [77, 78]. Figure 1.7 shows a simplified layout of pressure assisted sintering equipment, which has already been used for many commercial projects.

According to the research conducted by Wang [79], the pressure assisted sintering process is carried out as follows: firstly, the nanosilver film is first transferred to the bonding area of the die. Next, by using a pick-and-place process, the die will be furtherly assembled on DBC substrate which locates at the designed loading plate. After assembling, the loading plate will be moved into the equipment for fast sintering, which

only takes few minutes. During this process, a precisely controlled pressure will be applied on individual die through the patented dynamic insert. It is suggested that the final sintered structure has a uniform microstructure and a typical density more than 85% can be obtained.

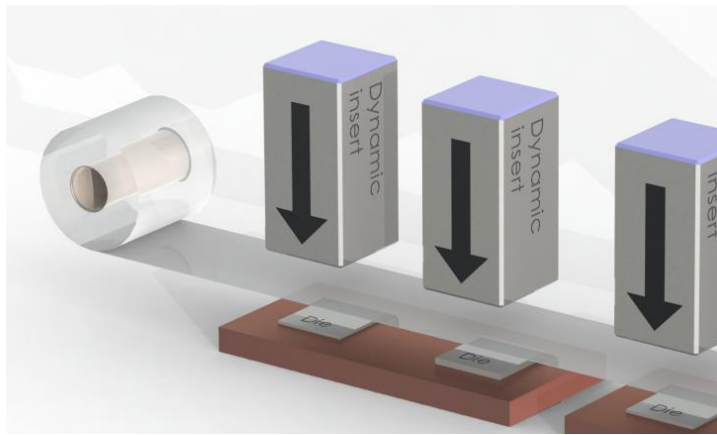


Figure 1.7: Layout of pressure assisted sintering (Courtesy of Boschman Technologies)

MATERIALS FOR SILVER SINTERING

When the size of metal particle reduces to nanoscale, the driving force for sintering increases due to the high surface curvature of nanoparticle, which will also lead to the decrease of melting temperature [80-82]. These phenomena are expected to enhance the sintering of nanosilver particles. Until now, different types of silver materials have been developed for die attach process, such as silver nanoparticle paste [83, 84], silver micro-particle paste [85], silver oxide micro-particle paste [86, 87], silver flake paste [88], silver nanonord paste [89], and etc. Besides, in order to increase the packing density inside sintered layer, the silver particles with different diameters are usually mixed together. For instance, the typical volumetric ratio of 1:3 is suggested for nano to micron-Ag ratio to get the maximum packing density [90]. According to the test results from Li *et al* [91], the sintered layer, which originally consists of 10 and 50 nm particles, has gained high thermal conductivity (278.5 W/(m·K)) and shear strength (41.8 MPa), as well as excellent resistance to thermal cycling.

In addition, due to the high electrical and thermal conductivity, as well as low cost of copper, the copper particles with an average diameter of 50 nm were added into nanosilver paste [92-94]. The composite paste was then sintered at 380°C without applying pressure. The bonding strength, thermal and electrical conductivity showed a decreasing trend with the increasing percentage of copper particles. The high weight percentage of copper particles resulted in the increase of porosity. The best bonding

properties were found on silver coated substrate. As a result, the composite paste with 20 wt% copper particles showed acceptable sintering properties. Similar results were gained with aluminum refined nanosilver paste [95-98]. In addition, the die attached by silver epoxy and conductive adhesives showed lower thermal conductivities (~ 60 W/(m·K) and ~ 10 W/(m·K), respectively) when compared with sintered nanosilver particles with dimensions of 10-30 nm (200 W/(m·K)) [99-101].

Recently, the nanosilver film, which has a similar composition as the silver paste, has been proven to be one of the most potential die attach materials [102-104]. The nanosilver film sintered layer has a uniform thickness distribution and less organic burnout, which ensures the high bonding quality between the power die and substrate. However, few researches have been done to systematically investigate the sintering properties of this material.

1.2.4. Comparison of three main die attach technologies

The comprehensive comparisons of die attach methods are listed in Table 1.3, and three main differences can be found. Firstly, there is a big difference in the composition of die attach materials. Comparing with the lead free soldering and silver sintering, the materials used in TLP bonding technology consist of at least one or two materials with different melting temperatures.

Secondly, the final compositions vary from each other. The remaining solder alloy and IMCs are the main phases in lead free soldered layer. However, full IMCs are formed in the final die attach layer of TLP bonding. Different from the previous two methods, the nano/micro silver sintered layer only consists of pure silver and small amount of residual organics.

Thirdly, the nano/micro silver sintered die attach layer gained the highest increase of re-melting temperature, which is comparable to the melting temperature of the bulk silver material (961°C). The re-melting temperature of TLP bonded die attach layer is higher than lead free soldered layer due to the formation of IMCs within the whole layer. Although the IMCs formed at the interface of lead free solder and substrate, the re-melting temperature of lead free soldered layer only increases slightly.

Table 1.3: Comprehensive comparison of die attach methods

	Soldering (Au-20Sn)	TLP bonding (Sn-Cu)	Sintering (Nanosilver paste)
Material compositions	Solder alloy	Solder alloy or pure Sn	Nanoparticles + organics
Material types	Paste, preform	Paste, thin layer	Paste, film
Substrate/die surface coating	Ni-Au (both)	Ni-Au on die	Ag or Au (both)
Processing method	Reflow, ultrasonic soldering	Direct heating	Sintering
Processing temp.	310°C	230°C	250°C
Pressure required	No	Yes	Yes/No
Final compositions	Solder alloy + IMCs	Full IMCs (Cu ₆ Sn ₅)	Pure Ag + organic residuals
Re-melting temperature	Slightly higher than solder's melting point	Melting point of IMCs	Theoretically 961°C
Thermal conductivity	57 W/(m·K) [42]	34.1 W/(m·K) [105]	240 W/(m·K) [106]
Electrical conductivity	$1.64 \times 10^7 / (\Omega \cdot m)$ [41]	$0.57 \times 10^7 / (\Omega \cdot m)$ [105]	$2.6 \times 10^7 / (\Omega \cdot m)$ [30]
CTE at 25°C	$18 \times 10^{-6} / K$ [107]	$16.3 \times 10^{-6} / K$ [108]	$19 \times 10^{-6} / K$ [106]
Young's modulus	70.95 GP, at 25°C [107]	119 GP, at 25°C [109]	9 GP, at 25°C [106]
Accurate control of final height	Difficult	Difficult	Can be controlled
Voiding issue	Can be optimized	Can be optimized	Micro/nano voids
Reliability issues	Brittle interfacial IMCs, and evolution of microstructure	Evolution of IMCs	Evolution of voids

1.3. RESEARCH OBJECTIVES

The press pack IGBT module has shown superior performance in high power density applications and is expected to work at temperatures higher than 200°C. Comparing with the high temperature soldering technology and TLP bonding technology, the nanosilver sintering technology has significant advantage in attaching chips in a press pack IGBT module. However, limited researches have reported the application of nanosilver sintering technology in high power press pack modules. Furthermore, most of the literatures are studying the properties of pressureless sintered silver joint, which has exhibited limitations in high power modules due to the degradation of the electrical and thermal performance resulted from its high porosity. In comparison, the pressure assisted sintering technology shows great potentials since the sintering pressure enhances the bonding quality of nanosilver sintered joint. In addition, current research lacks the knowledge of pressure assisted nanosilver sintering process.

According to the problem descriptions above, the objectives of this thesis are:

- (1) The sintering pressure, temperature and time are the three dominating factors in determining the sintering properties of nanosilver particles. The sintering behavior of nanosilver particles at various parameters is one of the main topics that this research is set to explore. The corresponding shear strength and fracture morphology of sintered joint are investigated. The obtained results provide technical guidance to the feasibility of employing pressure assisted nanosilver sintering technology in attaching power chips.
- (2) The nanosilver sintered layer is expected to serve applications with such requirements as high bonding strength while maintaining high temperature stability. Thus, the high temperature nanoindentation is performed in this thesis to obtain the micro mechanical properties of sintered layer. The plastic behavior and creep properties of sintered nanosilver particles are investigated by considering both the temperature effect and pressure effect. The test results provide foundational knowledge for the future pressure assisted sintering of nanosilver particles, which is also one of the most valuable novelties of this research to the whole power electronics field
- (3) The pressure assisted sintering technology is designed for the nanosilver double side sintered press pack power package. Mechanical tests prove the high bonding quality of sintered layer. The designed technology is successfully implemented in the mass production of press pack power package. The finite element analysis is carried out to simulate the effects of sintering sequence on the stress distribution of sintered package. The sintering stress analysis will be intensely addressed in this thesis as it is

one of the most challenging parts in the power package fabrication process.

- (4) The nanosilver sintering technology is employed in the ceramic package. The sintered area is examined by several methods to ensure the high bonding quality. The finite element analysis method is used to predict the stress distribution of sintered package. Comparisons are given between the two kinds of lids sintered package, including bonding quality, stress distribution and sintering pressure effects.

1.4. THESIS OUTLINE

The rest of this thesis is structured as follows:

Chapter 2 focuses on the effects of sintering parameters on the bonding quality of nanosilver sintered sandwich package. The evolution of shear strength and fracture morphology is respectively investigated at various sintering pressures, temperatures, time. The bonding mechanism of nanosilver particles is discussed based on the results obtained. Based on the analysis in Chapter 2, Chapter 3 focuses on investigating the micro mechanical properties of pressure sintered nanosilver joint at various test temperatures. The nanoindentation test is performed for sintered joint to evaluate the sintering pressure effects on the bonding properties of nanosilver particles. The plastic stress-strain constitutive equations of pressure sintered nanosilver joint at room temperature are demonstrated in Chapter 3. The effects of temperature on the hardness and elastic modulus are analyzed accordingly. Besides, the initial creep properties of pressure sintered nanosilver joint at high temperatures are characterized.

Chapter 4 focuses on employing the nanosilver sintering technology in the double side sintered press pack power module. The morphologies and density of pressure free and pressure assisted sintered nanosilver particles are first compared. Mechanical characterization is conducted and the module shows satisfying performance in terms of shear strength and fracture morphology, proving the presented nanosilver sintering technology as promising approach for attaching chips of high power press pack module application. Chapter 5 focuses on investigating the stress distributions of sintered package in various sintering sequences and sintering pressures since the cracking of die becomes the critical issue in pressure assisted sintering process. One of the research approaches employed in this thesis is the combination of the experimental tests and finite element analysis simulations. Three main sintering sequences are designed to fabricate the double side nanosilver sintered module. The simulation results explained the crack generation and prolongation in chips. The optimal sintering sequence is recommended for the future mass production.

Chosen as another application scenario of nanosilver sintering technology, the

sealing of a hermetic cavity is realized and presented in Chapter 6. The silver coated copper and silicon are selected as lid materials for the hermetic cavity. The bonding properties of sintered layer are characterized by the X-ray and C-SAM. The test results showed that the silicon lid sintered cavity displays good bonding quality. Finite element analysis (FEA) is employed to evaluate the stress distribution on sintered cavity and the obtained results are analyzed and compared with the experimental results. In addition, the effects of sintering pressure on the evolution of maximum stress distribution on both copper lid and silicon lid are explained in detail in this chapter.

In Chapter 7, the main conclusions and recommendations of this thesis are summarized. The achievement of this thesis provides fundamental knowledge for the further development of pressure assisted nanosilver sintering technology. Finally, an outlook for future research and development is presented.

REFERENCES

- [1] J.G. Kassakian and T.M. Jahns, *Evolving and emerging applications of power electronics in systems*, IEEE Journal of Emerging and Selected Topics in Power Electronics **1**, 47 (2013).
- [2] F. Iacopi, M. Hove, M. Charles, and K. Endo, *Power electronics with wide bandgap materials: Toward greener, more efficient technologies*, MRS Bulletin **40**, 390 (2015).
- [3] B. Ji, X. Song, E. Sciberras, W. Cao, Y. Hu, and V. Pickert, *Multiobjective design optimization of IGBT power modules considering power cycling and thermal cycling*, IEEE Transactions on Power Electronics **30**, 2493 (2015).
- [4] L.A. Navarro, X. Perpiñà, P. Godignon, J. Montserrat, V. Banu, M. Vellvehi, and X. Jordà, *Thermomechanical assessment of die-attach materials for wide bandgap semiconductor devices and harsh environment applications*, IEEE Transactions on Power Electronics **29**, 2261 (2014).
- [5] R. Khazaka, L. Mendizabal, D. Henry, and R. Hanna, *Survey of high-temperature reliability of power electronics packaging components*, IEEE Transactions on Power Electronics **30**, 2456 (2015).
- [6] C. Hang, J. He, Z. Zhang, H. Chen, and M. Li, *Low temperature bonding by infiltrating Sn3.5Ag solder into porous Ag sheet for high temperature die attachment in power device packaging*, Scientific Reports **8**, 17422 (2018).
- [7] J. Broughton, V. Smet, R.R. Tummala, and Y.K. Joshi, *Review of thermal packaging*

- technologies for automotive power electronics for traction purposes*, Journal of Electronic Packaging **140**, 040801 (2018).
- [8] J. Millan, P. Godignon, X. Perpina, A. Pérez-Tomás, and J. Rebollo, *A survey of wide bandgap power semiconductor devices*, IEEE Transactions on Power Electronics **29**, 2155 (2014).
- [9] H.A. Mantooth, M.D. Glover, and P. Shepherd, *Wide bandgap technologies and their implications on miniaturizing power electronic systems*, IEEE Journal of Emerging and Selected Topics in Power Electronics **2**, 374 (2014).
- [10] L. Fu, X. Zhang, M. Scott, C. Yao, and J. Wang, *The evaluation and application of wide bandgap power devices*, in *IEEE Conference and Expo Transportation Electrification Asia-Pacific (ITEC Asia-Pacific 2014)*, 2014, pp. 1-5.
- [11] H.A. Mustain, W.D. Brown, and S.S. Ang, *Transient liquid phase die attach for high-temperature silicon carbide power devices*, IEEE Transactions on Components and Packaging Technologies **33**, 563 (2010).
- [12] Y. Nakakohara, H. Otake, T.M. Evans, T. Yoshida, M. Tsuruya, and K. Nakahara, *Three-phase LLC series resonant DC/DC converter using SiC MOSFETs to realize high-voltage and high-frequency operation*, IEEE Transactions on Industrial Electronics **63**, 2103 (2016).
- [13] H.S. Chin, K.Y. Cheong, and A.B. Ismail, *A review on die attach materials for SiC-based high-temperature power devices*, Metallurgical and Materials Transactions B **41**, 824 (2010).
- [14] U.M. Choi, F. Blaabjerg, and K.B. Lee, *Study and handling methods of power IGBT module failures in power electronic converter systems*, IEEE Transactions on Power Electronics **30**, 2517 (2015).
- [15] H. Ye, M. Lin, and C. Basaran, *Failure modes and FEM analysis of power electronic packaging* Finite Elements in Analysis and Design **38**, 601 (2002).
- [16] G. Zeng, S. McDonald, and K. Nogita, *Development of high-temperature solders: review*, Microelectronics Reliability **52**, 1306 (2012).
- [17] H. Yu and J.K. Kivilahti, *Nucleation kinetics and solidification temperatures of SnAgCu interconnections during reflow process*, IEEE Transactions on Components and Packaging Technologies **29**, 778 (2006).
- [18] M. Drienovsky, L.R. Trnkova, M. Martinkovic, M. Ozvold, I. Cernickova, M. Palcut, and J. Janovec, *Influence of cerium addition on microstructure and properties of*

- Sn-Cu-(Ag) solder alloys*, *Materials Science and Engineering: A* **623**, 83 (2015).
- [19] A.A. Bajwa, Y. Qin, R. Reiner, R. Quay, and J. Wilde, *Assembly and packaging technologies for high-temperature and high-power GaN devices*, *IEEE Transactions on Components, Packaging and Manufacturing Technology* **5**, 1402 (2015).
- [20] P. Godijn, W. Veldhuizen, P. Lusse, M.T. Holtzer, R. Ekeren, and M. Haan, *Solder preforms for use in electronic assembly*, (2009), US Patent 7533793B2.
- [21] N. Hirano, A. Tanahashi, Y. Sakamoto, K. Tsuruta, T. Ishii, and S. Soga, *Solder preform and a process for its manufacture*, (2010), US Patent 7793820B2.
- [22] <http://www.welding-consultant.com/SolderingBrazing>.
- [23] T. Laurila, V. Vuorinen, and J. Kivilahti, *Interfacial reactions between lead-free solders and common base materials*, *Materials Science and Engineering: R: Reports* **49**, 1 (2005).
- [24] Y. Liu, F. Sun, L. Luo, C.A. Yuan, and G. Zhang, *Microstructure evolution and shear behavior of the solder joints for flip-chip LED on ENIG substrate*, *Journal of Electronic Materials* **44**, 2450 (2015).
- [25] O.M. Abdelhadi and L. Ladani, *IMC growth of Sn-3.5Ag/Cu system: combined chemical reaction and diffusion mechanisms*, *Journal of Alloys and Compounds* **537**, 87 (2012).
- [26] S.W. Chen, P.Y. Chen, and C.H. Wang, *Lowering of Sn-Sb alloy melting points caused by substrate dissolution*, *Journal of Electronic Materials* **35**, 1982 (2006).
- [27] H. Beyer, V. Sivasubramaniam, M. Bayer, and S. Hartmann, *Reliability of lead-free large area solder joints in IGBT modules with respect to passive and active thermal cycling*, in *9th International Conference on Integrated Power Electronics Systems (CIPS 2016)*, 2016, pp. 1-6.
- [28] Z. Tao, T. Bobal, M. Oud, and S.L. Jia, *An introduction to eutectic Au/Sn solder alloy and its preforms in microelectronics/optoelectronic packaging applications*, *Electronics & Packaging* **8**, 2 (2005).
- [29] J.W. Yoon, H.S. Chun, J.M. Koo, and S.B. Jung, *Au-Sn flip-chip solder bump for microelectronic and optoelectronic applications*, *Microsystem Technologies* **13**, 1463 (2007).
- [30] V.R. Manikam and K.Y. Cheong, *Die attach materials for high temperature*

- applications: A review*, IEEE Transactions on Components, Packaging and Manufacturing Technology **1**, 457 (2011).
- [31] N. Weyrich, S. Jin, L.I. Duarte, and C. Leinenbach, *Joining of Cu, Ni, and Ti using Au-Ge-based high-temperature solder alloys*, Journal of Materials Engineering and Performance **23**, 1585 (2014).
- [32] A. Hartnett and S. Buerki, *Process and reliability advantages of AuSn eutectic die attach*, Proc. 42nd IMAPS 281 (2009).
- [33] Z. Shen, R.W. Johnson, and M.C. Hamilton, *SiC power device die attach for extreme environments*, IEEE Transactions on Electron Devices **62**, 346 (2015).
- [34] H. Zhang and N.C. Lee, *A novel high melting lead-free mixed solder paste system*, in *IEEE 13th Electronics Packaging Technology Conference (EPTC 2011)*, 2011, pp. 567-572.
- [35] Z. Shen, K. Fang, R.W. Johnson, and M.C. Hamilton, *Characterization of Bi-Ag-X solder for high temperature SiC die attach*, IEEE Transactions on Components, Packaging and Manufacturing Technology **4**, 1778 (2014).
- [36] M. Uvarajan, L. Lim, M. Goh, F. Ng, and W. Pan, *Temperature cycling aging studies of Zn-based solders for high-temperature applications*, in *IEEE 17th Electronics Packaging and Technology Conference (EPTC 2015)*, 2015, pp. 1-5.
- [37] A. Haque, Y. Won, A. Haseeb, and H. Masjuki, *Investigations on Zn-Al-Ge alloys as high temperature die attach material*, in *3rd Electronic System-Integration Technology Conference (ESTC 2010)*, 2010, pp. 1-5.
- [38] N. Kang, H.S. Na, S.J. Kim, and C.Y. Kang, *Alloy design of Zn-Al-Cu solder for ultra high temperatures*, Journal of Alloys and Compounds **467**, 246 (2009).
- [39] H. Zhang, J. Fan, J. Zhang, C. Qian, X. Fan, F. Sun, and G. Zhang, *Reliability optimization of gold-tin eutectic die attach layer in HEMT package*, in *13th China International Forum on Solid State Lighting (SSLChina 2016)*, 2016, pp. 52-56.
- [40] C.P. Wang, T.T. Chen, H.K. Fu, T.L. Chang, P.T. Chou, and M.T. Chu, *Analysis of thermal characteristics and mechanism of degradation of flip-chip high power LEDs*, Microelectronics Reliability **52**, 698 (2012).
- [41] Y. Wang, W. Liu, Y. Ma, Y. Huang, Y. Tang, F. Cheng, and Q. Yu, *Indentation size effect and micromechanics characterization of intermetallic compounds in the Au-Sn system*, Materials Science and Engineering: A **610**, 161 (2014).

- [42] Y. Tian, W. Zhou, and P. Wu, *A density functional investigation of the structural, elastic and thermodynamic properties of the Au-Sn intermetallics*, Journal of Electronic Materials **45**, 639 (2016).
- [43] M. Hindler, Z. Guo, and A. Mikula, *Lead-free solder alloys: Thermodynamic properties of the (Au+Sb+Sn) and the (Au+Sb) system*, The Journal of Chemical Thermodynamics **55**, 102 (2012).
- [44] A.A. Bajwa and J. Wilde, *Reliability modeling of Sn-Ag transient liquid phase die-bonds for high-power SiC devices*, Microelectronics Reliability **60**, 116 (2016).
- [45] S. Marauska, M. Claus, T. Lisec, and B. Wagner, *Low temperature transient liquid phase bonding of Au/Sn and Cu/Sn electroplated material systems for MEMS wafer-level packaging*, Microsystem Technologies **19**, 1119 (2013).
- [46] V. Vuorinen, A. Rautiainen, and M. Paulasto-Krockel, *Design for reliability of Au-Sn and Cu-Sn based SLID bonds*, in *European Microelectronics Packaging Conference (EMPC 2015)*, 2015, pp. 1-6.
- [47] G.O. Cook and C.D. Sorensen, *Overview of transient liquid phase and partial transient liquid phase bonding*, Journal of Materials Science **46**, 5305 (2011).
- [48] F. Lang, H. Yamaguchi, H. Nakagawa, and H. Sato, *Thermally stable bonding of SiC devices with ceramic substrates: Transient liquid phase sintering using Cu/Sn powders*, Journal of The Electrochemical Society **160**, D315 (2013).
- [49] H. Feng, J. Huang, J. Yang, S. Zhou, R. Zhang, and S. Chen, *A transient liquid phase sintering bonding process using nickel-tin mixed powder for the new generation of high-temperature power devices*, Journal of Electronic Materials **46**, 4152 (2017).
- [50] A. Syed Khaja, C. Kaestle, and J. Franke, *Reliable packaging technologies for power electronics: Diffusion soldering and heavy copper wire bonding*, in *3rd International Electric Drives Production Conference (EDPC 2013)*, 2013, pp. 1-6.
- [51] S.J. Hsu and C.C. Lee, *Bonding of SiC chips to copper substrates using Ag-In system*, in *IEEE 65th Electronic Components and Technology Conference (ECTC 2015)*, 2015, pp. 1247-1250.
- [52] K. Chu, Y. Sohn, and C. Moon, *A comparative study of Cu/Sn/Cu and Ni/Sn/Ni solder joints for low temperature stable transient liquid phase bonding*, Scripta Materialia **109**, 113 (2015).
- [53] N.S. Nobeen, R. Imade, B.R. Lee, R. Phua, E. Jian, C.C. Wong, C.L. Gan, and Z. Chen, *Transient liquid phase (TLP) bonding using Sn/Ag multilayers for high*

- temperature applications*, in *IEEE 15th Electronics Packaging Technology Conference (EPTC 2013)*, 2013, pp. 647-652.
- [54] B.J. Grummel, Z.J. Shen, H.A. Mustain, and A.R. Hefner, *Thermo-mechanical characterization of Au-In transient liquid phase bonding die-attach*, *IEEE Transactions on Components, Packaging and Manufacturing Technology* **3**, 716 (2013).
- [55] J.B. Lee, H.Y. Hwang, and M.W. Rhee, *Reliability investigation of Cu/In TLP bonding*, *Journal of Electronic Materials* **44**, 435 (2015).
- [56] T.A. Tollefsen, A. Larsson, O.M. Lovvik, and K.E. Aasmundtveit, *High temperature interconnect and die attach technology: Au-Sn SLID bonding*, *IEEE Transactions on Components, Packaging and Manufacturing Technology* **3**, 904 (2013).
- [57] S.W. Yoon, M.D. Glover, and K. Shiozaki, *Nickel-tin transient liquid phase bonding toward high-temperature operational power electronics in electrified vehicles*, *IEEE Transactions on Power Electronics*, **28**, 2448 (2013).
- [58] J. Scola, X. Tassart, C. Vilar, F. Jomard, E. Dumas, Y. Veniaminova, P. Boullay, and S. Gascoin, *Microstructure and electrical resistance evolution during sintering of a Ag nanoparticle paste*, *Journal of Physics D: Applied Physics* **48**, 145302 (2015).
- [59] T. Yamakawa, T. Takemoto, M. Shimoda, H. Nishikawa, K. Shiokawa, and N. Terada, *Influence of joining conditions on bonding strength of joints: efficacy of low-temperature bonding using Cu nanoparticle paste*, *Journal of Electronic Materials* **42**, 1260 (2013).
- [60] C. Buttay, B. Allard, and R. Riva, *Silver sintering for power electronics integration*, in *International Conference on Electronics Packaging and iMAPS All Asia Conference (ICEP-IACC 2015)*, 2015, pp. 554-558.
- [61] Z. Zhang and G.Q. Lu, *Pressure-assisted low-temperature sintering of silver paste as an alternative die-attach solution to solder reflow*, *IEEE Transactions on Electronics Packaging Manufacturing* **25**, 279 (2002).
- [62] J. Bai, Z. Zhang, J. Calata, and G. Lu, *Characterization of low-temperature sintered nanoscale silver paste for attaching semiconductor devices*, in *2005 Conference on High Density Microsystem Design and Packaging and Component Failure Analysis*, 2005, pp. 1-5.
- [63] C. Buttay, D. Planson, B. Allard, D. Bergogne, P. Bevilacqua, C. Joubert, M. Lazar, C. Martin, H. Morel, and D. Tournier, *State of the art of high temperature power*

- electronics*, Materials Science and Engineering: B **176**, 283 (2011).
- [64] J. Liu, H. Chen, H. Ji, and M. Li, *Highly conductive Cu–Cu joint formation by low-temperature sintering of formic acid-treated Cu nanoparticles*, ACS Applied Materials & Interfaces **8**, 33289 (2016).
- [65] B.H. Lee, M.Z. Ng, A.A. Zinn, and C.L. Gan, *Evaluation of copper nanoparticles for low temperature bonded interconnections*, in *IEEE 22nd International Symposium on the Physical and Failure Analysis of Integrated Circuits (IPFA 2015)*, 2015, pp. 102-106.
- [66] T. Ishizaki, A. Kuno, A. Tane, M. Yanase, F. Osawa, T. Satoh, and Y. Yamada, *Reliability of Cu nanoparticle joint for high temperature power electronics*, Microelectronics Reliability **54**, 1867 (2014).
- [67] T. Ishizaki, T. Satoh, A. Kuno, A. Tane, M. Yanase, F. Osawa, and Y. Yamada, *Thermal characterizations of Cu nanoparticle joints for power semiconductor devices*, Microelectronics Reliability **53**, 1543 (2013).
- [68] J. Kähler, N. Heuck, A. Wagner, A. Stranz, E. Peiner, and A. Waag, *Sintering of copper particles for die attach*, IEEE Transactions on Components, Packaging and Manufacturing Technology **2**, 1587 (2012).
- [69] G. Frens and J.T.G. Overbeek, *Carey Lea's colloidal silver*, Kolloid-Zeitschrift und Zeitschrift für Polymere **233**, 922 (1969).
- [70] J.G. Bai, T.G. Lei, J.N. Calata, and G.Q. Lu, *Control of nanosilver sintering attained through organic binder burnout*, Journal of Materials Research **22**, 3494 (2007).
- [71] A.A. Wereszczak, B.R. Chen, and B.A. Oistad, *Reflow-oven-processing of pressureless sintered-silver interconnects*, Journal of Materials Processing Technology **255**, 500 (2018).
- [72] X. Wang, Y. Mei, X. Li, M. Wang, Z. Cui, and G.Q. Lu, *Pressureless sintering of nanosilver paste as die attachment on substrates with ENIG finish for semiconductor applications*, Journal of Alloys and Compounds **777**, 578 (2019).
- [73] K. Qi, X. Chen, and G.Q. Lu, *Effect of interconnection area on shear strength of sintered joint with nano-silver paste*, Soldering & Surface Mount Technology **20**, 8 (2008).
- [74] W. Guo, Z. Zeng, X. Zhang, P. Peng, and S. Tang, *Low-Temperature sintering bonding using silver nanoparticle paste for electronics packaging*, Journal of Nanomaterials **2015**, 10 (2015).

- [75] T.G. Lei, J.N. Calata, G.Q. Lu, X. Chen, and S. Luo, *Low-temperature sintering of nanoscale silver paste for attaching large-area chips*, IEEE Transactions on Components and Packaging Technologies **33**, 98 (2010).
- [76] M. Knoerr and A. Schletz, *Power semiconductor joining through sintering of silver nanoparticles: evaluation of influence of parameters time, temperature and pressure on density, strength and reliability*, in *6th International Conference on Integrated Power Electronics Systems (CIPS 2010)*, 2010, pp. 1-6.
- [77] Y. Mei, G. Chen, Y. Cao, X. Li, D. Han, and X. Chen, *Simplification of low-temperature sintering nanosilver for power electronics packaging*, Journal of Electronic Materials **42**, 1209 (2013).
- [78] G. Chen, Y. Cao, Y. Mei, D. Han, G.Q. Lu, and X. Chen, *Pressure-assisted low-temperature sintering of nanosilver paste for 5×5 mm² chip attachment*, IEEE Transactions on Components, Packaging and Manufacturing Technology **2**, 1759 (2012).
- [79] L. Wang, *Low temperature hermetic packaging with Ag sintering process*, in *16th International Conference on Electronic Packaging Technology (ICEPT 2015)*, 2015, pp. 1317-1320.
- [80] H. Alarifi, A. Hu, M. Yavuz, and Y.N. Zhou, *Silver nanoparticle paste for low-temperature bonding of copper*, Journal of Electronic Materials **40**, 1394 (2011).
- [81] H. Alarifi, M. Atis, C. Özdoğan, A. Hu, M. Yavuz, and Y. Zhou, *Molecular dynamics simulation of sintering and surface premelting of silver nanoparticles*, Materials Transactions **54**, 884 (2013).
- [82] P. Peng, A. Hu, A.P. Gerlich, G. Zou, L. Liu, and Y.N. Zhou, *Joining of silver nanomaterials at low temperatures: processes, properties, and applications*, ACS Applied Materials & Interfaces **7**, 12597 (2015).
- [83] S. Park, D. Seo, and J. Lee, *Preparation of Pb-free silver paste containing nanoparticles*, Colloids and Surfaces A: Physicochemical and Engineering Aspects **313**, 197 (2008).
- [84] W.H. Li, P.S. Lin, C.N. Chen, T.Y. Dong, C.H. Tsai, W.T. Kung, J.M. Song, Y.T. Chiu, and P.F. Yang, *Low-temperature Cu-to-Cu bonding using silver nanoparticles stabilised by saturated dodecanoic acid*, Materials Science and Engineering: A **613**, 372 (2014).

- [85] J. Jiu, H. Zhang, S. Nagao, T. Sugahara, N. Kagami, and K. Suganuma, *A new micro-silver paste for high power semiconductor devices*, in *China Semiconductor Technology International Conference (CSTIC 2016)*, 2016, pp. 1-3.
- [86] A. Hirose, H. Tatsumi, N. Takeda, Y. Akada, T. Ogura, E. Ide, and T. Morita, *A novel metal-to-metal bonding process through in-situ formation of Ag nanoparticles using Ag₂O microparticles*, *Journal of Physics: Conference Series* **165**, 012074 (2009).
- [87] F. Mu, Z. Zhao, G. Zou, H. Bai, A. Wu, L. Liu, D. Zhang, and Y.N. Zhou, *Mechanism of low temperature sintering-bonding through in-situ formation of silver nanoparticles using silver oxide microparticles*, *Materials Transactions* **54**, 872 (2013).
- [88] C.A. Lu, P. Lin, H.C. Lin, and S.F. Wang, *Effects of metallo-organic decomposition agents on thermal decomposition and electrical conductivity of low-temperature-curing silver paste*, *Japanese Journal of Applied Physics* **45**, 6987 (2006).
- [89] J. Jiu, K. Murai, K. Kim, and K. Suganuma, *Synthesis of silver nanorods and application for die attach material in devices*, *Journal of Materials Science: Materials in Electronics* **21**, 713 (2010).
- [90] K.S. Siow and Y. Lin, *Identifying the development state of sintered silver (Ag) as a bonding material in the microelectronic packaging via a patent landscape study*, *Journal of Electronic Packaging* **138**, 020804 (2016).
- [91] M. Li, Y. Xiao, Z. Zhang, and J. Yu, *Bimodal sintered silver nanoparticle paste with ultrahigh thermal conductivity and shear strength for high temperature thermal interface material applications*, *ACS Applied Materials & Interfaces* **7**, 9157 (2015).
- [92] K.S. Tan and K.Y. Cheong, *Physical and electrical characteristics of silver-copper nanopaste as alternative die-attach*, *IEEE Transactions on Components, Packaging and Manufacturing Technology* **4**, 8 (2014).
- [93] K.S. Tan and K.Y. Cheong, *Mechanical properties of sintered Ag-Cu die-attach nanopaste for application on SiC device*, *Materials & Design* **64**, 166 (2014).
- [94] K.S. Tan, Y.H. Wong, and K.Y. Cheong, *Thermal characteristic of sintered Ag-Cu nanopaste for high-temperature die-attach application*, *International Journal of Thermal Sciences* **87**, 169 (2015).
- [95] V.R. Manikam, K.A. Razak, and K.Y. Cheong, *Reliability of sintered Ag₈₀-Al₂₀ die attach nanopaste for high temperature applications on SiC power devices*,

- Microelectronics Reliability **53**, 473 (2013).
- [96] V.R. Manikam, K.A. Razak, and K.Y. Cheong, *A novel silver–aluminium high-temperature die attach nanopaste system: the effects of organic additives content on post-sintered attributes*, Journal of Materials Science: Materials in Electronics **24**, 2678 (2013).
- [97] V.R. Manikam, K.A. Razak, and K.Y. Cheong, *Sintering of silver–aluminum nanopaste with varying aluminum weight percent for use as a high-temperature die-attach material*, IEEE Transactions on Components, Packaging and Manufacturing Technology **2**, 1940 (2012).
- [98] V.R. Manikam, K.A. Razak, and K.Y. Cheong, *Physical and electrical attributes of sintered Ag80–Al20 high temperature die attach material with different organic additives content*, Journal of Materials Science: Materials in Electronics **24**, 720 (2013).
- [99] P. Panaccione, T. Wang, X. Chen, S. Luo, and G.Q. Lu, *Improved heat dissipation and optical performance of high-power LED packaging with sintered nanosilver die-attach material*, Journal of Microelectronics and Electronic Packaging **7**, 164 (2010).
- [100] A.A. Bajwa, E. Moller, and J. Wilde, *Die-attachment technologies for high-temperature applications of Si and SiC-based power devices*, in *IEEE 65th Electronic Components and Technology Conference (ECTC 2015)*, 2015, pp. 2168-2174.
- [101] G.Q. Lu, J.N. Calata, Z. Zhang, and J.G. Bai, *A lead-free, low-temperature sintering die-attach technique for high-performance and high-temperature packaging*, in *Sixth IEEE CPMT Conference on High Density Microsystem Design and Packaging and Component Failure Analysis (HDP'04)*, 2004, pp. 42-46.
- [102] G. Greca, P. Salerno, J. Durham, F. Henaff, J.C. Harel, J. Hamelink, and W. He, *Double side sintered IGBT 650V/200A in a TO-247 package for extreme performance and reliability*, in *IEEE 18th Electronics Packaging Technology Conference (EPTC 2016)*, 2016, pp. 589-592.
- [103] R. Khazaka, B. Thollin, L. Mendizabal, D. Henry, and R. Hanna, *Characterization of nanosilver dry films for high-temperature applications*, IEEE Transactions on Device and Materials Reliability **15**, 149 (2015).
- [104] F. Henaff, G. Greca, P. Salerno, O. Mathieu, M. Reger, O. Khaselev, M. Bouregghda, J. Durham, A. Lifton, and J. C. Harel, "Reliability of double side silver sintered devices

- with various substrate metallization," in *International Exhibition and Conference for Power Electronics, Intelligent Motion, Renewable Energy and Energy Management (PCIM Europe 2016)*, 2016, pp. 1027-1034.
- [105] H. Frederikse, R. Fields, and A. Feldman, *Thermal and electrical properties of copper-tin and nickel-tin intermetallics*, *Journal of Applied Physics* **72**, 2879 (1992).
- [106] Y. Mei, G. Chen, L. Guo-Quan, and X. Chen, *Effect of joint sizes of low-temperature sintered nano-silver on thermal residual curvature of sandwiched assembly*, *International Journal of Adhesion and Adhesives* **35**, 88 (2012).
- [107] Y. Liu, J. Zhao, C.A. Yuan, G.Q. Zhang, and F. Sun, *Chip-on-flexible packaging for high-power flip-chip light-emitting diode by AuSn and SAC soldering*, *IEEE Transactions on Components, Packaging and Manufacturing Technology* **4**, 1754 (2014).
- [108] C.C. Lee, P.J. Wang, and J.S. Kim, *Are intermetallics in solder joints really brittle?*, in *57th Electronic Components and Technology Conference (ECTC 2007)*, 2007, pp. 648-652.
- [109] Y. Zhong, R. An, C. Wang, Z. Zheng, Z. Liu, C. Liu, C. Li, T.K. Kim, and S. Jin, *Low temperature sintering Cu_6Sn_5 nanoparticles for superplastic and super-uniform high temperature circuit interconnections*, *Small* **11**, 4097 (2015).

2

BONDING MECHANISMS ANALYSIS OF NANOSILVER SANDWICH SINTERED PACKAGE

Though silver (Ag) nanoparticles have significant advantages on the physical and the mechanical properties, it is difficult to achieve the theoretical performances of bulk Ag by solid sintering of Ag nanoparticles. Due to the geometrical effect of the nanoparticles, the particle neck and pores suppress the properties of the sintering layer. An effective way to decrease the porosity in the sintering layer is to add external pressure during the sintering process. Besides, the decreasing porosity also has positive effects on the thermal and electrical performance of the sintering layers. Therefore, pressure assisted Ag sintering has gradually become the developing trend and been used in industry. This chapter focuses on investigating the effects of sintering parameters on the bonding quality of nanosilver sintered package. The effects of sintering pressure, temperature and time on the evolution of the bonding strength and fracture properties of nanosilver sintered sandwich package are presented. Besides, the effects of sintering parameters on the bonding mechanisms of sintered silver nanoparticles are discussed.

Parts of this chapter have been published in [IEEE Transactions on Device and Materials Reliability](#) **18**, 240 (2018)

[1].

2.1. INTRODUCTION

The developments of power electronics are moving toward high-power density, high efficiency and low-power loss [2-4]. The main function of power electronics is to control and convert electric power [5, 6]. The fast development of wide band gap semiconductors facilitates the extensive application of power electronics. They have already become the key components in fields of smart grid systems, photovoltaic inverters, uninterrupted power supply, hybrid electric vehicles and high speed tractions [7, 8]. The power electronics are expected to work at temperatures higher than 350°C [9], which propose severe requirements for the corresponding packaging materials.

The power die is normally attached to the substrate through the die attach layer. This layer plays an important role in the power module including mechanical connection, electrical conduction and thermal dissipation. The die attach layer needs to withstand the high current density while maintain high temperature reliability. Among the die attach materials, the nanosilver sintering paste/film has been developed and widely been applied for attaching power dies [1, 10]. The nanosilver sintered layer has the combined advantages of high electrical and thermal conductivity because of the silver. The sintering material is mainly composed of the silver nanoparticles, which possess the low sintering driving force due to their high surface energy [11]. The sintering process is achieved at temperatures around 200 to 300°C with or without the assistance of pressure.

Fu *et al* found that the pressureless nanosilver sintered IGBT module has a higher reliability than the Sn5Pb92.5Ag2.5 soldered one [12, 13]. Wang *et al* demonstrated that a shear strength of 25 MPa can be obtained by sintering silver nanoparticles at 200°C for 20 min, but the porosity of sintered layer was as high as 35.7% [14]. Besides, the weak spots were randomly distributed in the pressureless bonded joint after sintering, which resulted in the low bonding strength [15]. In order to bond large area chips (>100mm²) in pressureless sintering process, the ultrasonic vibration was introduced into the bonding process [16]. However, the shear strength only reached 18.9 MPa at the maximum ultrasonic power. Due to the high porosity generated in the sintered Ag layer during pressureless sintering process, the reliability of sintered module is decreased. In addition, the pressureless sintering process also takes a long period (>30 min) to get the enough bonding strength [13, 17]. Therefore, in order to ensure the high reliability of sintered layer and improve the efficiency, the application of pressure is of great importance, especially for die sizes larger than 25 mm² [18]. However, limited researches focused on the systematical analysis of the sintering parameters on bonding quality of nanosilver sintered joint.

This chapter investigates the sintering parameters on the bonding quality of

nanosilver sintered joint. The effects of sintering pressure on the shear strength of sintered power package and the corresponding fracture morphologies are first analyzed. Then the effects of sintering temperature and time on the sintering properties are also studied, respectively. Finally, the effects of various sintering parameters on the densification of nanoparticles during sintering process are analyzed from the theoretical point of view.

2.2. METHODOLOGY

The nanosilver film used in this research has a thickness of 65 μm . The power package with a sandwich structure, dummy die/nanosilver sintered layer/substrate, was applied in this research. The small Molybdenum (Mo) and big Mo, coated with (Mo)/Ni/Cu/Ag on the top surface, was used as dummy die and substrate, respectively. The dimension of dummy die and substrate was $9.4 \times 9.4 \times 1.2 \text{ mm}^3$ and $13.6 \times 13.6 \times 2.0 \text{ mm}^3$, respectively. The schematic diagram of sample fabrication process is presented in Figure 2.1.

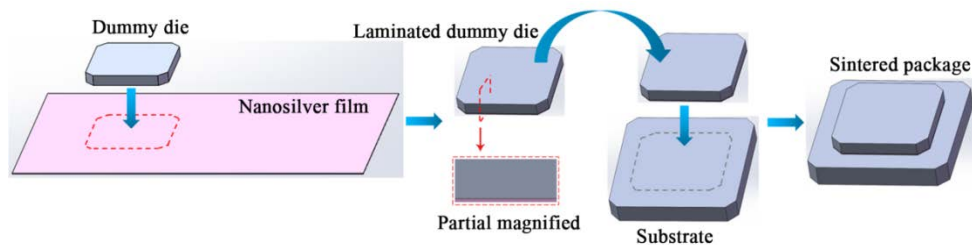


Figure 2.1: Schematic diagram of sample fabrication

The nanosilver film was first laminated to one side of the dummy die at 130°C for 2 min. The substrate was fixed in a special designed mold and then the laminated dummy die was placed on the central of the substrate. The assembled package was then sintered in the Sinterstar Innovate-F-XL at various parameters in air. The sintering parameters were summarized in Table 2.1. When investigating one parameter, the other two are fixed as a constant. Note that the sample in the line of No. 2 is the common one, which is also applicable for the other two parameters' tests. The sintering pressure was applied on the top of the dummy die and can be precisely controlled at high temperatures through the patented dynamic insert technology. The shear strength of sintered package was examined by Instron 5569 electromechanical test machine with a specially-designed fixture as shown in the Figure 2.2(a) and 2.2(b). The constant shear speed of 0.3 mm/min was used. The schematic diagram of the shear test is presented in Figure 2.2(c). The shear test was based on the standard of MIL-STD-883E, Method 2019.5. The fracture morphology of sheared package was observed by scanning electron microscopy (SEM) and the chemical composition was analyzed by energy dispersive spectrometer (EDS).

Table 2.1: Sintering parameters used in this research

No.	Pressure/ MPa	Temperature/ °C	Time/ min
1	5	250	3
2	10	250	3
3	20	250	3
4	30	250	3
5	10	210	3
6	10	230	3
7	10	270	3
8	10	250	1
9	10	250	2
10	10	250	4

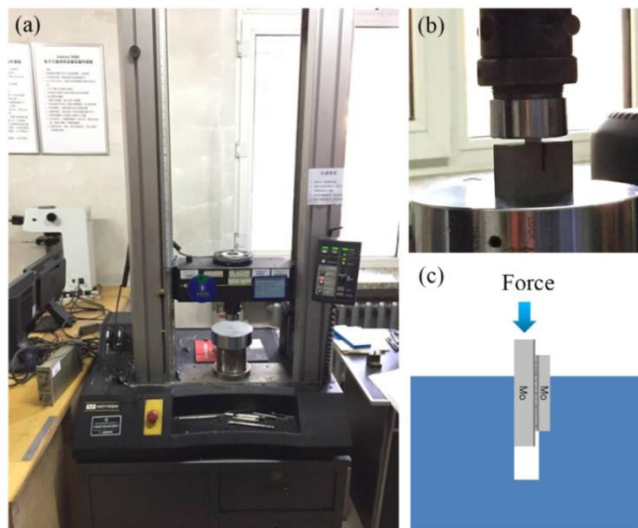


Figure 2.2: Shear tester and fixture: (a) Instron 5569 mechanical tester; (b) fixture designed for the specimens; (c) schematic diagram of the shear test

2.3. EFFECTS OF PRESSURE ON THE MECHANICAL PROPERTIES

Figure 2.3 shows the cross-sectional SEM morphologies of the sintering interfaces under the sintering pressures of 5, 10, 20, and 30 MPa, respectively. The result of the EDS line scan as shown in Figure 2.4 indicates that the top and the bottom layers are Mo. The dark layer next to the Mo layer, which consists of two elements, Ni and Cu, is formed of Ni-coated layer on the Mo plate and Cu-coated layer on Ni coated layer. Here the total

thickness of the Ni and the Cu layers is about 2 μm . The layer next to the Cu layer is the Ag-coated layer exposed to air of the Mo substrate. The thickness of this Ag-coated layer is about 5 μm .

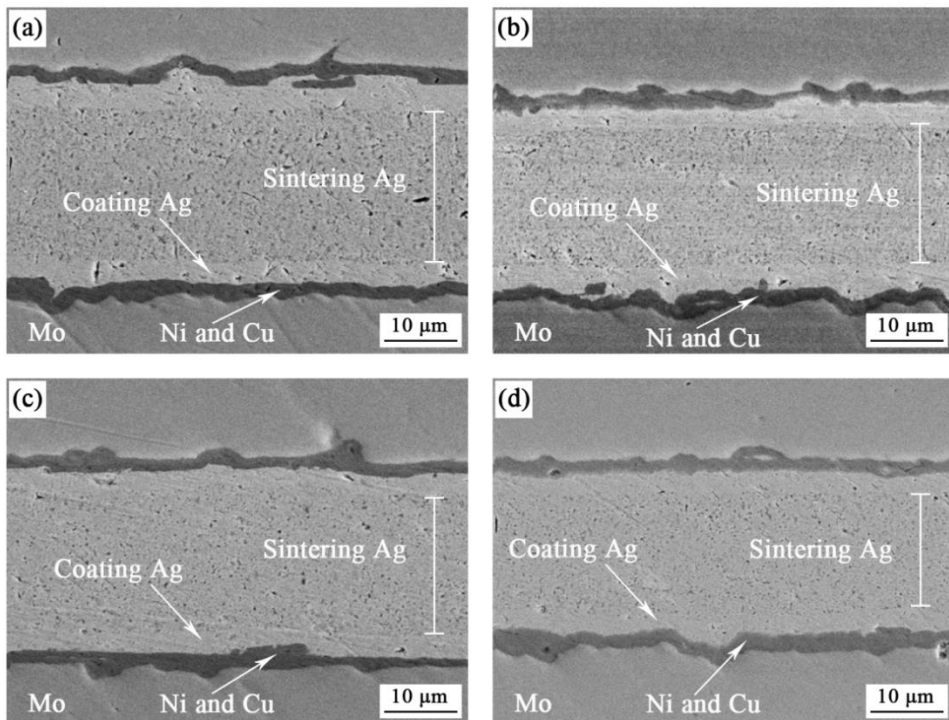


Figure 2.3: Cross-sectional SEM micrographs of the sintering interfaces under the sintering pressures of: (a) 5 MPa; (b) 10 MPa; (c) 20 MPa; (d) 30 MPa

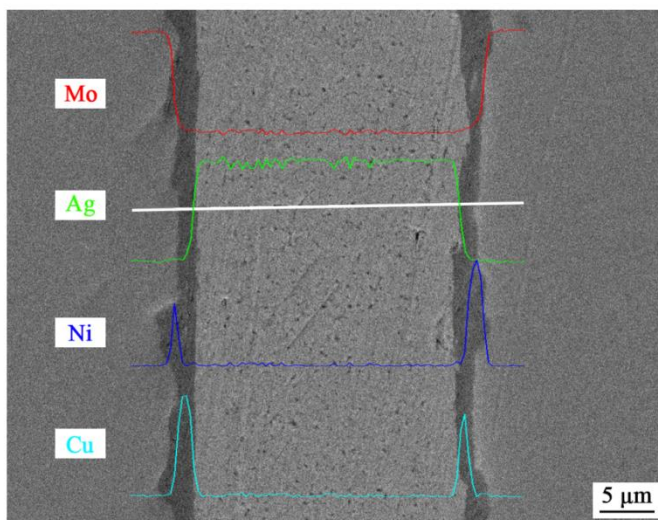


Figure 2.4: EDS line scan result of the sintering interface

The effect of sintering pressure on the mechanical properties of sintered Ag layer is shown in Figure 2.5. As the sintering pressure increases from 5 MPa to 10 MPa, the average shear strength of sintered Ag layer increases from 44.2 MPa to 69.4 MPa. This gives the maximum increase rate of 36.34%. The shear strength of 30 MPa sintered Ag layer is 73.4 MPa, which only increases slightly when comparing with the 10 MPa sintered one. These results indicate that the sintering pressure of 10 MPa is adequate to ensure the high bonding strength of sintered Ag layer and pressures higher than 10 MPa are not highly recommended.

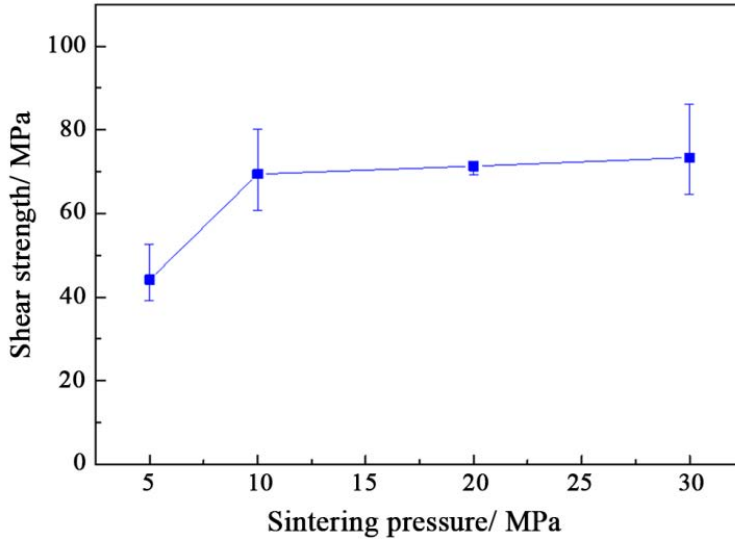


Figure 2.5: Relationship between sintering pressure and shear strength of sintered Ag layer (250°C, 3 min)

The fracture morphologies of sheared sintered packages are examined by SEM test and the results are shown in Figure 2.6 and Figure 2.7. As seen in Figure 2.6(a) and 2.6(b), the fracture area of 5 MPa sintered package is partially located at the sintered Ag layer and partially located at the interface between sintered Ag and the surface metallization layer on Mo. The EDS analysis in Figure 2.6(e) and 2.6(f) verifies these two different fracture areas, respectively. Combining the partial magnified images of sintered Ag layer in Figure 2.6(c) and 2.6(d), the sintered Ag is deformed under shear force and the fracture surface exhibits ductile morphology. The dense microstructure of sintered Ag nanoparticles can be seen in the fracture area.

When the sintering pressure increases to 30 MPa, the fracture area of sintered package occurs at the surface metallization layer on Mo, as seen in Figure 2.7(a) and 2.7(b). The chemical compositions of fracture surface are depicted in Figure 2.7(e) and 2.7(f), which represents the (Mo)/Ni/Cu metallization layer on Mo and the sintered Ag

layer, respectively. The fracture area of sintered Ag layer is partially magnified in Figure 2.7(c) and 2.7(d). There are more and deeper dimples found in the 30 MPa sintered Ag layer when comparing with the 5 MPa sintered Ag layer in Figure 2.6. The fracture surface of 30 MPa sintered Ag layer also shows ductile morphology.

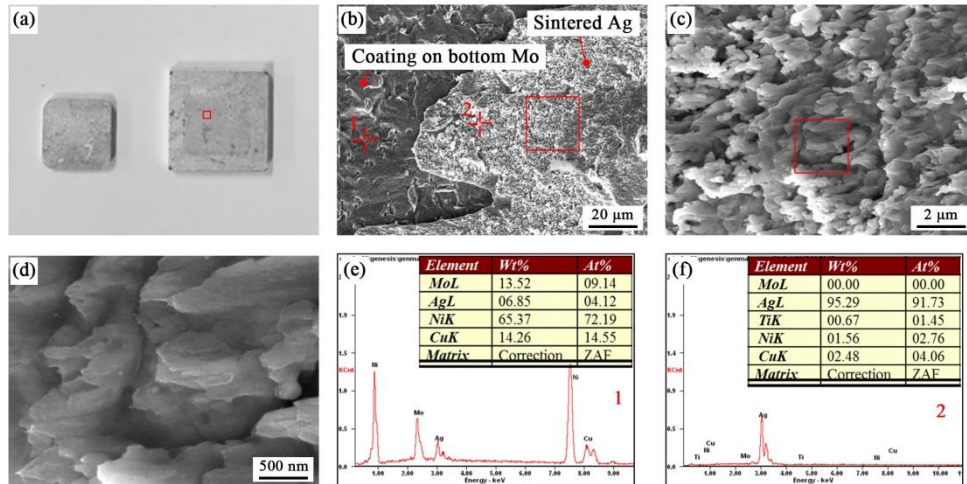


Figure 2.6: Fracture morphology of 5 MPa sintered package, (a) optical image of fracture morphology; (b), (c) and (d) are the partial magnified fracture morphology; (e) and (f) are the EDS results of 1 and 2 in (b), respectively

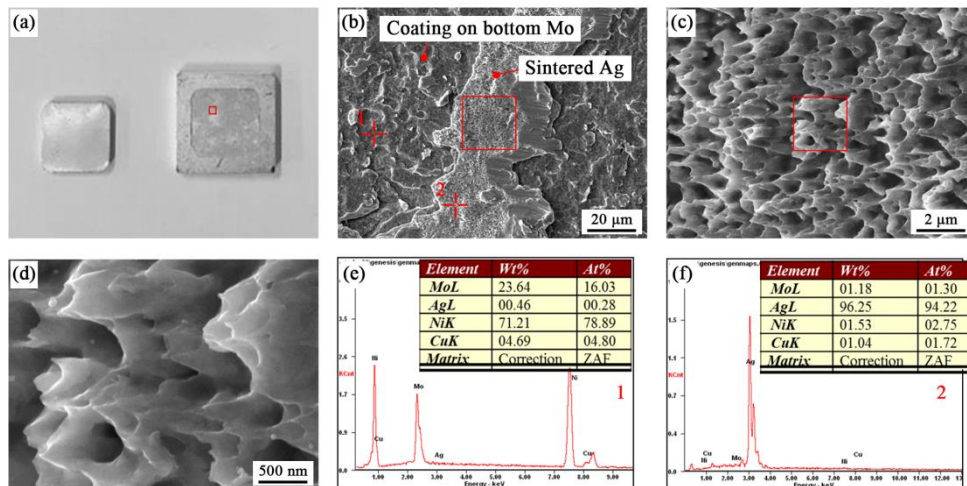


Figure 2.7: Fracture morphology of 30 MPa sintered package, (a) optical image of fracture morphology; (b), (c) and (d) are the partial magnified fracture morphology; (e) and (f) are the EDS results of 1 and 2 in (b), respectively

2.4. EFFECTS OF TEMPERATURE ON THE MECHANICAL PROPERTIES

Figure 2.8 describes the relationship between sintering temperature and average shear strength of sintered Ag layer. With the increase of sintering temperature, the shear strength of sintered Ag layer exhibits increase trend. The maximum increase rate is obtained when the sintering temperature increases from 210°C to 230°C. The shear strength of 230°C and 270°C sintered Ag layer is 68.3 MPa and 70.1 MPa, respectively. This result indicates that the shear strength of pressure assisted sintered Ag layer is not greatly affected by the temperatures higher than 230°C. According to the previous test results [19], the decomposition of organics ends around 240°C. Therefore, the temperature of 250°C is recommended in order to get the good bonding between silver nanoparticles.

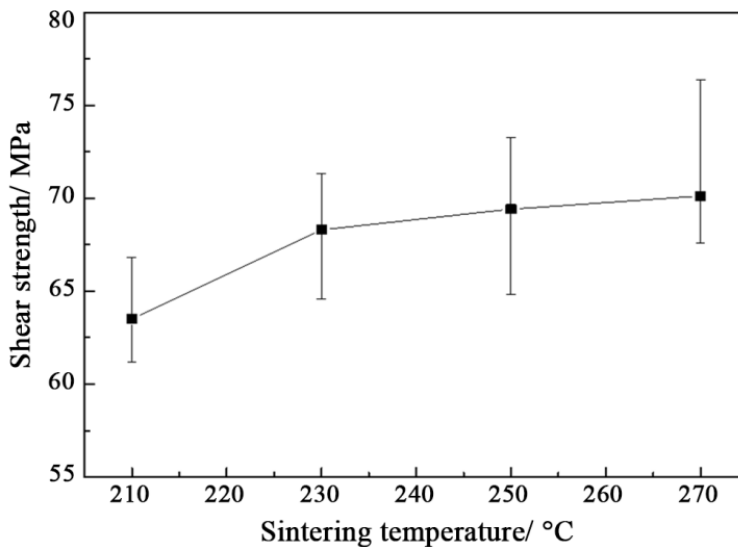


Figure 2.8: Relationship between sintering temperature and shear strength of sintered Ag layer (10 MPa, 3 min)

The fracture morphologies of 210°C sintered package are shown in Figure 2.9. The fracture area can be determined by the morphologies in Figure 2.9(a) and 2.9(b), which is mainly located at the sintered Ag layer. The sintered Ag nanoparticles in fracture area exhibits good bonding between adjacent particles. Based on the partial magnified image in Figure 2.9(c) and 2.9(d), the sintered Ag layer is quite dense and contains many dimples in the irregular fracture surface.

The fracture area of 270°C sintered package shifts to the surface metallization layer on Mo, as seen in Figure 2.10(a) and 2.10(b). The metallization layer is peeled off under shear force and partially left on the top surface of sintered Ag layer. The fracture surface is further magnified in Figure 2.10(c) and 2.10(d). Since the fracture surface is covered with

metallization layer, thus limited dimples can be observed in the magnified area. The sintered Ag nanoparticles can be identified on the top left corner in Figure 2.10(d), which is located under the metallization layer. Comparing with the 210°C sintered package, the bonding between Ag nanoparticles is greatly enhanced at 270°C and furtherly results in the change of fracture area from the sintered Ag layer to the metallization layer on Mo.

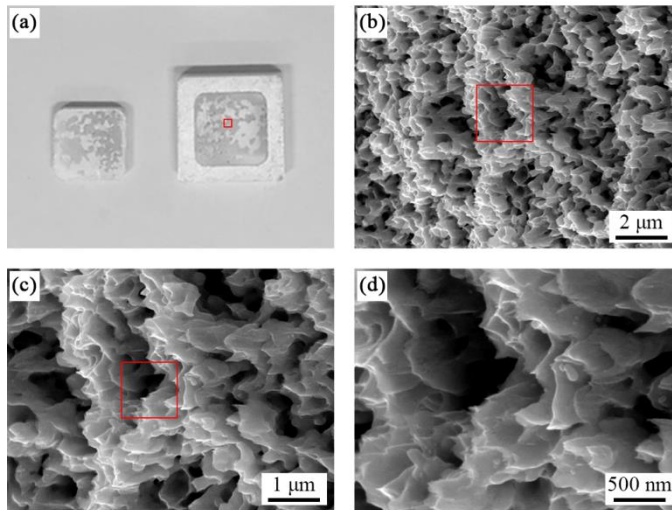


Figure 2.9: Fracture morphology of 210°C sintered package, (a) optical image of fracture morphology; (b), (c) and (d) are the partial magnified fracture morphology

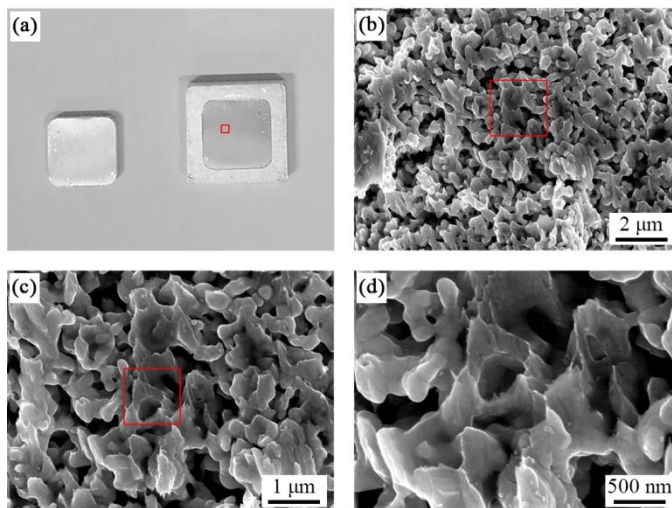


Figure 2.10: Fracture morphology of 270°C sintered package, (a) optical image of fracture morphology; (b), (c) and (d) are the partial magnified fracture morphology

2.5. EFFECTS OF TIME ON THE SHEAR MECHANICAL PROPERTIES

Figure 2.11 displays the effect of sintering time on the average shear strength of sintered Ag layer. The shear strength of 1 min and 4 min sintered package is 67.2 MPa and 71.4 MPa, respectively. There is no significant increase in the shear strength of sintered Ag layer with the increase of time when sintered at 250°C and 10 MPa. However, in order to ensure the high bonding quality of sintered Ag layer, it's better to extend the sintering time. Based on our previous work, the 3 min is chosen as the sintering time in production process.

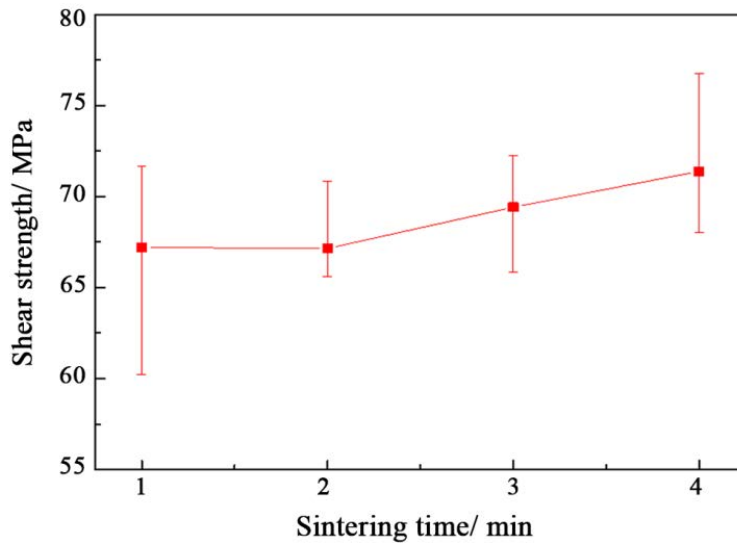


Figure 2.11: Relationship between sintering time and shear strength of sintered Ag layer (250°C, 10 MPa)

The fracture morphology of 1 min sintered package is shown in Figure 2.12. As seen in Figure 2.12(a) and 2.12(b), the sintered Ag layer is split up and the residuals are left on both top and bottom Mo. This result proves that the fracture occurs at the sintered Ag layer. The fracture morphologies of sintered Ag layer are further magnified, as shown in Figure 2.12(c) and 2.12(d). The fractured Ag nanoparticles are toward the same direction and dimples can be observed in the fracture area. Based on the fracture morphology analysis above, the fracture mode of sintered Ag layer is ductile fracture.

As the sintering time increases to 4 min, the fracture area of sintered package changes to the metallization layer on Mo, which can be verified in Figure 2.13(a) and 2.13(b). The fracture area in Figure 2.13(b) is partially magnified in Figure 2.13(c) and 2.13(d). As seen in the figure, there are a lot of dimples in the fracture surface and they show ductile morphology. There is no Ag nanoparticle can be seen in the fracture area,

since it locates under the fractured metallization layer of Mo. Comparing with the fracture morphologies in Figure 2.12, the increased sintering time enhances the bonding of Ag nanoparticles and thus results in the shift of fracture area. Table 2.2 summarizes the sintering condition, shear strength and fracture area of sintered packages.

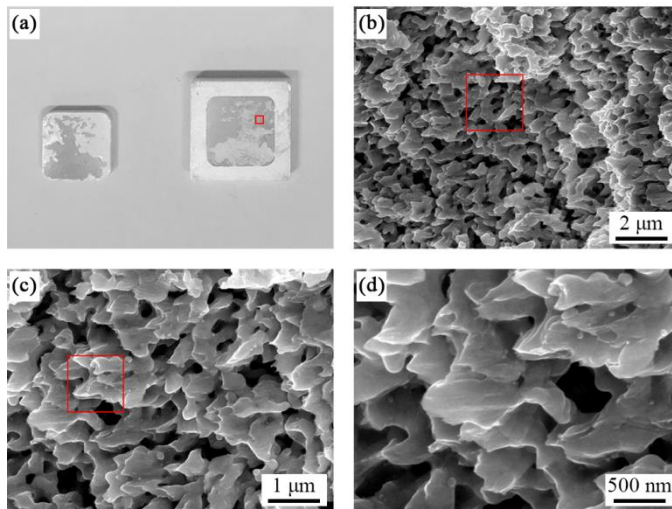


Figure 2.12: Fracture morphology of 1 min sintered package, (a) optical image of fracture morphology; (b), (c) and (d) are the partial magnified fracture morphology

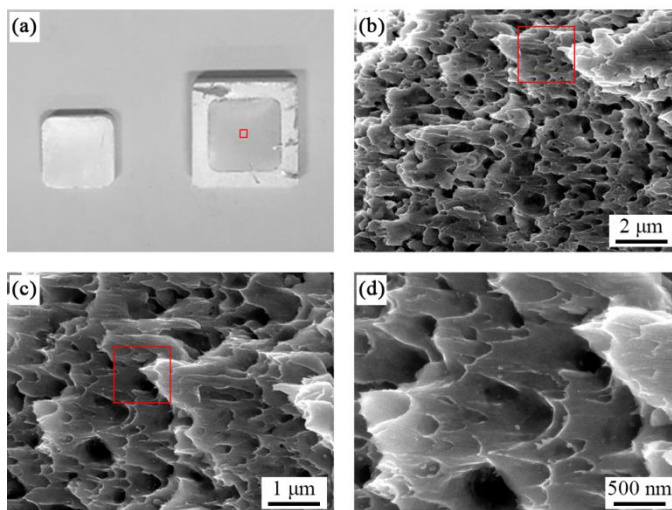


Figure 2.13: Fracture morphology of 4 min sintered package, (a) optical image of fracture morphology; (b), (c) and (d) are the partial magnified fracture morphology

Table 2.2: Summary of sintering parameters and shear performances

No.	Pressure (MPa)	Temperature (°C)	Time (min)	Shear strength (MPa)	Fracture area
1	5	250	3	44.2	Sintered Ag and interface on Mo
4	30	250	3	73.4	Metallization on Mo
5	10	210	3	63.5	Sintered Ag
7	10	270	3	70.1	Metallization on Mo
8	10	250	1	67.2	Sintered Ag
10	10	250	4	71.4	Metallization on Mo

2.6. DENSIFICATION MECHANISMS OF SILVER NANOPARTICLES

The applied pressure during sintering increases particle density and contact between nanosilver particles, and thus achieves better mechanical, electrical, and thermal properties. During sintering, the organic shells will first evaporate and allow coalescence between particles, as shown in Figure 2.14(a). The free energy of nanosilver particles decreases by reducing the surface area. Then the sintering necks are irregularly formed between adjacent particles without pressure, as depicted in Figure 2.14(b). As demonstrated by Peng *et al.* [11], the densification rate of particles during sintering process can be expressed by Eq. (2.1):

$$\frac{d\rho}{dt} = \frac{3}{2}\sigma(1-\rho)\left(1-\alpha\left(\frac{1}{\rho}-1\right)^{\frac{1}{3}}\ln\frac{1}{1-\rho}\right)\frac{1}{\eta} \quad (2.1)$$

where $d\rho/dt$ represents the densification rate, σ represents the driving force for densification, α represents the geometrical constant, ρ represents the density, and η represents the densification viscosity. Mackenzie and Shuttleworth [20] used Eq. (2.2) to express the driving force σ between two particles:

$$\sigma = \gamma\left(\frac{1}{R_1} + \frac{1}{R_2}\right) + P \quad (2.2)$$

where γ represents the surface energy of material, R_1 and R_2 represents the principal radii of curvature at the contact point, and P represents the applied pressure. Based on the equation above, it can be concluded that the densification will be enhanced by decreasing the particle size and/or increasing the applied pressure. During pressure assisted sintering process, the nanosilver particles will be compressed tighter and thus

resulting in a more and larger contact surface area as seen in Figure 2.14(c) when comparing with pressure-free sintered particles. Greater number sintering necks are formed with larger contact areas, which would further enhance the bonding quality and performance of the sintered layer. A more continuous matrix of nanosilver would then be indicative of better performance properties.

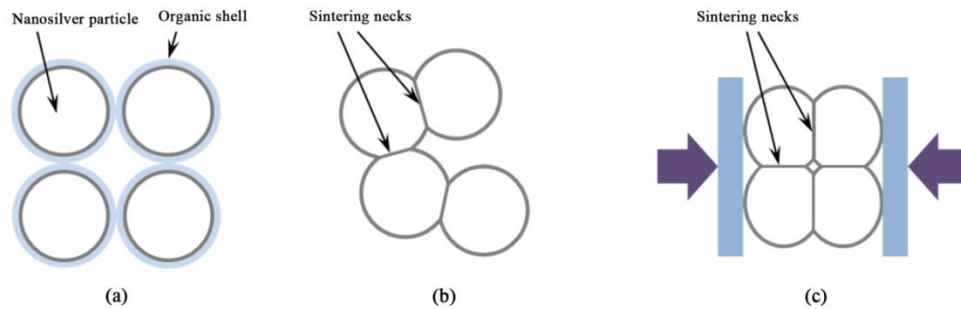


Figure 2.14: Schematic diagrams of sintered nanosilver particles, (a) original particles; (b) pressure-free sintered; (c) pressure assisted sintered

Besides the sintering pressure, the sintering temperature and time are the other two factors in affecting the properties of sintered joint. The nanosilver sintering bonding is a diffusion dominated process, which is dependent on the temperature. According to the Arrhenius equation [21], more atoms will be activated at higher sintering temperatures and facilitate the growth of sintering necks between nanoparticles. Therefore, the shear strength of sintered layer will be enhanced by the increased size and number of sintering necks. In addition, it is suggested that the grain size increases with the increase of sintering time [22]. The increase of grain size promotes the diffusion between nanosilver particles to form larger sintering necks, which furtherly enhances the shear strength of sintered layer. Besides, more organics inside the nanosilver film will evaporate with the increase of sintering time, which could be another reason for the enhancement of bonding strength. With the help of sintering pressure, the effects of sintering temperature and time on improving the bonding of nanosilver particles become insignificant.

2.7. SUMMARY

The sintering pressure exhibits significant effects on enhancing the bonding strength of sintered nanosilver layer. As the sintering pressure increases from 5 MPa to 10 MPa, the shear strength of sintered Ag layer increases from 44.2 MPa to 69.4 MPa. Further increase of the sintering pressure exhibits limited effect on enhancing on the shear strength in this study. Thus, the sintering pressure of 10 MPa is suitable for the sintering of nanosilver

particles. The fracture area of sintered package changes from the sintered Ag layer to the surface metallization layer on Mo when the sintering pressure increases from 5 MPa to 30 MPa sintering pressure.

With the increase of sintering temperature, the shear strength of sintered Ag layer exhibits increase trend. However, no obvious increase is found in the shear strength of pressure assisted sintered Ag layer when sintered at temperatures higher than 230°C. In order to achieve the maximum evaporation of organics in the nanosilver film, the sintering temperature of 250°C is recommended. Similar shifts of the fracture area are found as pressure effects when the sintering temperature increased from 210°C to 270°C. The shear strength of sintered Ag layer increased slightly with the increase of time from 1 min to 4 min when sintered at 250°C and 10 MPa. In order to ensure the adequate diffusion of nanosilver particles, the sintering time of 3 min is chosen. The fracture area of 1 min and 4 min sintered package is located at the sintered Ag layer and the surface metallization layer on Mo, respectively.

It is suggested that the applied sintering pressure directly enlarges the contact surface between silver nanoparticles and thus greatly enhances the bonding strength of sintered Ag layer. The number of activated atoms increases with the increase of sintering temperature and promotes the growth of sintering necks, which furtherly resulted in the increase of corresponding shear strength. The increase of sintering time extends the growth time for grains and thus improves the bonding strength of sintered layer. In addition, the organics inside the nanosilver film are expected to evaporate more sufficient with the increase sintering time. However, because of the application of sintering pressure, the sintering temperature and time are less significant in enhancing the bonding strength of sintered layer when comparing to the pressure effects.

REFERENCES

- [1] Y. Liu, H. Zhang, L. Wang, X. Fan, G. Zhang, and F. Sun, *Effect of sintering pressure on the porosity and the shear strength of the pressure-assisted silver sintering bonding*, IEEE Transactions on Device and Materials Reliability **18**, 240 (2018).
- [2] J.G. Kassakian and T.M. Jahns, *Evolving and emerging applications of power electronics in systems*, IEEE Journal of Emerging and Selected Topics in Power Electronics **1**, 47 (2013).
- [3] K.S. Siow, *Are sintered silver joints ready for use as interconnect material in microelectronic packaging?*, Journal of Electronic Materials **43**, 947 (2014).
- [4] H.S. Chin, K.Y. Cheong, and A.B. Ismail, *A review on die attach materials for*

- SiC-based high-temperature power devices*, Metallurgical and Materials Transactions B **41**, 824 (2010).
- [5] B. Ji, X. Song, E. Sciberras, W. Cao, Y. Hu, and V. Pickert, *Multiobjective design optimization of IGBT power modules considering power cycling and thermal cycling*, IEEE Transactions on Power Electronics **30**, 2493 (2015).
- [6] F. Iacopi, M. Van Hove, M. Charles, and K. Endo, *Power electronics with wide bandgap materials: Toward greener, more efficient technologies*, MRS Bulletin **40**, 390 (2015).
- [7] X. She, A.Q. Huang, Ó. Lucía, and B. Ozpineci, *Review of silicon carbide power devices and their applications*, IEEE Transactions on Industrial Electronics **64**, 8193 (2017).
- [8] I. Colak, E. Kabalci, G. Fulli, and S. Lazarou, *A survey on the contributions of power electronics to smart grid systems*, Renewable and Sustainable Energy Reviews **47**, 562 (2015).
- [9] H.A. Mustain, W.D. Brown, and S.S. Ang, *Transient liquid phase die attach for high-temperature silicon carbide power devices*, IEEE Transactions on Components and Packaging Technologies **33**, 563 (2010).
- [10] Z. Zhang and G.Q. Lu, *Pressure-assisted low-temperature sintering of silver paste as an alternative die-attach solution to solder reflow*, IEEE Transactions on Electronics Packaging Manufacturing **25**, 279 (2002).
- [11] P. Peng, A. Hu, A.P. Gerlich, G. Zou, L. Liu, and Y.N. Zhou, *Joining of silver nanomaterials at low temperatures: processes, properties, and applications*, ACS Applied Materials & Interfaces **7**, 12597 (2015).
- [12] S. Fu, Y. Mei, X. Li, C. Ma, and G.Q. Lu, *Reliability evaluation of multichip phase-leg IGBT modules using pressureless sintering of nanosilver paste by power cycling tests*, IEEE Transactions on Power Electronics **32**, 6049 (2017).
- [13] S. Fu, Y. Mei, X. Li, C. Ma, and G.Q. Lu, *A multichip phase-leg IGBT module bonded by pressureless sintering of nanosilver paste*, IEEE Transactions on Device and Materials Reliability **17**, 146 (2017).
- [14] S. Wang, H. Ji, M. Li, and C. Wang, *Fabrication of interconnects using pressureless low temperature sintered Ag nanoparticles*, Materials Letters **85**, 61 (2012).
- [15] H. Ogura, M. Maruyama, R. Matsubayashi, T. Ogawa, S. Nakamura, T. Komatsu, H. Nagasawa, A. Ichimura, and S. Isoda, *Carboxylate-passivated silver nanoparticles*

- and their application to sintered interconnection: a replacement for high temperature lead-rich solders*, Journal of Electronic Materials **39**, 1233 (2010).
- [16] Y. Li, H. Jing, Y. Han, L. Xu, and G. Lu, *Microstructure and joint properties of nano-silver paste by ultrasonic-assisted pressureless sintering*, Journal of Electronic Materials **45**, 3003 (2016).
- [17] J. Li, X. Li, L. Wang, Y.H. Mei, and G.Q. Lu, *A novel multiscale silver paste for die bonding on bare copper by low-temperature pressure-free sintering in air*, Materials & Design **140**, 64 (2018).
- [18] T. Wang, M. Zhao, X. Chen, G.Q. Lu, and S. Luo, *Shrinkage and sintering behavior of a low-temperature sinterable nanosilver die-attach paste*, Journal of Electronic Materials **41**, 2543 (2012).
- [19] H. Zhang, Y. Liu, L. Wang, F. Sun, J. Fan, M.D. Placette, X. Fan, and G. Zhang, *Effects of sintering pressure on the densification and mechanical properties of nanosilver double side sintered power module*, IEEE Transactions on Components, Packaging and Manufacturing Technology **9**, 963 (2019).
- [20] J. Mackenzie and R. Shuttleworth, *A phenomenological theory of sintering*, Proceedings of the Physical Society. Section B **62**, 833 (1949).
- [21] R.M. German, *Thermodynamics of sintering*, Sintering of Advanced Materials **20**, 3 (2010).
- [22] S. Fu, Y. Mei, X. Li, P. Ning, and G.Q. Lu, *Parametric study on pressureless sintering of nanosilver paste to bond large-area ($\geq 100 \text{ mm}^2$) power chips at low temperatures for electronic packaging*, Journal of Electronic Materials **44**, 3973 (2015).

3

MICRO MECHANICAL PROPERTIES OF PRESSURE SINTERED NANOSILVER JOINT

In order to meet the severe requirements proposed by the working condition of high power electronics, the high temperature stability of nanosilver sintered layer has important significance in ensuring the steady operation of the whole system. This chapter focuses on investigating the high temperature micro mechanical properties of nanosilver sintered layer, while taking the sintering pressure effect into consideration. The nanoindentation test is conducted to study the plasticity, indentation hardness, elastic modulus and initial creep properties of sintered joint. The strain rate shows obvious effect on the indentation hardness of sintered layer, especially at low strain rates. The yield stress and strain hardening exponent are obtained and furtherly employed in the plastic stress-strain constitutive equation of nanosilver sintered joint at various sintering pressures. The effects of temperature and sintering pressure on the evolution of maximum indentation depth of nanosilver sintered joint are presented in this chapter. The relationship between indentation hardness and temperature is discussed while combining the sintering pressure effects. The evolution of elastic modulus of nanosilver sintered joint exhibits similar trend as the indentation hardness with increasing temperature and pressure. The initial creep is observed in nanosilver sintered joint at temperatures ranged from 140°C to 200°C. The decrease of maximum creep displacement with increasing sintering pressure proves the enhanced resistance to creep of nanosilver sintered joint.

Parts of this chapter have been published in [Results in Physics 12, 712 \(2018\)](#) [1].

3.1. INTRODUCTION

Power electronic modules, which are expected to work in severe environments, have been regarded as the critical part in many fields including transportation (hybrid electric vehicles/electric vehicles, traction systems), utilities (smart grids, photovoltaic power and wind power systems), industries (motor drivers, electric machinery) and consumer products (uninterruptible power supplies, battery chargers) [2-4]. The power electronics are generally used to realize the conversion and transmission of electricity [5]. The first level interconnection is usually achieved through a die attach layer between power die and ceramic substrate. Consequently, the die attach layer plays an important role in ensuring the thermal and electrical conduction in power electronic modules. During the operation process of power electronics, temperature change occurs due to the periodical application of electric power [6]. Since the coefficient of thermal expansion is variable in each layer, so thermo-mechanical stress is expected to generate in the die attach layer. Therefore, the thermal reliability of die attach layer greatly affects the performance of power electronics.

The nanosilver sintering technology has gained high popularity in attaching power dies in power electronics packaging [7-9], and the reliability investigation of nanosilver sintered joint has become the mainstream in recent years. Zhao *et al* [10] found that the fracture morphology of nanosilver sintered joint exhibited significant plastic flow during shear test, which implied the high bonding strength. Similar result was also obtained by Fu *et al* [11]. Bai *et al* [12] proved that the dislocation creeps were produced in sintered silver die attach layer during thermal cycling test. The pile-up of dislocation creeps promoted the formation of microcavities at the grain boundaries and finally resulted in the decrease of shear strength. Li *et al* [13] investigated the creep behavior of nanosilver sintered lap shear joint, and the results showed that the creep strain of nanosilver sintered joint increased with the increase of temperature from 225°C to 325°C. Chen *et al* [14] found that the accumulation of creep strain of nanosilver sintered thin film became faster as the temperature increasing from 100°C to 175°C. This result indicated that the higher temperature would lead to a shorter creep rupture life. The nanoindentation test method is usually used to characterize the plastic deformation and creep behavior of materials on nano/microscale [15-17]. This technology has been used to investigate the room temperature viscoplastic properties of silver sintered joint [18, 19]. However, the silver sintered joint is expected to serve at high temperatures and there are few researches reporting on the high temperature indentation properties of nanosilver sintered joint while incorporating pressure effects.

This chapter investigates the indentation hardness, plasticity and initial creep

properties of pressure sintered nanosilver joint. The nanoindentation test is conducted at various temperatures. The effects of strain rate on the indentation hardness are first analyzed. Then the elastoplastic behaviors of nanosilver sintered joint at room temperature are discussed. What's more, the temperature dependence of indentation depth, hardness and modulus are studied, respectively. Besides, the effects of temperature on the evolution of initial creep behavior of nanosilver sintered joint are analyzed.

3.2. METHODOLOGY

The commercial Argomax 2020 (from Alpha Assembly Solutions) [20] nanosilver film with thickness of 65 μm was used as the sintering material. The molybdenum (Mo) coated with (Mo)/Ni/Cu/Ag on both sides was used as substrate. The upper one was named as top Mo substrate and lower one was to be the bottom Mo substrate. The dimension of Mo substrate was $13.60 \times 13.60 \times 2.00 \text{ mm}^3$. The nanosilver film was first transferred to the bottom Mo substrate through a lamination process at 130°C and 5 MPa pressure for 2 min. Then the top Mo substrate was placed on the laminated bottom Mo substrate and sintered at 250°C for 3 min with various pressures. The schematic diagram of fabrication process was shown in Figure 3.1. In order to investigate the effects of pressure on the mechanical properties of nanosilver sintered joint, the sintering pressure was respectively set as 5, 10, 20, 30 MPa for each sintering process. After sintering, the sample was grinded and polished with 0.25 μm suspension of diamond for the nanoindentation test. The scanning electron microscope was also used to examine the morphology of polished sample to ensure the quality of sintered layer. In order to ensure the high accuracy of tests, only the central part of the sintered layer was used in the nanoindentation test.

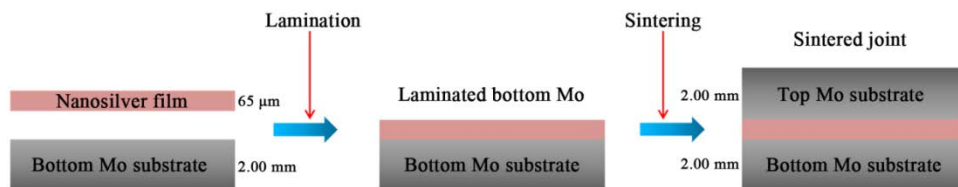


Figure 3.1: Schematic diagram of sample structure (not drawn to scale)

The SHIMADZU Dynamic Ultra-micro Hardness Tester (DUH-211S) was used to characterize the micro mechanical properties of nanosilver sintered joint. This tester was equipped with the 115° Berkovich indenter. The Berkovich indenter is the most widely used one to characterize the plasticity of bulk materials. The loading-holding-unloading

mode was applied to the test and the holding time was set as 10 s. The indentation test was first conducted at room temperature at 5 mN loading force. The strain rate of 0.004, 0.02, 0.1 and 0.2 s⁻¹ were selected for investigating its effect on indentation hardness. The strain rate is obtained through dividing the loading speed by loading force. The cross section morphology of 30 MPa sintered nanosilver joint was shown in Figure 3.2(a). The indentation morphology tested at 25°C and 0.2 s⁻¹ was shown in Figure 3.2(b). The high temperature tests were achieved with the help of micro heater assembled in the DUH-211S. The temperature referred here was the temperature on the test sample, which was measured and controlled precisely through the whole indentation test. The test was conducted at 140, 160, 180 and 200°C, respectively. The temperature selected here was based on the basic temperature requirement for the occurrence of creep: $T/T_m > 0.3$, where T is the test temperature, T_m is the melting point of material, all in Kelvin temperature. Here, the melting point of 961°C was used for sintered Ag. So the calculated value for 140, 160, 180 and 200°C was 0.33, 0.35, 0.37, 0.38, respectively. The selected temperature can ensure the occurrence of creep and the validity of the tests. The test force and strain rate for high temperature test was respectively set as 5 mN and 0.2 s⁻¹. Each data was the average value of at least 9 tests at the same condition. The Oliver and Pharr method was used to determine the hardness and elastic modulus of tested sample [21]. Previous results revealed that the porosity of sintered nanosilver joint decreased from 1.39% to 1.14% as the sintering pressure increased from 5 MPa to 30 MPa [7]. The low porosity as well as the difference of porosity have limited effect on the change of the Poisson's ratio according to the calculation method adopted by Long *et al* [22]. So, the Poisson's ratio of 0.37 for pure Ag is used for the nanoindentation tests in this paper.

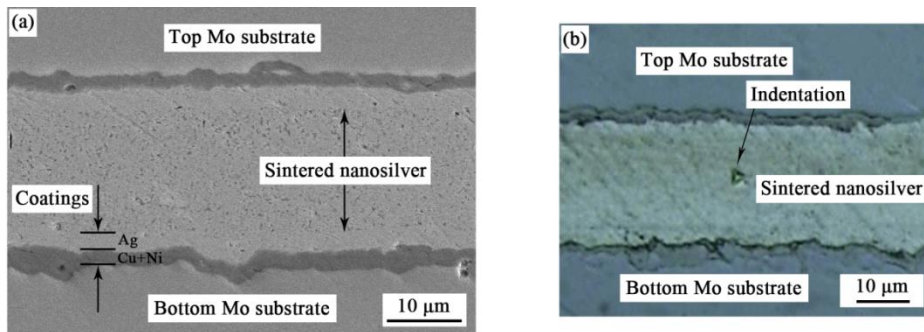


Figure 3.2: Morphology of 30 MPa sintered nanosilver joint, (a) cross section; (b) after indentation

3.3. EFFECTS OF STRAIN RATE ON THE INDENTATION HARDNESS

Since the strain rate plays an important role in determining the mechanical properties of materials [22], the nanosilver sintered joint is tested at 25°C under various strain rates.

The evolution of indentation hardness with increasing strain rate for 5 MPa sintered nanosilver joint is shown in Figure 3.3. With the increase of strain rate from 0.004 to 0.02 s^{-1} , the indentation hardness (H_{IT}) of nanosilver sintered joint increases sharply. However, the increase rate of H_{IT} decreases as the strain rate increasing from 0.02 s^{-1} to 0.1 s^{-1} . Limited effect is observed on H_{IT} when the strain rate reaches 0.2 s^{-1} . It is suggested that the indentation size is larger at low strain rate when comparing with the one tested at high strain rate [23]. According to Eq. (3.1) [24], the larger indentation size A_c will result in higher indentation hardness H_{IT} at the same loading force F_{max} . This effect becomes insignificant when the strain rate increases to certain level. So the strain rate of 0.2 s^{-1} is chosen for the following tests.

$$H_{IT} = \frac{F_{max}}{A_c} \quad (3.1)$$

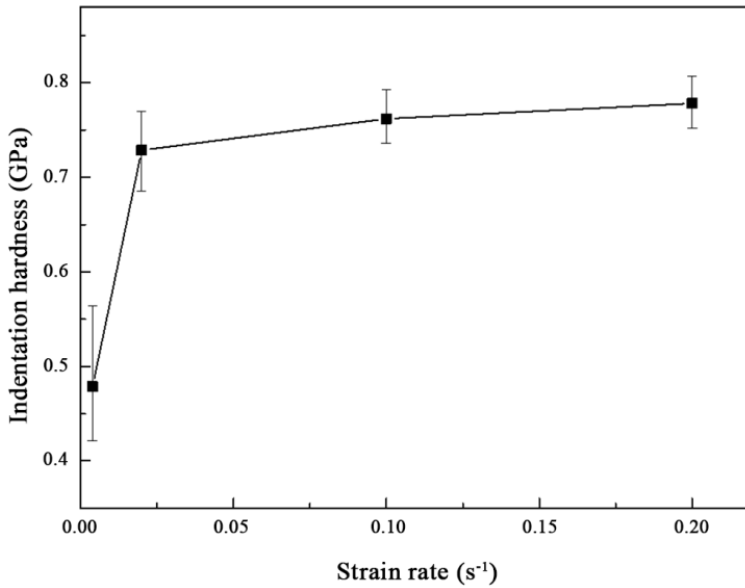


Figure 3.3: Relationship between indentation hardness and strain rate of 5 MPa sintered nanosilver joint

3.4. PLASTIC STRESS-STRAIN CONSTITUTIVE MODEL AT ROOM TEMPERATURE

During nanoindentation test, the nanosilver sintered joint deforms as the indentation load increases and elastic deformation occurs at the beginning stage. Once the indentation load exceeds the yield strength of sintered joint, plastic deformation happens and leads to the irreversible deformation. Since the residual indentation depth is recorded after the nanoindentation test, so the deformation of nanosilver sintered

joints consist of both elastic and plastic deformation. The stress (σ)-strain (ε) behavior of sintered joint can be expressed in general form as follows [25-27]:

$$\sigma = \begin{cases} E\varepsilon & (\sigma \leq \sigma_y) \\ \sigma_y \left(1 + \frac{E}{\sigma_y} \varepsilon_p\right)^n & (\sigma > \sigma_y) \end{cases} \quad (3.2)$$

where E represents the elastic modulus of tested material, σ_y represents the initial yield stress, ε_p represents the plastic strain, n represents the strain hardening exponent. There is an empirical equation describing the relationship between yield stress σ_y and hardness H_{IT} as seen in Eq. (3.3) [28]:

$$\sigma_y \approx \frac{H_{IT}}{3} \quad (3.3)$$

The strain hardening exponent (n) can be calculated according to literature [29]. The σ_y and n for various pressures sintered nanosilver joint are summarized in Table 3.1. As the sintering pressure increases from 5 MPa to 30 MPa, the yield stress σ_y of nanosilver sintered joint increases. This result implies that the strength of nanosilver sintered joint can be enhanced by increasing the sintering pressure. In addition, the strain hardening exponent n exhibits increase trend with increasing pressure. The increase of n indicates the increased capability of bearing loading force, which also means the improvement of resistance to plastic deformation. Combining with Eq. (3.2), the plastic stress-strain constitutive equations of nanosilver sintered joint with various sintering pressures at room temperature are gained and shown in Table 3.2.

Table 3.1: The σ_y and n of nanosilver sintered joint with various sintering pressures (25°C)

	5 MPa	10 MPa	20 MPa	30 MPa
σ_y (GPa)	0.26	0.33	0.64	0.67
n	0.43	0.47	0.48	0.48

3.5. EFFECTS OF TEMPERATURE ON THE MICRO MECHANICAL PROPERTIES

3.5.1. EVOLUTION OF INDENTATION DEPTH

Figure 3.4 is the evolution of indentation load-depth curve of 5 MPa sintered nanosilver joint at 25, 140, 160 and 200°C test temperatures. The indentation load-depth curve consists of three stage, the loading stage, holding stage and unloading stage. As seen in

Figure 3.4, the maximum indentation depth (h_{max}) increases from 0.51 μm to 1.81 μm as the test temperature increases from 25°C to 200°C. The h_{max} at 200°C is approximately three times higher than that tested at 25°C. Besides, the slope of loading stage becomes smaller at 200°C when comparing with the sample tested at 25°C. The slope reflects the increase rate of indentation depth, the smaller the slope, the larger the increase rate of indentation depth. Similar trends are also found in 10, 20 and 30 MPa sintered nanosilver joint.

Table 3.2: Plastic stress-strain constitutive equation of nanosilver sintered joint (25°C)

Sintering pressure	Plastic stress-strain constitutive equation	
5 MPa	$\sigma = \begin{cases} 31.72\varepsilon & (\sigma \leq 0.26 \text{ GPa}) \\ 0.26(1 + 120.22\varepsilon_p)^{0.43} & (\sigma > 0.26 \text{ GPa}) \end{cases}$	
10 MPa	$\sigma = \begin{cases} 39.93\varepsilon & (\sigma \leq 0.33 \text{ GPa}) \\ 0.33(1 + 122.65\varepsilon_p)^{0.47} & (\sigma > 0.33 \text{ GPa}) \end{cases}$	
20 MPa	$\sigma = \begin{cases} 66.73\varepsilon & (\sigma \leq 0.64 \text{ GPa}) \\ 0.64(1 + 104.64\varepsilon_p)^{0.48} & (\sigma > 0.64 \text{ GPa}) \end{cases}$	
30 MPa	$\sigma = \begin{cases} 81.83\varepsilon & (\sigma \leq 0.67 \text{ GPa}) \\ 0.67(1 + 122.69\varepsilon_p)^{0.48} & (\sigma > 0.67 \text{ GPa}) \end{cases}$	

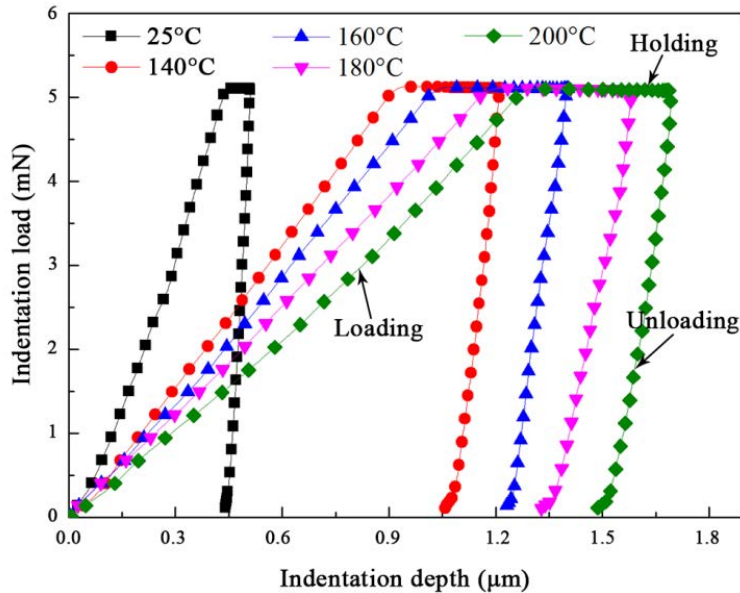


Figure 3.4: Indentation load-depth curves of 5 MPa sintered nanosilver joint at various temperatures

But the h_{max} exhibits difference in various pressures sintered nanosilver joint. The corresponding results are summarized in Figure 3.5. The difference of h_{max} between 25°C and 200°C in 5, 10, 20 and 30 MPa sintered joint is 1.30, 0.67, 0.43 and 0.29 μm , respectively. The value of difference decreases gradually with the increase of sintering pressure. This result implies that the sensitivity of h_{max} to temperature during nanoindentation test decreases with increasing sintering pressure from 5 MPa to 30 MPa. Meanwhile, the result also indicates that the resistance to elastoplastic deformation of nanosilver sintered joint can be greatly enhanced by increasing the sintering pressure. In the serving process of nanosilver sintered package, stress induced deformation occurs due to the mismatch of coefficients of thermal expansion (CTE). The reliability of nanosilver sintered joint can be improved due to its increased resistance to the deformation when sintered with pressures.

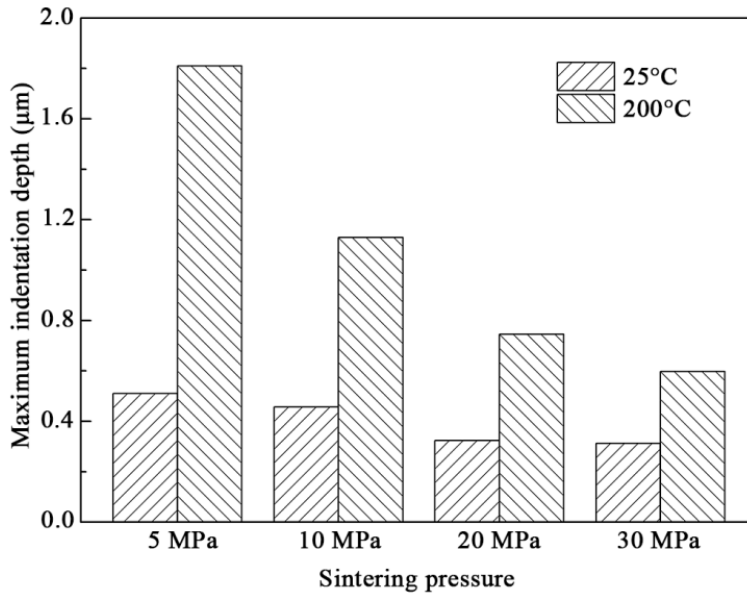


Figure 3.5: Effects of temperature and pressure on the maximum indentation depth of nanosilver sintered joints

3.5.2. TEMPERATURE DEPENDENCE OF HARDNESS

Figure 3.6 shows the relationship between indentation hardness (H_{IT}) and test temperature for various pressures sintered joints. With the increase of temperature, the H_{IT} presents decrease trend in all the four pressures sintered joints. This result indicates that the softening phenomenon happens in nanosilver sintered joint at high temperatures. Thus, the resistance to plastic deformation of sintered joint decreases and furtherly leads to the decrease of H_{IT} accordingly. It is suggested that the amount of thermal vacancies is increasing exponentially with temperature [30]. This follows the

Arrhenius type behavior:

$$n_v = n \times \exp\left(-\frac{Q_v}{RT}\right) \quad (3.4)$$

where n_v is the number of vacancies, n is the number of atoms, Q_v is the energy required to produce one mole of vacancies, R is the gas constant, T is the temperature in degrees Kelvin. Therefore, the concentration of vacancies increases exponentially as increasing the temperature. The activity of dislocation can be enhanced by the generated thermal vacancies at elevated temperature and therefore results in the decrease of indentation hardness [31]. In addition, the H_{IT} increases with the increase of sintering pressure at the same test temperature. The diffusion bonding among nanosilver particles can be greatly enhanced with the help of sintering pressure. This will further result in greater number and larger area of sintering necks. The hardness of sintered layer can be improved by the increased bonding quality at high pressures.

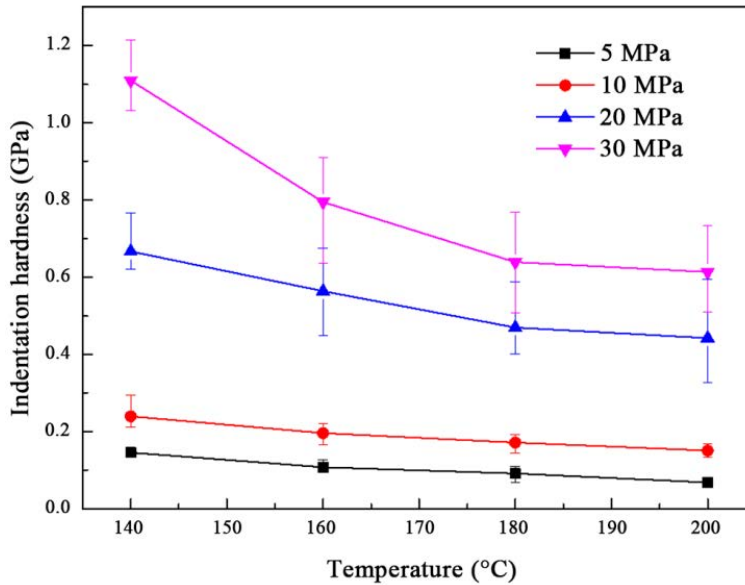


Figure 3.6: Relationship between indentation hardness and temperature of pressure sintered nanosilver joint

3.3.1. TEMPERATURE DEPENDENCE OF ELASTIC MODULUS

The evolution of indentation modulus (E_{IT}) of pressure sintered nanosilver joint at high temperatures is shown in Figure 3.7. The E_{IT} increases with the increase of sintering pressure. The E_{IT} of 5 MPa and 30 MPa sintered joint at 140°C is 8.98 GPa and 24.71 GPa, respectively. The E_{IT} has increased 2.75 times when the sintering pressure increases from 5 MPa to 30 MPa. The increase of E_{IT} can be attributed to enhanced bonding between

nanosilver particles under high sintering pressures. However, the E_{IT} of pressure sintered nanosilver sintered joint decreases with the increase of temperature from 140°C to 200°C, as seen in Figure 3.7. Similar trend is observed in all four different pressures sintered joints. It has been revealed that the E_{IT} decreases with increasing temperature T , which can be described as follows [32, 33]:

$$E_{IT} = A + B * T \quad (3.5)$$

where A and B are the constants in the equation, which can be obtained from the fitted curve in Figure 3.7. The relationship between E_{IT} and T for various pressures sintered joint is summarized in Table 3.3. It has been revealed that the elastic modulus of a material is inversely proportional to the distance between adjacent atoms [34]. The distance between atoms in sintered joint becomes larger at elevated temperatures, which will result in the smaller indentation modulus.

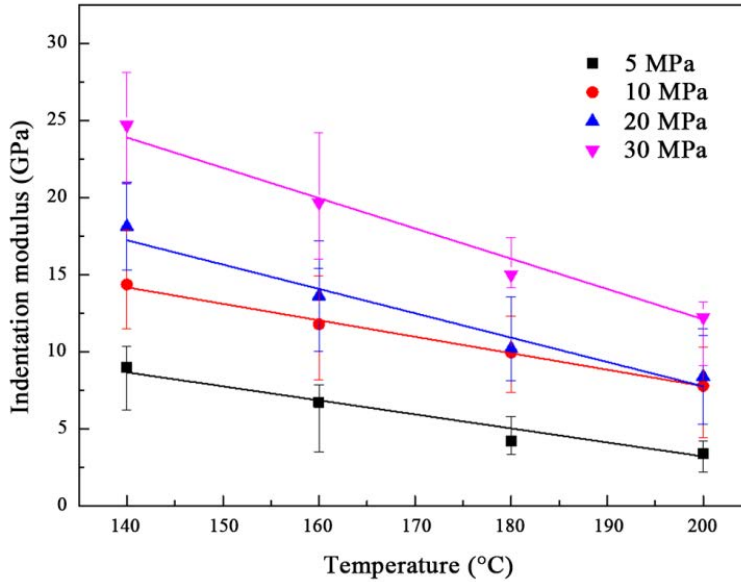


Figure 3.7: Relationship between indentation modulus and temperature of sintered nanosilver joint

Table 3.3 Relationship between H_{IT} and T for various pressures sintered nanosilver joint

Sintering pressure	Relationship between H_{IT} and T	
5 MPa	$E_{IT} = 21.41 - 0.09T$	$T \in (140 \sim 200^\circ\text{C})$
10 MPa	$E_{IT} = 29.14 - 0.11T$	$T \in (140 \sim 200^\circ\text{C})$
20 MPa	$E_{IT} = 39.36 - 0.16T$	$T \in (140 \sim 200^\circ\text{C})$
30 MPa	$E_{IT} = 51.43 - 0.20T$	$T \in (140 \sim 200^\circ\text{C})$

3.6. INITIAL CREEP BEHAVIOR OF NANOSILVER SINTERED JOINT

The initial creep behavior of nanosilver sintered joint at various temperatures is investigated through nanoindentation test. The creep displacement of nanosilver sintered joint during holding stage is extracted from the load-depth curve and then plotted with creep time. The creep behavior of 5 MPa sintered joint is displayed in Figure 3.8(a), the result shows that the evolution of creep displacement exhibits similar trend at four test temperatures. The creep displacement becomes larger as the temperature increasing from 140°C to 200°C. The creep displacement increases quickly at the initial creep stage, especially at the first 5 s. The higher the test temperature, the larger the increase rate of initial creep displacement. However, the increase rate of creep displacement decreases gradually after 5 s. As for 10, 20 and 30 MPa nanosilver sintered joint, similar creep law is also observed, as seen in Figure 3.8(b), 3.8(c) and 3.8(d).

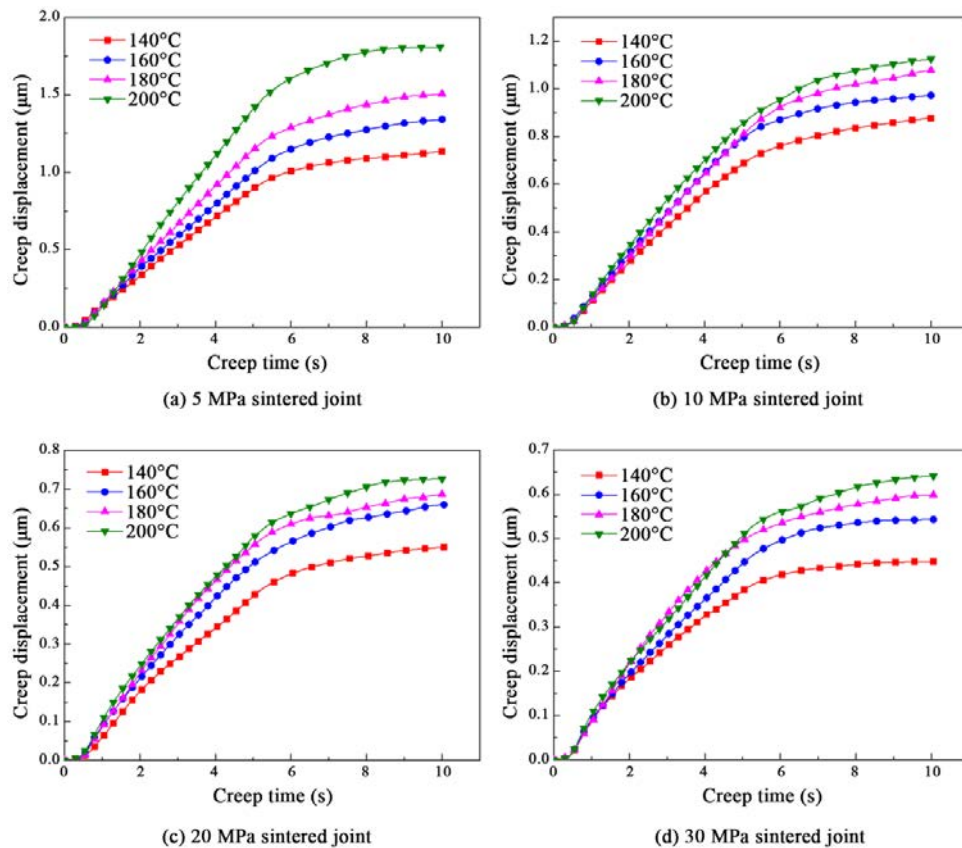


Figure 3.8: The creep time-displacement curves of pressure sintered nanosilver joint

But the maximum creep displacement after 10 s is quite different in various pressures sintered joint. With the increase of sintering pressure, the maximum creep

displacement decreases at the same temperature. The creep displacement at 200°C is much larger than the value obtained at 140°C in 5 MPa sintered nanosilver joint. But this difference becomes quite small in 30 MPa sintered joint, as seen in Figure 3.8(a) and 3.8(d). These results indicate that the resistance to creep of nanosilver sintered joint can be improved by increasing the sintering pressure. The growth of sintering neck between nanoparticles can be enhanced by increasing the sintering pressure from 5 to 30 MPa, which furtherly results in the increase of bonding strength of sintered nanoparticles and strengthens its resistance to creep.

3.7. SUMMARY

The indentation hardness is not greatly affected by the strain rate when it reaches 0.2 s^{-1} . Both the yield stress and strain hardening exponent of nanosilver sintered joint increase as the sintering pressure increases from 5 MPa to 30 MPa. The plastic stress-strain constitutive equations of pressure sintered nanosilver joint are obtained at room temperature. The maximum indentation depth of nanosilver sintered joint increases with increasing test temperature from 25°C to 200°C, but decreases with increasing sintering pressure from 5 MPa to 30 MPa. Both of the indentation hardness and elastic modulus of nanosilver sintered joint show decrease trend with the increase of temperature from 140°C to 200°C, but increase trend is found when the sintering pressure increases from 5 MPa to 30 MPa. The creep displacement of nanosilver sintered joint increases rapidly at the initial creep stage. The creep displacement of nanosilver sintered joint decreases with the increase of sintering pressure.

REFERENCES

- [1] H. Zhang, Y. Liu, L. Wang, F. Sun, X. Fan, and G. Zhang, *Indentation hardness, plasticity and initial creep properties of nanosilver sintered joint*, Results in Physics **12**, 712 (2018).
- [2] G. Zhang, Z. Li, B. Zhang, and W. A. Halang, *Power electronics converters: Past, present and future*, Renewable and Sustainable Energy Reviews **81**, 2028 (2017).
- [3] J.W. Yoon and B.S. Lee, *Sequential interfacial reactions of Au/In/Au transient liquid phase-bonded joints for power electronics applications*, Thin Solid Films **660**, 618 (2018).
- [4] B. Ji, X. Song, W. Cao, V. Pickert, Y. Hu, J.W. Mackersie, and G. Pierce, *In situ diagnostics and prognostics of solder fatigue in IGBT modules for electric vehicle drives*, IEEE Transactions on Power Electronics **30**, 1535 (2015).

- [5] H. Okumura, *A roadmap for future wide bandgap semiconductor power electronics*, MRS Bulletin **40**, 439 (2015).
- [6] B.S. Lee and J.W. Yoon, *Cu-Sn intermetallic compound joints for high-temperature power electronics applications*, Journal of Electronic Materials **47**, 430 (2018).
- [7] Y. Liu, H. Zhang, L. Wang, X. Fan, G. Zhang, and F. Sun, *Effect of sintering pressure on the porosity and the shear strength of the pressure-assisted silver sintering bonding*, IEEE Transactions on Device and Materials Reliability **18**, 240 (2018).
- [8] F. Yu, J. Cui, Z. Zhou, K. Fang, R.W. Johnson, and M.C. Hamilton, *Reliability of Ag sintering for power semiconductor die attach in high-temperature applications*, IEEE Transactions on Power Electronics **32**, 7083 (2017).
- [9] S. Nishimoto, S.A. Moeini, T. Ohashi, Y. Nagatomo, and P. McCluskey, *Novel silver die-attach technology on silver pre-sintered DBA substrates for high temperature applications*, Microelectronics Reliability **87**, 232 (2018).
- [10] S.Y. Zhao, X. Li, Y.H. Mei, and G.Q. Lu, *Study on high temperature bonding reliability of sintered nano-silver joint on bare copper plate*, Microelectronics Reliability **55**, 2524 (2015).
- [11] S. Fu, Y. Mei, G.Q. Lu, X. Li, G. Chen, and X. Chen, *Pressureless sintering of nanosilver paste at low temperature to join large area ($\geq 100 \text{ mm}^2$) power chips for electronic packaging*, Materials Letters **128**, 42 (2014).
- [12] J. G. Bai and G.Q. Lu, *Thermomechanical reliability of low-temperature sintered silver die attached SiC power device assembly*, IEEE Transactions on Device and Materials Reliability **6**, 436 (2006).
- [13] X. Li, G. Chen, L. Wang, Y.H. Mei, X. Chen, and G.Q. Lu, *Creep properties of low-temperature sintered nano-silver lap shear joints*, Materials Science and Engineering: A **579**, 108 (2013).
- [14] G. Chen, X.H. Sun, P. Nie, Y.H. Mei, G.Q. Lu, and X. Chen, *High-temperature creep behavior of low-temperature-sintered nano-silver paste films*, Journal of Electronic Materials **41**, 782 (2012).
- [15] N.R. Kang, E.J. Gwak, H. Jeon, E. Song, and J.Y. Kim, *Microstructural effect on time-dependent plasticity of nanoporous gold*, International Journal of Plasticity **109**, 108 (2018).
- [16] X. Kong, F. Sun, M. Yang, and Y. Liu, *High temperature creep properties of low-Ag Cu/Sn-Ag-Cu-Bi-Ni/Cu solder joints by nanoindentation method*, Soldering &

- Surface Mount Technology **28**, 167 (2016).
- [17] M. Elbarbary, *Elasto-plastic material properties of lead-free solder by finite element analysis and nanoindentation test*, Master thesis, Lamar University, 2018.
- [18] D. Leslie and A. Dasgupta, and C. Morillo, *Viscoplastic properties of pressure-less sintered silver materials using indentation*, Microelectronics Reliability **74**, 121 (2017).
- [19] S. Kraft and S. Zischler, N. Tham, and A. Schletz, *Properties of a novel silver sintering die attach material for high temperature-high lifetime applications*, in *16th International Conference on Sensors and Measurement Technology (SENSOR 2013)*, 2013, pp. 242-247.
- [20] F. Henaff, S. Azzopardi, E. Woïrgard, T. Youssef, S. Bontemps, and J. Joguet, *Lifetime evaluation of nanoscale silver sintered power modules for automotive application based on experiments and finite-element modeling*, IEEE Transactions on Device and Materials Reliability **15**, 326 (2015).
- [21] W.C. Oliver and G.M. Pharr, *An improved technique for determining hardness and elastic modulus using load and displacement sensing indentation experiments*, Journal of Materials Research **7**, 1564 (1992).
- [22] X. Long, W. Tang, Y. Feng, C. Chang, L.M. Keer, and Y. Yao, *Strain rate sensitivity of sintered silver nanoparticles using rate-jump indentation*, International Journal of Mechanical Sciences **140**, 60 (2018).
- [23] G. Xiao, G. Yuan, C. Jia, X. Yang, Z. Li, and X. Shu, *Strain rate sensitivity of Sn-3.0 Ag-0.5 Cu solder investigated by nanoindentation*, Materials Science and Engineering: A **613**, 336 (2014).
- [24] X. Hou and N. Jennett, *A method to separate and quantify the effects of indentation size, residual stress and plastic damage when mapping properties using instrumented indentation*, Journal of Physics D: Applied Physics **50**, 455304 (2017).
- [25] J. Luo and J. Lin, *A study on the determination of plastic properties of metals by instrumented indentation using two sharp indenters*, International Journal of Solids & Structures **44**, 5803 (2007).
- [26] M. Dao, N. Chollacoop, K. Vliet, T. Venkatesh, and S. Suresh, *Computational modeling of the forward and reverse problems in instrumented sharp indentation*, Acta Materialia **49**, 3899 (2001).

- [27] M. Barbary, L. Chen, Y. Liu, F. Qin, and X. Fan, *On the uniqueness and sensitivity of nanoindentation testing for determining elastic and plastic material properties of electroplating copper filled in through-silicon-via (TSV)*, in *IEEE 68th Electronic Components and Technology Conference (ECTC 2018)*, 2018, pp. 1023-1029.
- [28] P. Sanders, C. Youngdahl, and J. Weertman, *The strength of nanocrystalline metals with and without flaws*, *Materials Science and Engineering: A* **234**, 77 (1997).
- [29] A. Giannakopoulos and S. Suresh, *Determination of elastoplastic properties by instrumented sharp indentation*, *Scripta Materialia* **40**, 1191 (1999).
- [30] E. George and I. Baker, *Thermal vacancies and the yield anomaly of FeAl*, *Intermetallics* **6**, 759 (1998).
- [31] D. Mu, H. Huang, S.D. McDonald, and K. Nogita, *Creep and mechanical properties of Cu_6Sn_5 and $(Cu, Ni)_6Sn_5$ at elevated temperatures*, *Journal of Electronic Materials* **42**, 304 (2013).
- [32] K. Kese, P. Olsson, A.M. A. Holston, and E. Broitman, *High temperature nanoindentation hardness and Young's modulus measurement in a neutron-irradiated fuel cladding material*, *Journal of Nuclear Materials* **487**, 113 (2017).
- [33] R.M. Mohamed, M.K. Mishra, L.M.A. Harbi, M.S.A. Ghamdi, A.M. Asiri, C.M. Reddy, and U. Ramamurty, *Temperature dependence of mechanical properties in molecular crystals*, *Crystal Growth & Design* **15**, 2474 (2015).
- [34] H. Ma and J.C. Suhling, *A review of mechanical properties of lead-free solders for electronic packaging*, *Journal of Materials Science* **44**, 1141 (2009).

4

MECHANICAL PROPERTIES OF NANOSILVER DOUBLE SIDE SINTERED PACKAGE

Modern power electronics has the increased demands in current density and high temperature reliability. However, these performance factors are limited due to the die attach materials used to affix power dies to the electric circuitry. Although several die attach materials and methods exist, nanosilver sintering technology has received much attention in attaching power dies due to its superior high temperature reliability. This chapter investigates the sintering properties of nanosilver film in double side sintered power packages. X-ray diffraction (XRD) results reveal that the size of nanosilver particles increases after pressure-free sintering. Comparing with the pressure-free sintered nanosilver particles, the 5 MPa sintered particles show a higher density. When increasing sintering pressure from 5 MPa to 30 MPa, the shear strength of the sintered package increases from 8.7 MPa to 86.3 MPa. When sintering at pressures below 20 MPa, the fracture areas are mainly located between the sintered Ag layer and the surface metallization layer on the fast recovery diode (FRD) die. The fracture occurs through the FRD die and the metallization layer on the bottom Mo substrate when sintering at 30 MPa.

Parts of this chapter have been published in [IEEE Transactions on Components, Packaging and Manufacturing Technology](#) **9**, 963 (2019) [1].

4.1. INTRODUCTION

The rapid development of wide-band gap semiconductors have facilitated power electronics becoming key components in hybrid electric vehicles, traction, wind turbine and high-voltage power transmission systems due to their combined advantages of fast switch speed and low power consumption [2-4]. Despite these promising attributes, the development trends of power electronics require increased current carrying capacity and higher operating temperatures. This proposes a challenge to power electronics' packaging components, particularly die attachment materials. The die attach layer plays an important role in power electronics. Yu *et al.* [5] indicated that the die attach layers are responsible for mechanical connection of microelectronics to the substrate, thermal dissipation of processing units, and electric conduction. Therefore, the effectiveness of the die attach layer significantly contributes to the overall performance of the entire package. Moreover, die attach materials typically limit the operating temperature and power density of the device. In the work of Navarro *et al.* [6], the silicon-based packages, for example, have an operating temperature of only about 175°C and a power density of 200 W/cm². These physical limitations as well as the lifetime concerns of lead-based solders have led to alternative die attach technologies.

Currently, several advanced die attach materials and methods of attachment exist that increase electrical/temperature performance of power electronic devices, but the manufacturing and service processes often reduce mechanical reliability and manufacturing efficiency. For instance, Gold-tin eutectic solder alloy has been widely used as soldering material in attaching power dies due to its favorable mechanical properties and capability of fluxless soldering [7, 8]. Huang *et al.* [9] implied that the AuSn eutectic layer has been proven to provide good electrical and thermal conductivity, and reliable high temperature interconnection for power electronics. However, Wang *et al.* [10] proved that the coarsening of microstructure in the service process decreased the reliability of AuSn solder joint. In addition, Arabi *et al.* [11] suggested that the voids can cause localized stress and cracks under thermal cycles as well as thermal stress from its high processing temperature which limit the wide application of AuSn solder alloy. Transient liquid phase (TLP) bonding technology has been developed as a die attaching process in response to increased concerns over lead-based attachments. As described by Khazaka *et al.* [12], a metallic interlayer is usually used in the TLP process, such as Sn or In. This interlayer reacts under low pressure with a substrate that has a higher melting point, such as Cu, Ag, Ni, Au [13-16]. The formed die attach layer consists of full intermetallic compounds (IMCs) and its re-melting temperature is much higher than the melting point of the corresponding solder material. But Shao *et al.* [17] found that the TLP process is quite time consuming because of the diffusion dominated reaction

between the interlayer and substrate, and IMCs are brittle, causing performance issues.

Recently, nanosilver sintering technology has shown great potential in attaching power dies while potentially maintaining favorable physical properties [18]. The nanosilver particles are usually mixed with dispersant, binder and thinner to form nanosilver paste, which can be further screen printed or dispensed on the substrate. The nanosilver paste can be sintered at low temperatures around 250°C to form a bonding, and then serve at relatively high temperatures. Bai *et al.* [19] reported that the electrical conductivity and thermal conductivity of pressure-free sintered Ag layer can reach as high as $2.6 \times 10^7 / (\Omega \cdot m)$ and 240 W/(m·K), respectively. However, Qi *et al.* [20] indicated that low shear strength is generated in sintered Ag layer without the assistance of pressure, especially when die sizes are larger than 9 mm². It was reported by Ogura *et al.* [21] that the fracture surface of pressure-free sintered nanosilver layer exhibited uneven morphology with randomly distributed weak spots on the bonding area. In addition, as demonstrated by Knoerr and Schletz [22], the density of sintered Ag layer can be improved from 58% to 90% when the sintering pressure increased from 0 MPa to 30 MPa. The increased density will also be beneficial for the improvement of electrical and thermal conductivity of sintered Ag layer. Zhao *et al.* [23] have already applied pressure assisted sintering in industrial production, and the thermal shock test results revealed that the better reliability of pressure sintered power module was obtained when comparing with soldered power module. Therefore, the sintering pressure is quite necessary to ensure the long term high temperature reliability of power package, especially for bonding package with large dies.

According to our previous test results [24], the two Molybdenum (Mo) substrates, coated with Ag/Cu/Ni(Mo), were successfully bonded by the sintering of nanosilver film. In this chapter, a real power module that involves with power dies is studied. We are trying to apply this result in our further test to verify the feasibility in bonding real products, which involves the power dies. This chapter investigates the effect of sintering pressure on nanosilver films and double-sided nanosilver sintered power packages. Particle densification of the nanosilver films during fabrication can have significant effects on the performance of the package, and this effect is examined by comparing sintered, not sintered, and pressure-assisted nanosilver films. The thermal behavior of nanosilver film is studied by differential scanning calorimetry (DSC) test. The morphology and phase composition of the pure nanosilver film before and after pressure-free sintering are investigated by scanning electron microscopy (SEM) and X-ray diffraction (XRD), respectively. The morphologies of pressure-free and pressure-assisted sintered nanosilver film are then compared by SEM. The mechanical performance of a power package often limits its reliability. The mechanical performance of pressure

sintered power packages in this research are determined by shear tests for a variety of sintering pressures. The fracture morphologies achieved by the shear tests are then further analyzed by SEM to demonstrate the effect of sintering pressure on bonding strength. Energy dispersive spectroscopy (EDS) is conducted in conjunction with SEM to determine material transfers after fracture.

4.2. METHODOLOGY

The nanosilver film used was the commercial sintering material from Alpha Assembly. In order to characterize the structure and phase composition of sintered nanosilver particles, two pure nanosilver films were sintered at 250°C for 3 min. One film was pressure-free sintered, and another was sintered with a pressure of 5 MPa. SEM was used to investigate the morphology of nanosilver of these two samples. X-ray Diffraction (XRD) was conducted to investigate the crystal structures of the pressure-free nanosilver particles. All films in this analysis and this research had a thickness of 65 μm . Besides, the DSC test was performed for nanosilver film in N_2 atmosphere, and the heating range and heating rate was set as 130°C to 260°C and 10°C/min, respectively.

Four power packages were produced for the shear tests in this study. Each power package was fabricated with novel equipment, Sinterstar Innovate-F-XL, which could precisely and uniformly control the applied pressure at high temperatures through the real time feedback system embedded in the equipment, as shown in Figure 4.1. There are three main steps in fabricating these power packages as seen in Figure 4.1. First, two Molybdenum (Mo) substrates were laminated with nanosilver film on one side. The Mo substrate was coated with several layers on the top and bottom surfaces: Ag/Cu/Ni/(Mo substrate). The larger Mo substrate was to be the bottom Mo substrate with dimension of 13.6×13.6×2.0 mm³, and the smaller was to be the top Mo substrate with dimension of 9.4×9.4×1.2 mm³. This process was achieved at 130°C with the pressure of 5 MPa for 2 min. Second, the FRD die (13.53×13.53×0.41 mm³) coated with Ag on the top surfaces of up and down sides was placed on the laminated side of the bottom Mo substrate, and then sintered at 250°C for 3 min. In order to investigate the effects of sintering pressure on the bonding quality of the sintered Ag layer, four samples were created, each at different applied pressures of 5, 10, 20, 30 MPa during the sintering process in this step. Then, the laminated side of the top Mo substrate was placed on the top of the sintered bottom Mo substrate. The assembled package was then sintered at 250°C for 3 min and the same sintering pressure was used as last step. The entire process was achieved in air. The schematic diagram of cross section of double side sintered power package is shown in Figure 4.1, and the thickness of each layer is also marked.

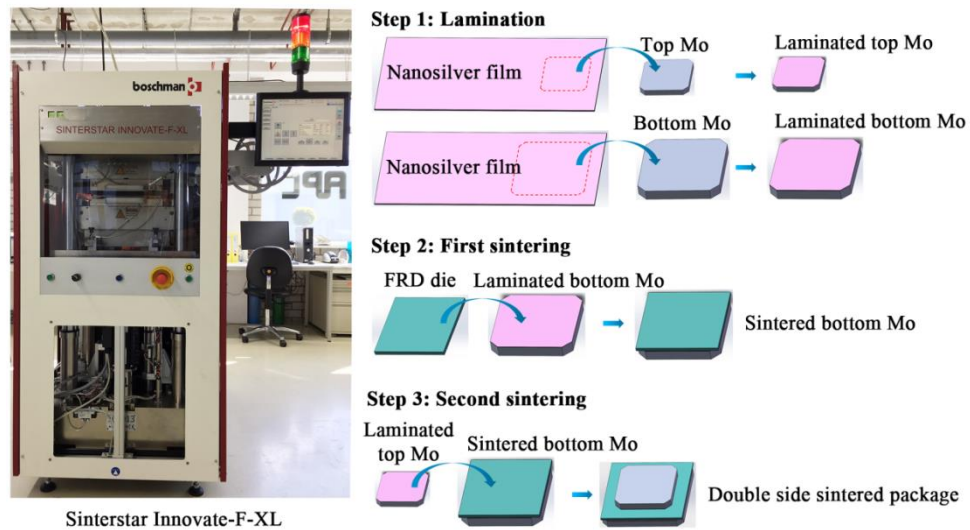


Figure 4.1: Sintering equipment and schematic diagram of fabrication process (not drawn to scale)

To determine the mechanical properties of sintered Ag layer, a shear test was performed on the Instron 5569 electromechanical test machine. The test settings were based on the standard of MIL-STD-883E, Method 2019.5. The sintered package was first secured in a special designed rigid frame and a constant test speed was set as constant of 0.3 mm/min, as shown in Figure 4.2. The mechanical properties of sintered package were measured in displacement control mode. The fracture surface morphology of sheared sample was examined by SEM and EDS.

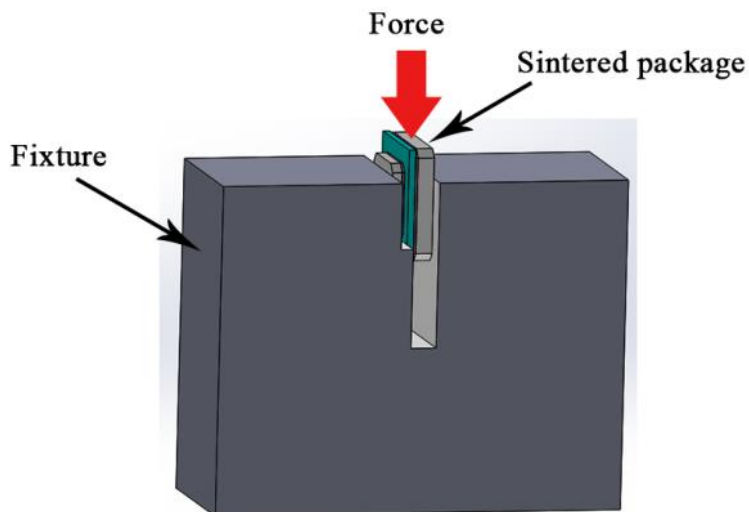


Figure 4.2: Schematic diagram of the shear test

4.3. CHARACTERIZATION OF SINTERED NANOSILVER FILM

4.3.1. PRESSURE-FREE SINTERED NANOSILVER FILM

The thermal behavior of nanosilver film is first investigated by DSC test. Figure 4.3 shows the DSC heat curve of nanosilver film within the temperature range of 130-260°C. As indicated in the figure, one exothermic peak at approximately 220-240°C is obviously observed during heating process. When the sintering temperature increases to 220°C, the organics inside the nanosilver film decompose gradually. It is suggested that the coalescence of silver nanoparticles starts at this temperature. The decomposition of organics ends around 240°C. Therefore, it is reasonable to conclude that the sintering temperature of nanosilver film should be higher than 240°C in order to get the good bonding between silver nanoparticles. In this research, the temperature of 250°C is selected for the sintering tests.

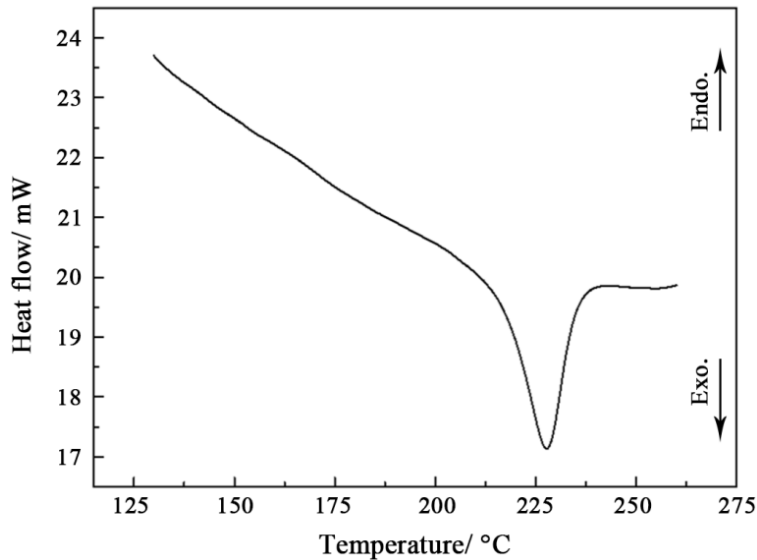


Figure 4.3: DSC heat curve of nanosilver film

An initial SEM investigation was conducted to examine morphologies of pure nanosilver film before and after sintering, as shown in Figure 4.4(a) and 4.4(b) respectively. The nanosilver particles are coated with a nearly transparent layer on the surface, which can prohibit the aggregation between particles, as shown in Figure 4.4 (a). The nanosilver particles have an average diameter around 200 nm. The close contact of nanosilver particles is likely to result from the compression during the film fabrication process. During sintering, the organic shells start to decompose and allow adjacent nanosilver particles to combine with each other. This combining of particles is seen upon

comparing Figure 4.4(a) and 4.4(b). Li *et al.* [25] suggested that surface diffusion is the primary sintering mechanism at the beginning of the sintering process due to its lowest activation energy, and then followed by grain boundary diffusion and lattice diffusion as temperature increases. After pressure-free sintering at 250°C for 3 min, sintering necks are formed between particles, which indicate bonding of the nanosilver layer, as shown in Figure 4.4(b).

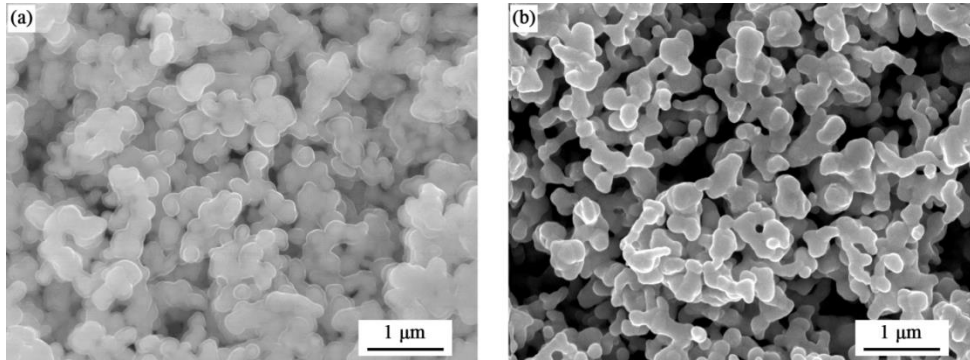


Figure 4.4: SEM images of nanosilver film, (a) original; (b) pressure-free sintered at 250°C for 3 min

Crystal structures of nanosilver particles before and after pressure-free sintering at 250°C for 3 min were studied with XRD, and the results are shown in Figure 4.5. According to the test results, five obvious peaks appear in the original nanosilver film, and the corresponding crystal plane index is (111), (200), (220), (311) and (222), respectively. Because of the existence of a large number of oriented small crystal particles in the irradiated area, the nanosilver particles exhibit a polycrystalline structure.

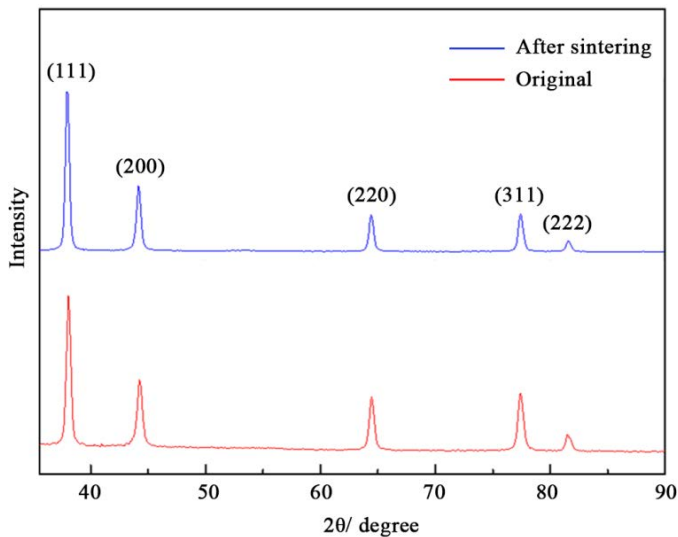


Figure 4.5: XRD spectra of nanosilver particles before and after sintering

The full width at half maximum (FWHM) of the nanosilver particles are listed in Table 4.1 for the crystal planes found in Figure 4.5. Comparing the FWHM of nanosilver particles before and after sintering, the peaks of sintered particles show slightly narrowed width due to the increased particle size. Similar results have been obtained by sintering different types of silver particles [26, 27]. In addition, there is no oxidation peak observed after sintering in air. This result indicates that the nanosilver particles are not greatly oxidized and the formed sintered joint is mainly composed of silver particles, which also implies good bonding between nanosilver particles.

Table 4.1: FWHM of nanosilver particles

Nanosilver particles	2θ / degree (111)	2θ / degree (200)	2θ / degree (220)	2θ / degree (311)	2θ / degree (222)
Original	0.46	0.54	0.52	0.56	0.60
After sintering	0.41	0.46	0.47	0.50	0.50

4.3.2. COMPARISON OF SINTERED SILVER NANOPARTICLES

An SEM study was conducted to investigate the effect of applied pressure during sintering on the structure of nanosilver particles. The results in Figure 4.6(a) and 4.6(b) show the pressure-free and 5 MPa sintered layers respectively. As seen in Figure 4.6(a), the overall morphology of pressure-free sintered nanosilver particles shows an irregular structure. Some of the particles only combine with the nearest ones, which will result in the discontinuous matrix. However, the dense and well-structured sintered Ag layer seen in Figure 4.6(b) is achieved with the help of sintering pressure. Most of the particles have formed sintering necks with particles around them. Comparing the micrographs also illustrates that the pressure-free sintered structure is more porous. The porosity of pressure-free and 5 MPa sintered nanosilver particles were measured using Image-J software and the corresponding result is 16.26% and 5.38%, respectively. These results and the results in the previous section confirm both sintering and pressure during nanosilver sintering may enhance the performance of the power package.

4.4. EFFECTS OF SINTERING PRESSURE ON THE SHEAR STRENGTH

During sintering, the formation of necks between particles can be enhanced with the help of applied pressure and finally result in the high mechanical properties. The shear strength of sintered package reveals an increasing trend with the increase of sintering pressure, as shown in Figure 4.7. The average shear strength of 5 MPa sintered package is

8.7 MPa. When sintering pressure increases to 10 MPa, the sintered package has the average shear strength of 24.7 MPa and the increase rate is 64.71%. The maximum increase rate of 65.83% is achieved when pressure increases from 10 MPa to 20 MPa. The highest shear strength of 86.3 MPa is obtained at a pressure of 30 MPa. This gives empirical evidence that pressure-assisted sintering will increase the mechanical performance of the package, but the rate of increase is most effective between 10 and 20 MPa.

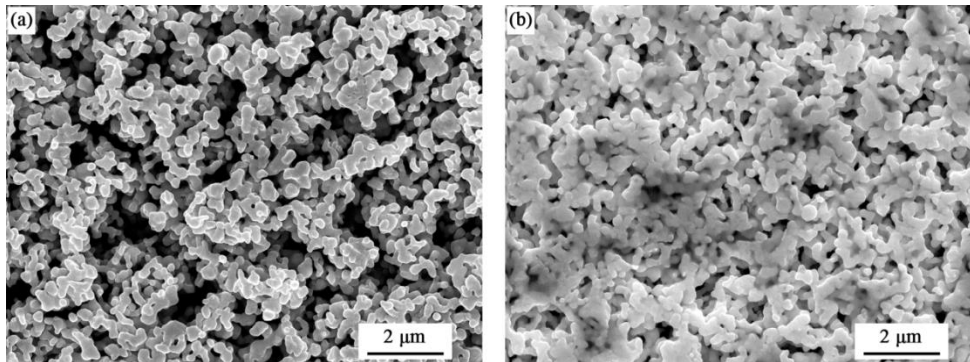


Figure 4.6: Comparison of sintered nanosilver particles at 250°C for 3 min, (a) 0 MPa; (b) 5 MPa

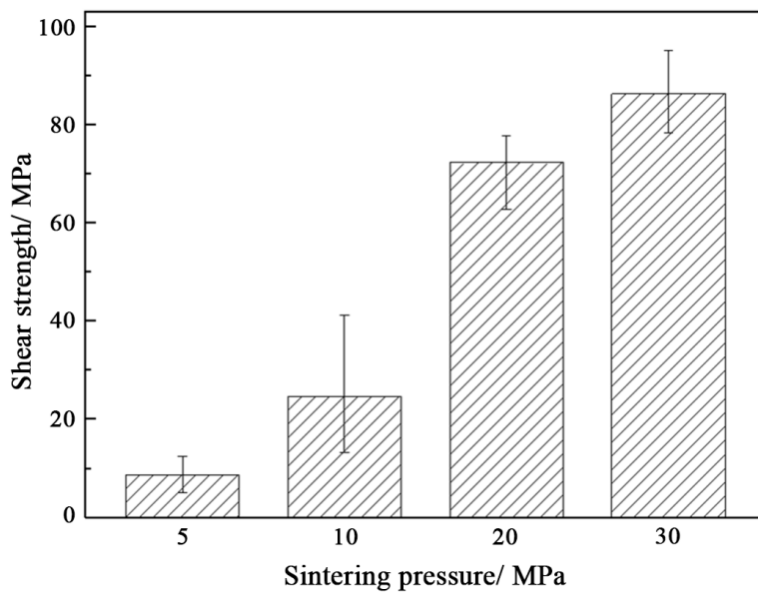


Figure 4.7: Relationship between sintering pressure and shear strength

4.5. EFFECTS OF SINTERING PRESSURE ON THE FRACTURE MORPHOLOGY

Shear tests were conducted on the power packages, and the fracture morphologies of a sintered package under 5 MPa are shown in Figure 4.8. According to the optical image in Figure 4.8(a), the fracture area is mainly located at the interface between the sintered Ag layer and the surface metallization layer on FRD die. The top Mo substrate and the whole sintered Ag layer are peeled off the package, which indicates weak bonding between sintered nanosilver particles and die surface metallization. The fracture surface of sintered Ag layer is quite smooth, as shown in the partial magnified image in Figure 4.8(b) and 4.8(c). The detailed morphology is shown in Figure 4.8(d), and there are only sintered nanosilver particles found in this location, which can be identified by energy-dispersive X-ray spectroscopy (EDS) in Figure 4.8(e). In addition, the fracture surface in Figure 4.8(d) is not flat and pores with various sizes are formed between particles.

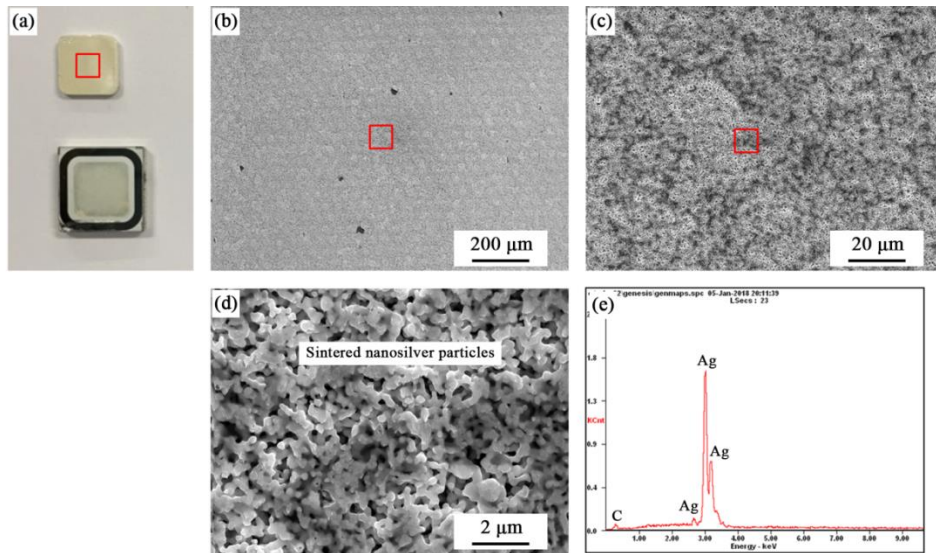


Figure 4.8: Fracture morphology of sintered package under 5 MPa, (a) optical image of fracture surface; (b), (c) and (d) are the gradually partial magnified image of (a); (e) EDS pattern of the fracture surface in (d)

Figure 4.9 displays the fracture morphology of 10 MPa sintered package. Similar to the 5 MPa sintered package, the fracture area in this package is also located at the interface between the sintered Ag layer and the surface metallization layer on FRD die, as shown in Figure 4.9(a). The magnified fracture morphologies are quite flat and smooth, as seen in Figure 4.9(b) and 4.9(c), which indicates the uniform diffusion bonding of nanosilver particles under 10 MPa pressure. Based on the magnified image in Figure 4.9(d) and the EDS analysis in Figure 4.9(e), the fracture surface mainly consists of

sintered nanosilver particles. The sintered nanosilver particles have a lower porosity when comparing with the 5 MPa sintered ones in Figure 4.9(d).

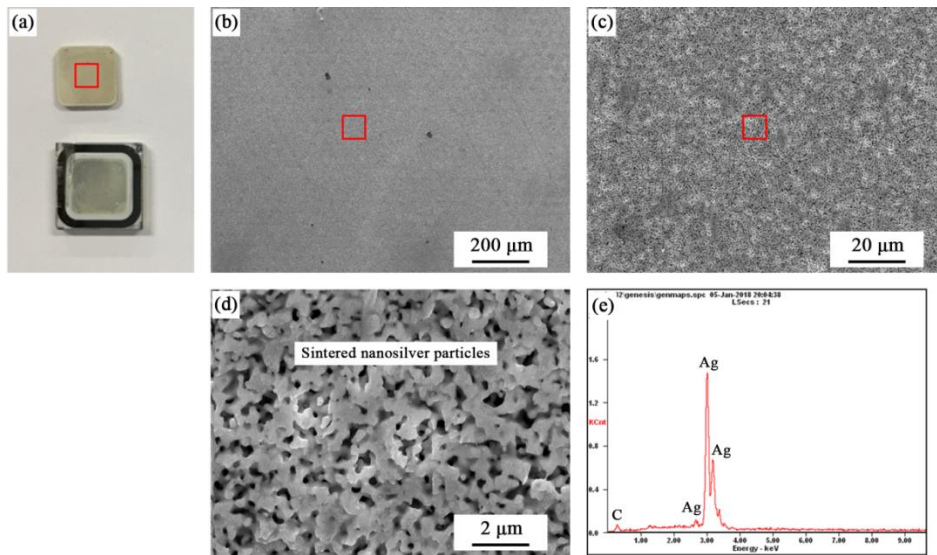


Figure 4.9: Fracture morphology of sintered package under 10 MPa, (a) optical image of fracture surface; (b), (c) and (d) are the gradually partial magnified image of (a); (e) EDS pattern of the fracture surface

However, as the sintering pressure increases to 20 MPa, the fracture occurs partially on the FRD die and partially on the sintered Ag layer, as shown in Figure 4.10(a). The sintering pressure of 20 MPa has an obvious effect of strengthening the bonding between sintered Ag layer and metallization layer on FRD die. As seen in Figure 4.10(b) and its magnified image in Figure 4.10(c), the fracture surface is not flat and there are many depressions on it. More details can be obtained from Figure 4.10(d), the fracture area is composed of Ag coating on FRD die and the sintered Ag particles. The element composition is proven by EDS results in Figure 4.10(e), showing no significant material transfer other than the sintered silver.

At 30 MPa, fracture occurs through the FRD die and the metallization layer on bottom Mo substrate as shown in Figure 4.11(a). The fracture surface of 30 MPa sintered package is quite rough, which is different from other packages that are sintered at pressures lower than 30 MPa, as shown in Figure 4.11(b). The further magnified image is shown in Figure 4.11(c), and the fracture surface is partially lifted up and partially ripped. More details are depicted in Figure 4.11(d), and no nanosilver particles are found on the surface. According to the EDS analysis in Figure 4.11(e), the fracture area is located at the metallization layer on the Mo substrate, which contains Ag, Cu and Ni elements.

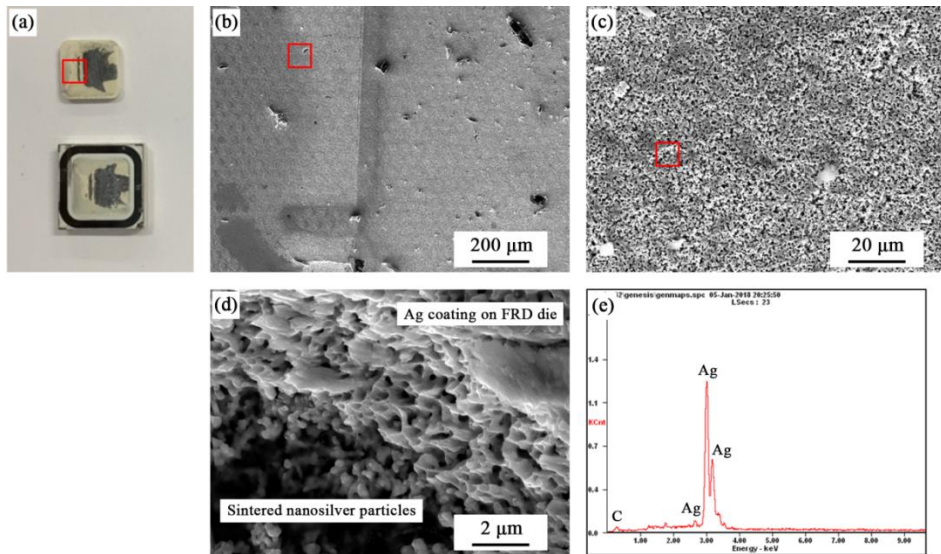


Figure 4.10: Fracture morphology of sintered package under 20 MPa, (a) optical image of fracture surface; (b), (c) and (d) are the gradually partial magnified image of (a); (e) EDS pattern of the fracture surface

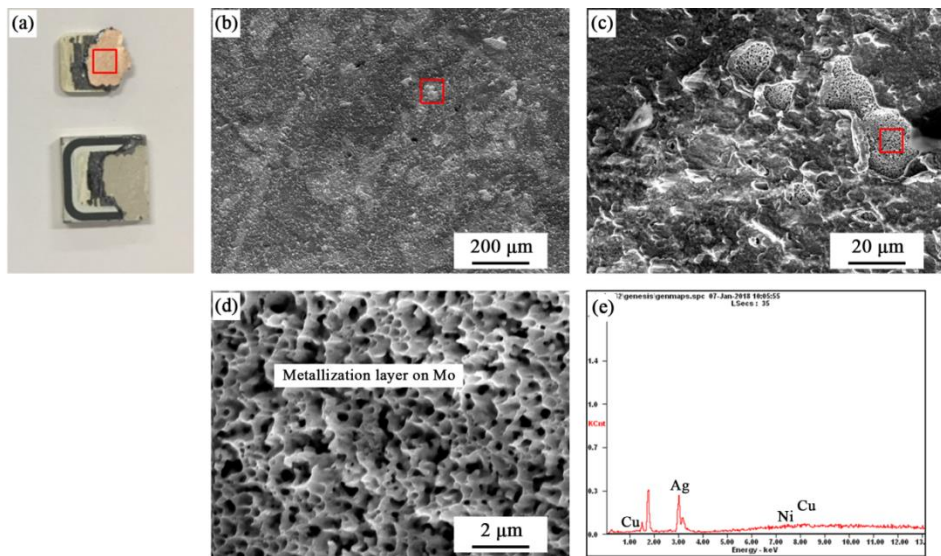


Figure 4.11: Fracture morphology of sintered package under 30 MPa, (a) optical image of fracture surface; (b), (c) and (d) are the gradually partial magnified image of (a); (e) EDS pattern of the fracture surface

Combining the results of Figure 4.7 and Figures 4.8-4.11, there is strong evidence that increasing the applied pressure when sintering increases the shear and bonding strength of the package, but only at pressures below 30 MPa. The change of fracture area may due to the enhanced bonding strength of metallization layer under high sintering

pressures. Dudek *et al.* [28] also proved that the bonding quality of metallization layer can be improved by the increased sintering pressure from 5 MPa to 20 MPa, which resulted in the change of fracture area from the die attach layer to the die. Based on the results above, it can be concluded that a sintering pressure higher than 5 MPa is quite useful to ensure the high bonding quality of sintered package. However, the sintering pressure beyond 20 MPa may not be optimal for manufacturing due to the limited increase rate in shear strength when increasing the sintering pressure from 20 MPa to 30 MPa.

4.6. SUMMARY

According to the crystal structure analysis before and after pressure-free sintering, the peaks of sintered particles exhibit slight narrowed width due to the increased particle size. The overall morphology of pressure-free sintered nanosilver particles shows irregular and discontinuous matrix. However, a dense and well-structured sintered layer is obtained with the help of 5 MPa sintering pressure. This result indicates that the application of sintering pressure during nanosilver sintering may enhance the performance of the power package. The shear strength of sintered package increases with pressure increasing from 5 MPa to 30 MPa. The highest increase rate is obtained when sintering pressure increases from 10 to 20 MPa. The fracture areas are mainly locate between the sintered Ag layer and the surface metallization layer on FRD die at sintering pressures lower than 20 MPa, and finally change to the FRD die and even the metallization layer on bottom of Mo at 30 MPa. However, the shear tests indicate increasing the sintering pressure beyond 20 MPa may not be optimal for manufacturing.

REFERENCES

- [1] H. Zhang, Y. Liu, L. Wang, F. Sun, J. Fan, M.D. Placette, X. Fan, and G. Zhang, *Effects of sintering pressure on the densification and mechanical properties of nanosilver double side sintered power module*, IEEE Transactions on Components, Packaging and Manufacturing Technology **9**, 963 (2019).
- [2] X. She, A.Q. Huang, Ó. Lucía, and B. Ozpineci, *Review of silicon carbide power devices and their applications*, IEEE Transactions on Industrial Electronics **64**, 8193 (2017).
- [3] J. Li, C.M. Johnson, C. Buttay, W. Sabbah, and S. Azzopardi, *Bonding strength of multiple SiC die attachment prepared by sintering of Ag nanoparticles*, Journal of Materials Processing Technology **215**, 299 (2015).
- [4] S.A. Paknejad and S.H. Mannan, *Review of silver nanoparticle based die attach*

- materials for high power/temperature applications*, Microelectronics Reliability **70**, 1 (2017).
- [5] F. Yu, J. Cui, Z. Zhou, K. Fang, R.W. Johnson, and M.C. Hamilton, *Reliability of Ag sintering for power semiconductor die attach in high-temperature applications*, IEEE Transactions on Power Electronics **32**, 7083 (2017).
- [6] L.A. Navarro, X. Perpina, P. Godignon, J. Montserrat, V. Banu, M. Vellvehi, and X. Jorda, *Thermomechanical assessment of die-attach materials for wide bandgap semiconductor devices and harsh environment applications*, IEEE Transactions on Power Electronics **29**, 2261 (2014).
- [7] J.W. Yoon, H.S. Chun, and S.B. Jung, *Reliability evaluation of Au-20Sn flip chip solder bump fabricated by sequential electroplating method with Sn and Au*, Materials Science and Engineering: A **473**, 119 (2008).
- [8] H. Zhang, J. Fan, J. Zhang, C. Qian, X. Fan, F. Sun, and G. Zhang, *Reliability optimization of gold-tin eutectic die attach layer in HEMT package*, in *13th China International Forum on Solid State Lighting (SSLChina 2016)*, 2016, pp. 52-56.
- [9] Y. Huang, W. Liu, Y. Ma, Y. Wang, and S. Tang, *Effects of cooling rate and magnetic field on solidification characteristics of Au80Sn20 eutectic solder*, Journal of Materials Science: Materials in Electronics **29**, 436 (2018).
- [10] Y. Wang, W. Liu, Y. Ma, Y. Huang, Y. Tang, F. Cheng, and Q. Yu, *Indentation size effect and micromechanics characterization of intermetallic compounds in the Au-Sn system*, Materials Science and Engineering: A **610**, 161 (2014).
- [11] F. Arabi, L. Theolier, D. Martineau, J.Y. Deletage, M. Medina, and E. Woïrgard, *Power electronic assemblies: Thermo-mechanical degradations of gold-tin solder for attaching devices*, Microelectronics Reliability **64**, 409 (2016).
- [12] R. Khazaka, L. Mendizabal, D. Henry, and R. Hanna, *Survey of high-temperature reliability of power electronics packaging components*, IEEE Transactions on Power Electronics **30**, 2456 (2015).
- [13] Z. Li, J. Liu, H. Zhao, X. Song, Y. Zhao, H. Niu, H. Tian, H. Dong, and J. Feng, *Microstructure evolution, grain morphology variation and mechanical property change of Cu-Sn intermetallic joints subjected to high-temperature aging*, Materials Characterization **135**, 238 (2018).
- [14] H. Shao, A. Wu, Y. Bao, Y. Zhao, and G. Zou, *Microstructure characterization and mechanical behavior for Ag₃Sn joint produced by foil-based TLP bonding in air*

- atmosphere*, Materials Science and Engineering: A **680**, 221 (2017).
- [15] S.W. Yoon, M.D. Glover, and K. Shiozaki, *Nickel–tin transient liquid phase bonding toward high-temperature operational power electronics in electrified vehicles*, IEEE Transactions on Power Electronics **28**, 2448 (2013).
- [16] T.A. Tollefsen, A. Larsson, O.M. Løvvik, and K.E. Aasmundtveit, *High temperature interconnect and die attach technology: Au–Sn SLID bonding*, IEEE Transactions on Components, Packaging and Manufacturing Technology **3**, 904 (2013).
- [17] H. Shao, A. Wu, Y. Bao, Y. Zhao, L. Liu, and G. Zou, *Rapid Ag/Sn/Ag transient liquid phase bonding for high-temperature power devices packaging by the assistance of ultrasound*, Ultrasonics Sonochemistry **37**, 561 (2017).
- [18] H. Zhang, Y. Liu, L. Wang, J. Fan, X. Fan, F. Sun, and G. Zhang, *A new hermetic sealing method for ceramic package using nanosilver sintering technology*, Microelectronics Reliability **81**, 143 (2018).
- [19] J.G. Bai, Z.Z. Zhang, J.N. Calata, and G.Q. Lu, *Low-temperature sintered nanoscale silver as a novel semiconductor device-metallized substrate interconnect material*, IEEE Transactions on components and packaging technologies **29**, 589 (2006).
- [20] K. Qi, X. Chen, and G.Q. Lu, *Effect of interconnection area on shear strength of sintered joint with nano-silver paste*, Soldering & Surface Mount Technology **20**, 8 (2008).
- [21] H. Ogura, M. Maruyama, R. Matsubayashi, T. Ogawa, S. Nakamura, T. Komatsu, H. Nagasawa, A. Ichimura, and S. Isoda, *Carboxylate-passivated silver nanoparticles and their application to sintered interconnection: A replacement for high temperature lead-rich solders*, Journal of Electronic Materials **39**, 1233 (2010).
- [22] M. Knoerr and A. Schletz, *Power semiconductor joining through sintering of silver nanoparticles: Evaluation of influence of parameters time, temperature and pressure on density, strength and reliability*, in *6th International Conference on Integrated Power Electronics Systems (CIPS 2010)*, 2010, pp. 10.3.
- [23] Y. Zhao, P. Mumby-Croft, S. Jones, A. Dai, Z. Dou, Y. Wang, and F. Qin, *Silver sintering die attach process for IGBT power module production*, in *IEEE Applied Power Electronics Conference and Exposition (APEC 2017)*, 2017, pp. 3091-3094.
- [24] Y. Liu, H. Zhang, L. Wang, X. Fan, G. Zhang, and F. Sun, *Effect of sintering pressure on the porosity and the shear strength of the pressure-assisted silver sintering bonding*, IEEE Transactions on Device and Materials Reliability **18**, 240 (2018).

- [25] J. Li, X. Li, L. Wang, Y.H. Mei, and G.Q. Lu, *A novel multiscale silver paste for die bonding on bare copper by low-temperature pressure-free sintering in air*, *Materials & Design* **140**, 64 (2017).
- [26] R. Zhang, K.S. Moon, W. Lin, and C. Wong, *Preparation of highly conductive polymer nanocomposites by low temperature sintering of silver nanoparticles*, *Journal of Materials Chemistry* **20**, 2018 (2010).
- [27] J.H. Jeong and T.S. Cho, *Sintering behaviors of Ag nanopowders with different particle sizes: A real-time synchrotron X-ray scattering study*, *Journal of Nanoscience and Nanotechnology* **17**, 7799 (2017).
- [28] R. Dudek, R. Doring, P. Sommer, B. Seiler, K. Kreyssig, H. Walter, M. Becker, and M. Gunther, *Combined experimental-and FE-studies on sinter-Ag behaviour and effects on IGBT-module reliability*, in *15th International Conference on Thermal, Mechanical and Multi-Physics Simulation and Experiments in Microelectronics and Microsystems (EuroSimE 2014)*, 2014, pp. 1-9.
- [29] P. Peng, A. Hu, A.P. Gerlich, G. Zou, L. Liu, and Y.N. Zhou, *Joining of silver nanomaterials at low temperatures: processes, properties, and applications*, *ACS Appl Mater Interfaces* **7**, 12597 (2015).
- [30] J. Mackenzie and R. Shuttleworth, *A phenomenological theory of sintering*, *Proceedings of the Physical Society. Section B* **62**, 833 (1949).

5

STRESS ANALYSIS OF NANOSILVER DOUBLE SIDE SINTERED PACKAGE USING FEA METHOD

Crack formation and stress distribution on dies are the key issues for the pressure-assisted sintering bonding of power modules. The aim of this chapter is to build the relationship between the stress distributions, the sintering sequences, and the sintering pressures during the sintering processes. This chapter investigates the stress distributions of the double side sintered power modules under different sintering pressures. Based on the results of experiments and finite element analysis (FEA), the best sintering sequence design is provided under various sintering pressures. Three sintering sequences, denoted as S(a), S(b) and S(c), have been designed for the double side assembly of power module in this chapter. Experiments and finite element analysis are conducted to investigate the crack formation and stress distribution. The sintering sequence has significant effects on the crack generation in the chips during the sintering process under 30 MPa pressure. The simulation results reveal that the module sintered by S(a) showed lower chip stress than those by the other two sintering sequences under 30 MPa. In contrast, the chip stress is the highest when the sintering sequence follows S(b). The simulation results explain the crack generation and prolongation in the experiments. S(a) is recommended as the best sintering sequence because of the lowest chip stress and highest yield rate.

5.1. INTRODUCTION

High-voltage power modules have achieved significant progress to meet the increasing demands and applications of power chips, such as insulated gate bipolar transistor (IGBT) and fast recovery diode (FRD) in automotive, energy transfer, and aerospace industries in the near years [2-4]. The trends to develop power chips with high voltage and high power density have posed new challenges for the assembly technology of power modules due to reliability concern [5, 6]. As one of the critical assembly processes, the die attach technology is a governing restriction to improve the reliability of the power modules.

Soldering and silver sintering are typical die attach methods for power modules [7, 8]. Soldering achieves wide applications in the assembly of low power modules because of its advantages such as high-efficiency, low-cost, and self-alignment [9-12]. However, there are three major challenges which restrict the application of soldering in the assembly of high power modules. The first one is the low creep resistance of the solder joints in high temperature environment [13]. The high service temperature of high power modules is a threat to the reliability of the solder joints. The second major challenge is the evolution of the brittle interfacial intermetallic compounds (IMCs) in the solder joints [14, 15], which is considered as the leading factor for the generation and prolongation of interfacial crack in the solder joints. Besides, the electro-migration in the solder joints may be intensified in high power applications [16]. In contrast, the silver-sintered connections show better thermal stability and higher reliability than the solder joints [17, 18]. Due to reliability concern, sintering is considered as a promising method for the assembly of high power modules [19, 20].

Compared with silver bulks, silver-sintered layer shows some worse performances, such as mechanical properties, thermal conductivity and electrical conductivity. The biggest challenges for silver sintering are to decrease the porosity and to improve the comprehensive performances of the sintered layers. Youssef *et al.* demonstrated that the lifetime of nanosilver sintered power module is affected by the porosity ratio inside the sintered layer [21]. Herboth *et al.* [22] identified that the decrease of porosity in the sintered layer greatly improved the lifetime of sintered package during thermal shock test. The performances of the sintered layers can be improved by optimizing sintering parameters, sintering environment and composition of the sinter paste [23]. Zhang *et al.* [24] investigated the bridging effect of Ag_2O in pressure-less silver sintering. It showed that the proper number of additives, such as Ag_2O , facilitated the bridging connection between Ag particles, which led to microstructure densification and strength enhancement. Li *et al.* [25] and Mei *et al.* [26] indicated that the sinter joints by current-assisted or ultrasonic-assisted sintering showed significant improvement on

their shear strength. Besides the pressure-less sintering, pressure-assisted sintering is another commonly-used die attach process for power modules. On one hand, the increasing mechanical pressure improves the densification rate and the strength of the sintered layer. On the other, pressure-assisted sintering shows good process stability for industrial production. The application of pressure during sintering process significantly enhances the densification of nanoparticles and thus decreases porosity of sintered interconnection [20]. Le *et al.* [27] used the finite element analysis method to evaluate the reliability of a sintered package. It was found that the pressure-assisted nanosilver sintered package exhibited much higher thermo-mechanical resistance to thermal swings when comparing with soldered ones. Similar results were verified by Fu *et al.* [28]. However, applying pressure aggravates the risk of crack generation in chips and no simulation works have reported this phenomenon in nanosilver sintered power module. Thus it is critical to control the stress in the modules by combining the sintering pressure effect and optimizing the sintering process to improve the yield of production.

As stated above, the stress distributions of the double side sintered power modules under different sintering pressures are investigated. The power module used in this study is a press-pack structure with different geometric size substrates on the double sides of the power chips. Accordingly, there are three sintering sequence designs for this structure. The aim of this chapter is to build the relationship between the stress distributions, the sintering sequences, and the sintering pressures during the sintering processes. Based on the results of experiments and finite element analysis, the best sintering sequence design is provided under various sintering pressures.

5.2. EXPERIMENTAL SET-UP

Figure 5.1 shows the schematic diagram of the sintering design. The whole process includes two parts: the lamination of silver film onto Mo plates and the sintering process. In this study the geometric dimension of the top Mo plate is smaller than that of the bottom Mo plate. Thus three different sintering sequences can be designed for the double side sintering process. In sintering sequence (a) in Figure 5.1 (a), the power chip is sintered onto the bottom Mo plate, and then the top Mo plate is sintered onto the chip with the bottom Mo plate. Figure 5.1(b) shows another possible sintering sequence. Here the top Mo plate is sintered onto the chip at first. Then, the chip with the top Mo plate is sintered onto the bottom Mo plate. Compared with the sintering sequence (a) and (b), there is a more simple sintering method, a one-step process, which is shown in Figure 5.1(c). The bottom Mo, the chip, and the top Mo are put into the sintering tool in sequence, and then they are sintered in one step. In this chapter we use S(a), S(b), and S(c) to represent the sintering sequence (a), (b), and (c), respectively.

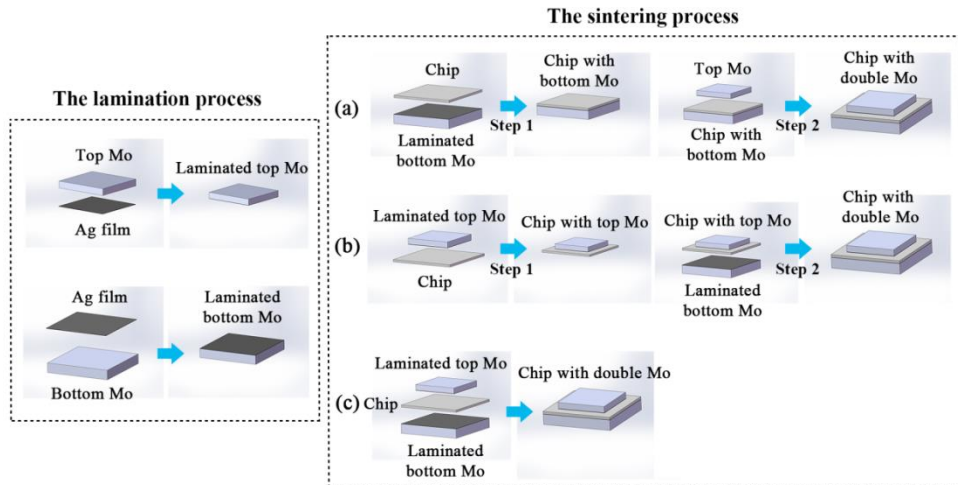


Figure 5.1: Schematic diagrams of the sintering procedures by sequence (a), (b), and (c)

The sintering process is conducted by a pressure sintering equipment as shown in Figure 5.2(a). Before the sintering process, the Ag film is laminated to the Ag-coated Mo layer at 130°C under 5 MPa for 2 min. Figure 5.2(b) and 5.2(c) show the morphology of the surface of the Mo layer before and after being laminated. The power chip used in this study is the dummy Si chip with Ag coating on the surfaces as shown in Figure 5.2(d). The sintering process is conducted at 250°C under 30 MPa for 3 min. Figure 5.2(e) shows the morphology of the well-sintered samples.

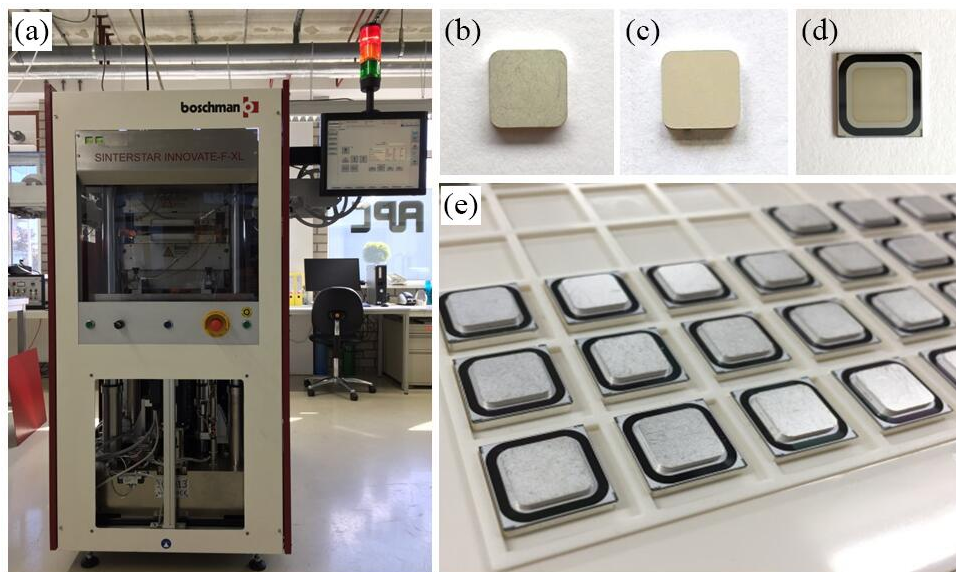


Figure 5.2: Sintering equipment and specimens: (a) Boschman pressure-assisted sintering equipment; (b) Mo layer; (c) laminated Mo layer; (d) power chip, (e) sintered samples

5.3. SIMULATION MODEL

FEA is used to analyze the stress distribution in the samples by different sintering sequences under various sintering pressures (0, 10, 20, and 30 MPa). The 3D FEA model of the power module is built and shown in Figure 5.3. Table 5.1 lists the geometric parameters of each part of the module. Here the size of the top Mo layer is $9.4 \times 9.4 \times 1.2 \text{ mm}^3$, which is smaller than the chip and the bottom Mo layer. Accordingly, the length and the width of the Ag film between the top Mo and the chip is 9.4 mm equally, while the thickness of this film is only $20 \text{ }\mu\text{m}$. Likewise, the Ag film between the chip and the bottom Mo layer has a similar dimension of $13.6 \times 13.6 \text{ mm}^2$ in length and in width.

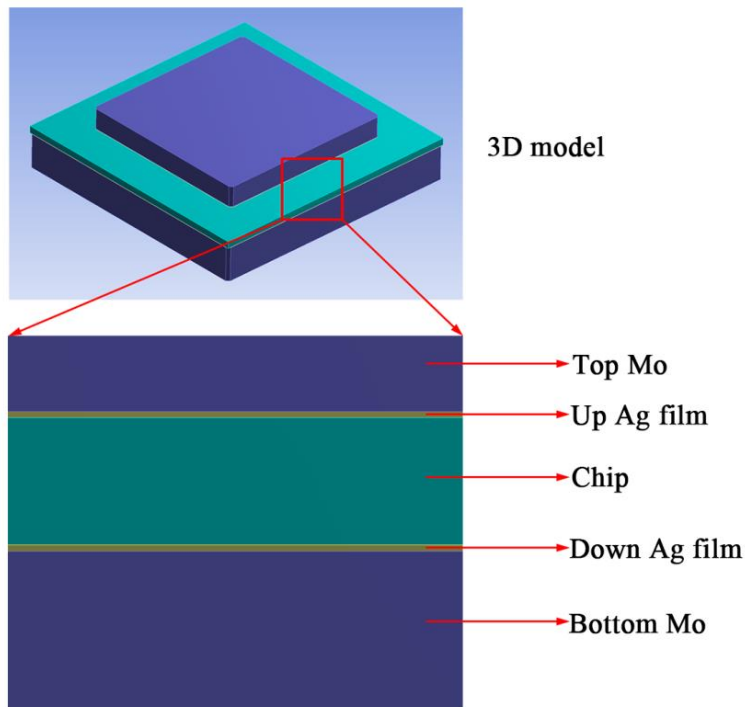


Figure 5.3: 3D model of the double side sintering module

Based on the experimental results, no chip damages appear during the first sintering steps by S(a) and S(b). Meanwhile, the residual stress is limited in the modules after the first sintering steps by S(a) and S(b). Therefore, the simulation works in this study mainly focus on the second sintering steps of S(a) and S(b). By this means, the simulation works are significantly simplified. A simple model as shown in Figure 5.3 can be used for the second steps sintering for S(a) and S(b), as well as the one-step sintering process of S(c). The major differences among these sintering sequences are supposed to be the Young's modulus of the up and the down Ag films in the models. The sintering film used in this

study is mainly formed by Ag nanoparticles and the Young's modulus of the film is very low before sintering process. Literature reported [29] that the Young's modulus of nanoscale Ag film was 2.64 GPa at the temperature of 120°C, and 1.58 GPa at the temperature of 150°C. Based on the data provided, the Young's modulus of the laminated Ag film is set as 0.5 GPa during the sintering process at 250°C. The material properties are summarized in Table 5.1.

Table 5.1: Geometrical size and material properties of each layer [25, 26]

Layer	Length (mm)	Width (mm)	Thickness (mm)	Poisson's ratio	Young's modulus (GPa)	CTE (K ⁻¹)
Top Mo	9.4	9.4	1.2	0.28	320	5.0 × 10 ⁻⁶
Laminated Ag	9.4	9.4	0.02	0.25	0.5	2.03 × 10 ⁻⁵
Chip	13.53	13.53	0.41	0.28	131	4.2 × 10 ⁻⁶
					23°C, 32	
					100°C, 22	
Sintered Ag	13.6	13.6	0.02	0.25	200°C, 32	2.03 × 10 ⁻⁵
					250°C, 6.02	
Bottom Mo	13.6	13.6	2.0	0.28	320	5.0 × 10 ⁻⁶

The Garofalo model [30] is applied for describing the creep properties of sintered Ag layer which has been sintered once, and it can be expressed as:

$$\dot{\epsilon} = A \cdot [\sinh(\alpha \cdot \sigma)]^n \cdot \exp\left(\frac{-E_a}{R \cdot T}\right) \quad (5.1)$$

where $\dot{\epsilon}$ represents the steady state creep rate, σ represents the stress (MPa), R represents the universal gas constant and T represents the temperature (K), A , α , n , E_a are constants and can be defined in Table 5.2.

Table 5.2: Garofalo model parameters

Material	A (s ⁻¹)	α (MPa ⁻¹)	n	E_a (kJ·mol ⁻¹)
Sintered Ag	0.12	0.25	0.9	55.04

In the model by S(a), the upper Ag film is laminated Ag and the Young's modulus is

set as 0.5 GPa. Meanwhile, the down Ag film is sintered Ag and the Young's modulus is summarized in Table 5.1 during the second sintering process. In contrast, the upper Ag film is sintered Ag and the down Ag film is laminated Ag by S(b). For the one step sintering process of S(c), however, both the up and the down Ag films are laminated Ag. The Young's moduli for both are given to be 0.5 GPa during the sintering process.

The sintering temperature is set as 250°C and the sintering time is 3 min. After sintering, the module is cooled down to room temperature within 3 min. The sintering pressure is applied to the top Mo layer uniformly, and the pressure is set as 0, 10, 20, and 30 MPa, respectively. The pressure is only applied during sintering at 250°C. In order to simplify the simulation model, some assumptions are proposed as following: (1) only stress distribution is taken into account when the max stress appears in the modeling. Thus some transformation like the Young's modulus, CTE, and geometric size of the laminated Ag layers are neglected during the sintering process. (2) The thin-coated Ag layers on the surfaces of Mo layers are neglected in the models. (3) The residual stress, which is limited in the one-side sintered module during the first sintering process of S(a) and S(b), is also neglected.

5.4. RESULTS EXPERIMENTS

The morphology of the sintered samples under 30 MPa sintering pressure can be observed in Figure 5.4. As shown in Figure 5.4(a), the power chip is sintered onto the bottom Mo plate in the first sintering procedure by S(a). Figure 5.4(b) shows the double side sintered sample after the second sintering procedure by S(a). No cracks appeared in the modules during both the two sintering procedures by this sintering sequence. Figure 5.4(c) shows the sintered chip with the top Mo plate in the first sintering procedure by S(b). In the second sintering procedure, the sample as shown in Figure 5.4(c) is sintered onto the bottom Mo plate. The double side sintered sample is as shown in Figure 5.4(d), in which clear cracks can be observed in the power chip. The typical distribution of cracks in the samples by S(b) is as described in the schematic diagram in Figure 5.4(e). As shown in Figure 5.1(c), S(c) is a one-step sintering process, during which both the top and the bottom Mo plates are sintered onto the power chip simultaneously. According to the experimental results, there is not any crack on most of the samples by S(c) as shown in Figure 5.4(f), while the others appear cracked chips as presented in Figure 5.4(g). Figure 5.4(h) shows the schematic diagram describing the crack prolongation in Figure 5.4(g).

The numbers of the cracked samples by different sintering sequences are listed in Table 5.3. Firstly, every sintering sequence involved nine samples. It is found that all the nine samples by S(b) show cracked chips. Two chips break during the sintering process by

S(c). In contrast, no crack appears in the chips sintered by S(a). Thus this sintering sequence is used for the batch production of the double side sintering of the power chips and 450 more samples are sintered. The results show that the yield of this sintering process is 100% for all the 450 samples.

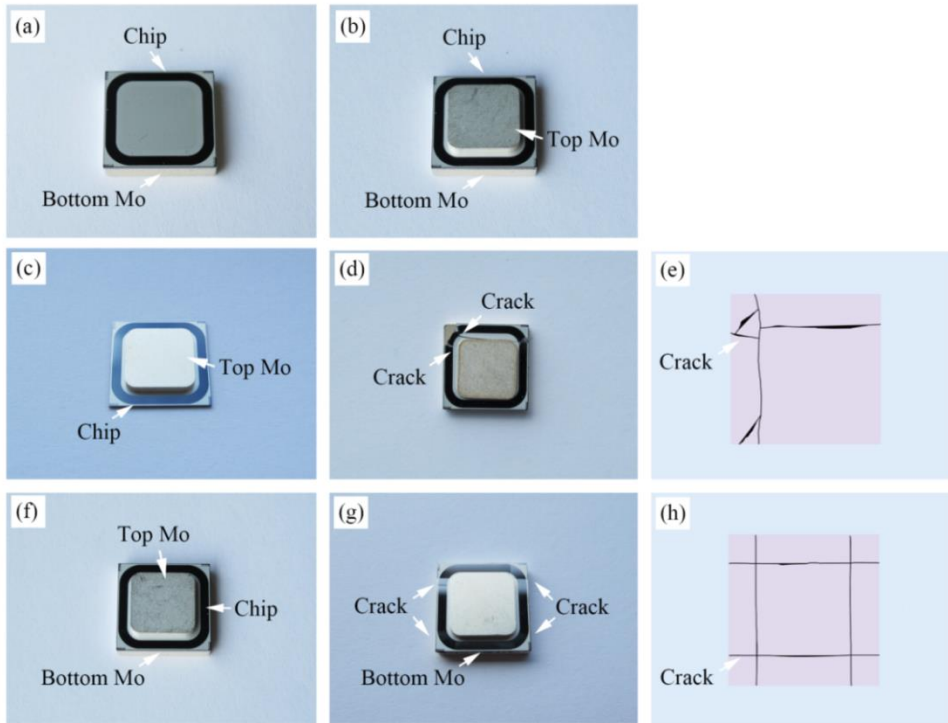


Figure 5.4: Morphology of the sintered samples under 30MPa by different sintering sequences: (a) chip with the bottom Mo by S(a); (b) the double side sintered sample by S(a); (c) chip with the top Mo by S(b); (d) the double side sintered sample by S(b); (e) schematic diagram describing the cracks in (d); (f) good sample by S(c); (g) sample with cracks by S(c); (h) schematic diagram describing the cracks in (g)

Table 5.3: The yield of the samples by different sintering sequences

Sintering sequence	Number of samples	Number of samples with crack	Yield rate
(a)	459	0	100%
(b)	9	9	0
(c)	9	2	78%

For S(a), the chip and bottom Mo have already joined together and formed one new

part in the first sintering process. In the second sintering process, the applied pressure on top Mo will uniformly distributed on the bottom Mo and will not introduce too much stress into the chip. However, for S(b), the silver film between the joined top Mo/chip and the bottom Mo shows low elastic modulus. Also the bottom surface of the chip is unconstrained on the bottom Mo. Therefore, the pressure applied on the top Mo will cause high stress concentration on the chip at the lower corner area of top Mo and lead to the generation of cracks. For S(c), both the top and bottom surfaces of the chip are unconstrained, this gives more flexibility for the deformation of chip and results in lower stress than S(b).

According to the experimental results, we can draw some conclusions as follow:

- (1) All the cracks appear in the chip, which is the weakest part in the power module.
- (2) For the two-step sintering sequences of S(a) and S(b), no crack generates after the first sintering process.
- (3) All the cracks appear during the sintering process at 250°C under 30 MPa instead of the cooling process.

It is of great significance to investigate the stress distribution in the samples during the sintering processes, and then to take the stress as a standard to design the sequence of the sintering processes under various sintering pressures.

5.5. RESULTS SIMULATIONS

Figure 5.5(a) shows the 3D view describing the von Mises stress distribution in the double side sintering model by S(a) at 250°C under 30 MPa sintering pressure. The top view, the bottom view, and the cross sectional view of the module can be observed in Figure 5.5(b), 5.5(c), and 5.5(d), respectively. It is remarkable that the maximum von Mises stress in the whole module is 115 MPa, which is located on the bottom Mo layer. The stress in the up Ag layer is similar to that in the down Ag layer, as shown in Figure 5.5(d).

Because the weakest part in the whole module is suggested to be the chip, more attention should be paid to the stress on the chip than that on the other parts in the module. Figure 5.5(e) shows the von Mises stress distribution on the chip. The top view and the bottom view of the chip can be seen in Figure 5.5(f) and 5.5(g), respectively. As presented in the figures, the maximum von Mises stress on the chip is 63 MPa, which is located on the bottom surface of chip, and the corner area of the corresponding up Ag layer. According to the experimental tests, no damages appear in these layers.

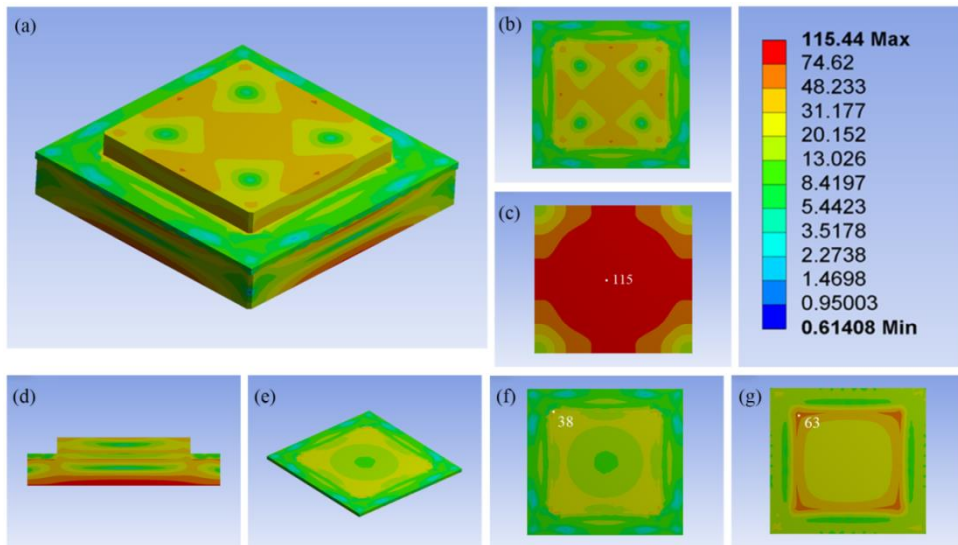


Figure 5.5: Von Mises stress distribution in the model with 30 MPa by S(a). (a) the 3D view of the model; (b) the top-view of the model; (c) the bottom-view of the model; (d) the cross-sectional view of the model; (e) the 3D view of the chip; (f) the top-view of the chip; (g) the bottom-view of the chip

Figure 5.6 shows the von Mises stress distribution in the double side sintering model by S(b) at 250°C under 30 MPa sintering pressure. In contrast to S(a), the upper Ag layer is first sintered with top Mo layer in the model by S(b). Meanwhile, the down Ag layer is the laminated layer whose Young's modulus is 0.5 GPa. As presented in Figure 5.6(d), the maximum von Mises stress in the module by S(b) is 211 MPa, which appears in the corner areas of the upper Ag layer.

The stress distribution on the chip in this model can be seen in Figure 5.6(e), 5.6(f), and 5.6(g). The maximum von Mises stress is 152 MPa on the top surface of the chip. It is observed that the points with maximum von Mises stress are located in the corners where the chip is connected to the up Ag layer. Consequently, the high stress concentration on the chips leads to the generation and prolongation of the cracks during the sintering process by S(b) as shown in Figure 5.4(d) and 5.4(e).

The von Mises stress distribution in the double side sintering model by S(c) at 250°C under 30 MPa is shown in Figure 5.7. In this one step sintering process, the Young's modulus of both the up and the down Ag layers is 0.5 GPa. As presented in the figure, the maximum von Mises stress is 129 MPa which is located on the bottom Mo layer. Meanwhile, as shown in Figure 5.7(e), 5.7(f), and 5.7(g), the maximum von Mises stress on the chip is 85 MPa in this model. The stress concentration areas are mainly located on the back side of chip, and the areas where correspond to the edges of the up Ag layer. As

shown in Figure 5.4(g) and 5.4(h), the experimental results verify that the cracks mainly generate and propagate along the stress concentration areas by S(c).

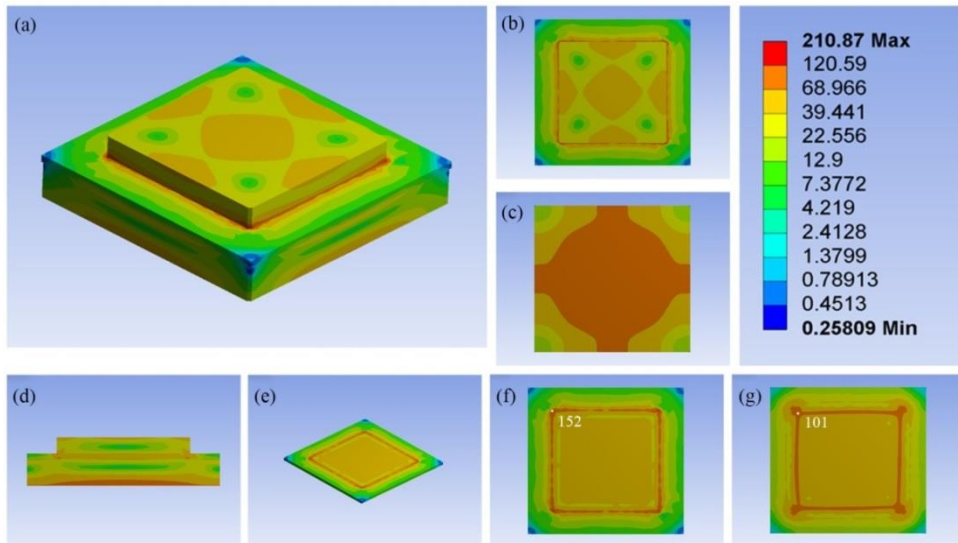


Figure 5.6: Von Mises stress distribution in the model under 30 MPa by S(b). (a) the 3D view of the model; (b) the top-view of the model; (c) the bottom-view of the model; (d) the cross-sectional view of the model; (e) the 3D view of the chip; (f) the top-view of the chip; (g) the bottom-view of the chip

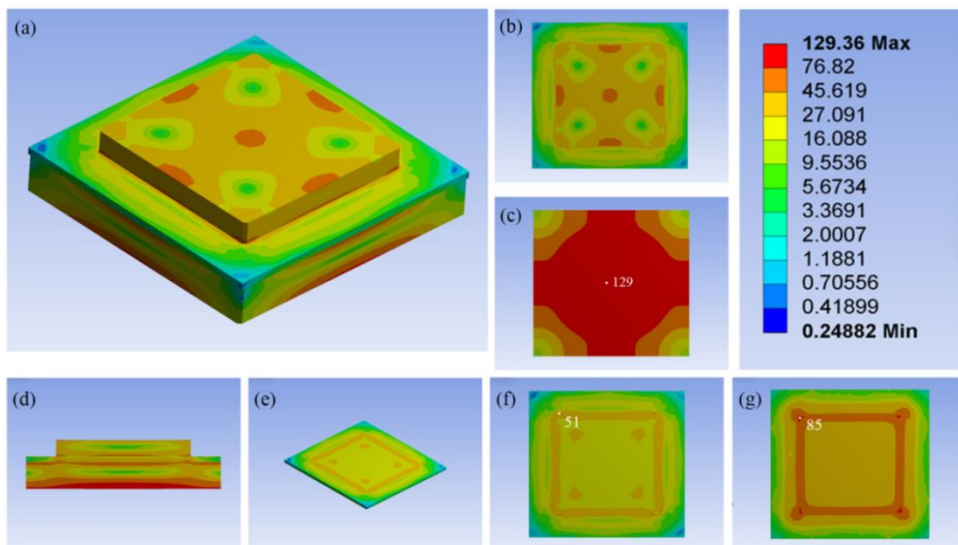


Figure 5.7: Von Mises stress distribution in the model under 30 MPa by S(c). (a) the 3D view of the model; (b) the top-view of the model; (c) the bottom-view of the model; (d) the cross-sectional view of the model; (e) the 3D view of the chip; (f) the top-view of the chip; (g) the bottom-view of the chip

Among the three sintering sequences, the module sintered by S(a) under 30 MPa pressure shows the lowest von Mises stress of 63 MPa on the chip. In contrast, the stress on the chip reaches 152 MPa by S(b), which is the highest in the three sequences. Meanwhile, the maximum von Mises stress on the chip by S(c) is about 85 MPa under the same simulation conditions. It is obvious that the simulation results reach a proper agreement with the experiments. The simulation results of the stress on the chips reflect the possibility of the crack generation on the chips in the experiments. Thus, the stress on the chip is considered as an index for the sintering sequence design under various sintering pressures. The stress distribution in the modules is simulated with various sintering sequences and pressures. The maximum von Mises stress for each sintering condition is shown in Table 5.4.

Table 5.4: Maximum von Mises stress in the modules and on the chips

Pressure (MPa)	Sintering sequence	Maximum von Mises stress (MPa)	Location	Stress on chip ^{up} (MPa)	Stress on chip ^{down} (MPa)
0	a	47	Down Ag layer	27	28
0	b	47	Up Ag layer	30	30
0	c	28	Chip	26	27
10	a	47	Down Ag layer	24	38
10	b	94	Up Ag layer	69	49
10	c	45	Bottom Mo	25	41
20	a	78	Bottom Mo	28	51
20	b	151	Up Ag layer	111	76
20	c	87	Bottom Mo	36	63
30	a	115	Bottom Mo	38	63
30	b	211	Up Ag layer	152	101
30	c	129	Bottom Mo	51	85

Because chip is the weakest part in the module, it is vital to concern the maximum von Mises stress on the chip during the sintering process. Figure 5.8 presents the maximum von Mises stress on the chips under various sintering conditions. As indicated in the figure, the chips show much higher maximum von Mises stress by S(b) than by the other two sintering sequences. The chips by S(a) shows the lowest maximum von Mises stress among all the three sintering sequences. With the increase of sintering pressure

from 0 to 30 MPa, the maximum von Mises stress on the chips by all the three sintering sequences increase. Although the one step sintering of S(c) is the most effective process, it will induce higher stress on chip and thus bring more risks to the reliability of chip when comparing with S(a). Thus, S(a) is highly recommended for the double side sintering process.

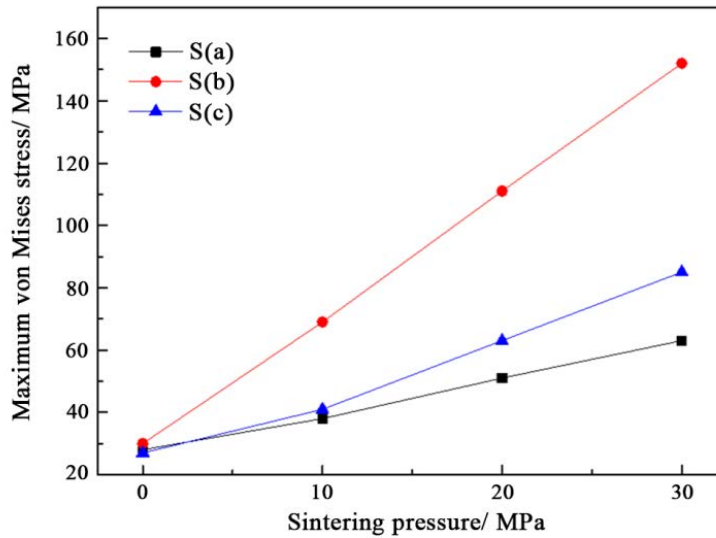


Figure 5.8: Effect of sintering pressure on the maximum von Mises stress on the chips

5.6. SUMMARY

The chip, where cracks may generate during the pressure-assisted sintering process, is the weakest part in the double sintered module. Designing proper sintering sequences is positive to suppress the generation of cracks. When the sintering pressure is 30 MPa, the chip sintered by S(b) shows the highest von Mises stress. In contrast, the chip that sintered by S(a) showed the lowest von Mises stress. The increase of the sintering pressure (0 to 30 MPa) elevates the maximum von Mises stress on the power chips for all the modules by different sintering sequences. Moreover, the maximum von Mises stress on the chip by S(a) shows the lowest stress level. Combining the test results and simulation results, S(a) is recommended as the best sintering sequence because of its high yield rate and lowest von Mises stress on the power chip.

REFERENCES

- [1] Y. Liu, H. Zhang, L. Wang, X. Fan, G. Zhang, and F. Sun, *Stress analysis of pressure-assisted sintering for the double-side assembly of power module*,

- Soldering & Surface Mount Technology **31**, 20 (2018).
- [2] M. Gleissner and M.M. Bakran, *Design and control of fault-tolerant nonisolated multiphase multilevel DC-DC converters for automotive power systems*, IEEE Transactions on Industry Applications **52**, 1785 (2016).
- [3] M.A. Khan, I. Husain, and Y. Sozer, *A bidirectional DC-DC converter with overlapping input and output voltage ranges and vehicle to grid energy transfer capability*, IEEE Journal of Emerging and Selected Topics in Power Electronics **2**, 507 (2014).
- [4] Y. Peng, P. Sun, L. Zhou, X. Du, and J. Cai, *A temperature-independent method for monitoring the degradation of bond wires in IGBT modules based on transfer characteristics*, in *IEEE Applied Power Electronics Conference and Exposition (APEC 2017)*, 2017, pp. 751-755.
- [5] P. Ghimire, A.R. Vega, S. Beczkowski, B. Rannestad, S. Munk-Nielsen, and P. Thogersen, *Improving power converter reliability: Online monitoring of high-power IGBT modules*, IEEE Industrial Electronics Magazine **8**, 40 (2014).
- [6] H. Luo, Y. Chen, P. Sun, W. Li, and X. He, *Junction temperature extraction approach with turn-off delay time for high-voltage high-power IGBT modules*, IEEE Transactions on Power Electronics **31**, 5122 (2016).
- [7] J.L. Marchesini, P.O. Jeannin, Y. Avenas, J. Delaine, C. Buttay, and R. Riva, *Implementation and switching behavior of a PCB-DBC IGBT module based on the power chip-on-chip 3-D concept*, IEEE Transactions on Industry Applications **53**, 362 (2017).
- [8] S. Chua and K.S. Siow, *Microstructural studies and bonding strength of pressureless sintered nano-silver joints on silver, direct bond copper (DBC) and copper substrates aged at 300°C*, Journal of Alloys and Compounds **687**, 486 (2016).
- [9] F. Dugal and M. Ciappa, *Study of thermal cycling and temperature aging on PbSnAg die attach solder joints for high power modules*, Microelectronics Reliability **54**, 1856 (2014).
- [10] L.L. Liao, T.Y. Hung, C.K. Liu, W. Li, M.J. Dai, and K.N. Chiang, *Electro-thermal finite element analysis and verification of power module with aluminum wire*, Microelectronic Engineering **120**, 114 (2014).
- [11] P. Pougnet, G. Coquery, R. Lallemand, and A. Makhloufi, *Power module thermal cycling tester for in-situ ageing detection*, Microelectronics Reliability **76-77**, 544

- (2017).
- [12] U.M. Choi, F. Blaabjerg, and K.B. Lee, *Study and handling methods of power IGBT module failures in power electronic converter systems*, IEEE Transactions on Power Electronics **30**, 2517 (2015).
- [13] C. Durand, M. Klingler, M. Bigerelle, and D. Coutellier, *Solder fatigue failures in a new designed power module under Power Cycling*, Microelectronics Reliability **66**, 122 (2016).
- [14] W.H. Chen, C.F. Yu, H.C. Cheng, Y.M. Tsai, and S.T. Lu, *IMC growth reaction and its effects on solder joint thermal cycling reliability of 3D chip stacking packaging*, Microelectronics Reliability **53**, 30 (2013).
- [15] Y. Liu, F. Sun, H. Zhang, T. Xin, C.A. Yuan, and G. Zhang, *Interfacial reaction and failure mode analysis of the solder joints for flip-chip LED on ENIG and Cu-OSP surface finishes*, Microelectronics Reliability **55**, 1234 (2015).
- [16] E.C. Yeh, W. Choi, K. Tu, P. Elenius, and H. Balkan, *Current-crowding-induced electromigration failure in flip chip solder joints*, Applied Physics Letters **80**, 580 (2002).
- [17] A. Hutzler, A. Tokarski, S. Kraft, S. Zischler, and A. Schletz, *Increasing the lifetime of electronic packaging by higher temperatures: Solders vs. silver sintering*, in *IEEE 64th Electronic Components and Technology Conference (ECTC 2014)*, 2014, pp. 1700-1706.
- [18] R. Khazaka, L. Mendizabal, and D. Henry, *Review on joint shear strength of nano-silver paste and its long-term high temperature reliability*, Journal of Electronic Materials **43**, 2459 (2014).
- [19] S.A. Paknejad and S.H. Mannan, *Review of silver nanoparticle based die attach materials for high power/temperature applications*, Microelectronics Reliability **70**, 1 (2017).
- [20] S. Zabihzadeh, S. Van Petegem, L. Duarte, R. Mokso, A. Cervellino, and H. Van Swygenhoven, *Deformation behavior of sintered nanocrystalline silver layers*, Acta Materialia **97**, 116 (2015).
- [21] T. Youssef, W. Rmili, E. Woirgard, S. Azzopardi, N. Vivet, D. Martineau, R. Meuret, G. Quilliec, and C. Richard, *Power modules die attach: A comprehensive evolution of the nanosilver sintering physical properties versus its porosity*, Microelectronics Reliability **55**, 1997 (2015).

- [22] T. Herboth, M. Guenther, A. Fix, and J. Wilde, *Failure mechanisms of sintered silver interconnections for power electronic applications*, in *IEEE 63rd Electronic Components and Technology Conference (ECTC 2013)*, 2013, pp. 1621-1627.
- [23] P. Peng, A. Hu, A.P. Gerlich, G. Zou, L. Liu, and Y.N. Zhou, *Joining of silver nanomaterials at low temperatures: processes, properties, and applications*, *ACS Applied Materials & Interfaces* **7**, 12597 (2015).
- [24] H. Zhang, Y. Gao, J. Jiu, and K. Suganuma, *In situ bridging effect of Ag₂O on pressureless and low-temperature sintering of micron-scale silver paste*, *Journal of Alloys and Compounds* **696**, 123 (2017).
- [25] Y. Li, H. Jing, Y. Han, L. Xu, and G. Lu, *Microstructure and joint properties of nano-silver paste by ultrasonic-assisted pressureless sintering*, *Journal of Electronic Materials* **45**, 3003 (2016).
- [26] Y.H. Mei, Y. Cao, G. Chen, X. Li, G.Q. Lu, and X. Chen, *Characterization and reliability of sintered nanosilver joints by a rapid current-assisted method for power electronics packaging*, *IEEE Transactions on Device and Materials Reliability* **14**, 262 (2014).
- [27] F. Henaff, S. Azzopardi, E. Woïrgard, T. Youssef, S. Bontemps, and J. Joguet, *Lifetime evaluation of nanoscale silver sintered power modules for automotive application based on experiments and finite-element modeling*, *IEEE Transactions on Device and Materials Reliability* **15**, 326 (2015).
- [28] S. Fu, Y. Mei, X. Li, C. Ma, and G.Q. Lu, *Reliability evaluation of multichip phase-leg IGBT modules using pressureless sintering of nanosilver paste by power cycling tests*, *IEEE Transactions on Power Electronics* **32**, 6049 (2017).
- [29] D. Yu, X. Chen, G. Chen, G. Lu, and Z. Wang, *Applying Anand model to low-temperature sintered nanoscale silver paste chip attachment*, *Materials & Design* **30**, 4574 (2009).
- [30] C. Weber, H. Walter, M. Dijk, M. Hutter, O. Wittler, and K.D. Lang, *Combination of experimental and simulation methods for analysis of sintered Ag joints for high temperature applications*, in *IEEE 66th Electronic Components and Technology Conference (ECTC 2016)*, 2016, pp. 1335-1341.

6

APPLICATION OF NANOSILVER SINTERING IN CERAMIC PACKAGES

High reliable packaging materials are needed for electronics when they are subjected to harsh environments. Among which, the nanosilver material has been widely studied and applied in power electronics due to its low processing temperature and high reliability. This chapter investigates the bonding properties of nanosilver sintered hermetic cavities. There are two kinds of lids used in this study, including copper lid and silicon lid. The X-ray and C-Mode Scanning Acoustic Microscopy (C-SAM) are used to evaluate the bonding quality of sintered layer. The results reveal that delamination tends to happen in Cu lid sintered cavity. However, no delamination or cracks are found in the Si lid sintered cavity. Finite element analysis (FEA) method is employed to investigate the effects of lid materials on the stress distribution of lid. The simulation results indicate that the Cu lid sintered cavity shows a much higher stress than the Si lid sintered cavity after sintering. Besides, the effects of sintering pressure on the evolution of stress distribution on two kinds of lids are studied. There is no obvious change in the stress distribution areas on Cu lid with the increasing of pressures from 5 to 30 MPa. However, the stress distribution on Si lid expands obviously only when the sintering pressure increases to 30 MPa. With the increase of sintering pressure from 5 to 30 MPa, the maximum stresses on Cu lid are almost the same, while increasing trend is found on Si lid.

6.1. INTRODUCTION

Electronics, operating at harsh environment, are usually suffering extremely high/low temperature shock and high pressure, when they are applied in the areas of renewable energy, aerospace engine, oil and gas drilling and production [2-5]. Some of these electronics need to be hermetically sealed to prevent the deterioration of function and reliability.

The hermeticity is usually achieved by using various sealing methods, such as thermocompression bonding [6-8], soldering [9-11], glass frit bonding [12, 13], seam welding [14] and anodic bonding [15, 16]. Among these methods, the Au-Sn eutectic soldering technology is one of the widely used hermetic seal methods due to its favorable mechanical strength, flux-free process, and hermeticity [17, 18]. Zhang *et al* [19] designed an electrical test method to monitor the bonding quality of AuSn eutectic soldered micro-electro-mechanical systems (MEMS) cavities. They found that the sample with a lower resistivity owned a thicker (Au, Ni)₃Sn₂ phase at the bonding interface and a lower bonding strength. Demir *et al* [20] fabricated the thermal evaporated Au and Sn layers as a seal ring in MEMS cavity. The bonding was achieved by the formation of Au-Sn intermetallic compounds (IMC) and the average shear strength can reach 23 MPa. Rautiainen *et al* [17] used the Au-Sn seal ring for bonding silicon wafers and caps through solid-liquid interdiffusion (SLID) method. The bonded wafers with Ni layer between the TiW adhesion layer showed quite high shear strength while voids were found at the shear and tensile fracture surface.

However, the processing temperature (over 300°C) of Au-Sn eutectic solder is quite high, which may introduce the thermal induced stress concentration and damage in the electronic components. Although the Au-Sn stacked metal layers in SLID method can be processed at temperatures around 235°C, the complicated deposition procedure and processing technology limit its further application. Furthermore, the excessive growth of IMC may decrease the bonding strength of joint because of its brittle nature [21, 22]. In addition, the cost of Au-Sn eutectic alloy is also quite high. So there is an urgent need for developing a new sealing material that can work steadily at harsh environments.

Recently, the nanosilver sintering technology has attracted a lot of attention in the die attach process of power semiconductor fields. This process can be achieved at low temperature around 250°C and served at relative high environment temperatures over 200°C [23, 24]. Comparing with the traditional Au-Sn eutectic soldering method, the nanosilver sintering technology offers relatively lower processing temperature and higher reliability. Until now, there are few publications reporting the application of nanosilver sintering technology in hermetic sealing process.

This chapter investigates the bonding properties of nanosilver sintered hermetic cavity. The bonding qualities of sintered Ag layer are examined using X-ray and C-Mode Scanning Acoustic Microscopy (C-SAM) imaging methods. The effects of lid materials and sintering pressure on the stress distribution of sintered cavity are investigated by FEA method.

6.2. EXPERIMENTAL SET-UP

The ceramic cavity (Al_2O_3) with a gold (Au) coating layer ($10\ \mu\text{m}$) on the top surface was used in this study. The sealing material was nanosilver film (Ag film), which has a thickness of $65\ \mu\text{m}$ (from Alpha Assembly Solutions). The Ag film was cut by laser into hollow square shape with a width of $0.22\ \text{mm}$ according to the sealing area on the top surface of the cavity. There are two kinds of lids used in this study, including copper (Cu) and silicon (Si) based ones. Both two kinds of lids were coated with silver on the top surface of sealing area. The materials, sintering equipment and the two processing steps were shown in Figure 6.1.

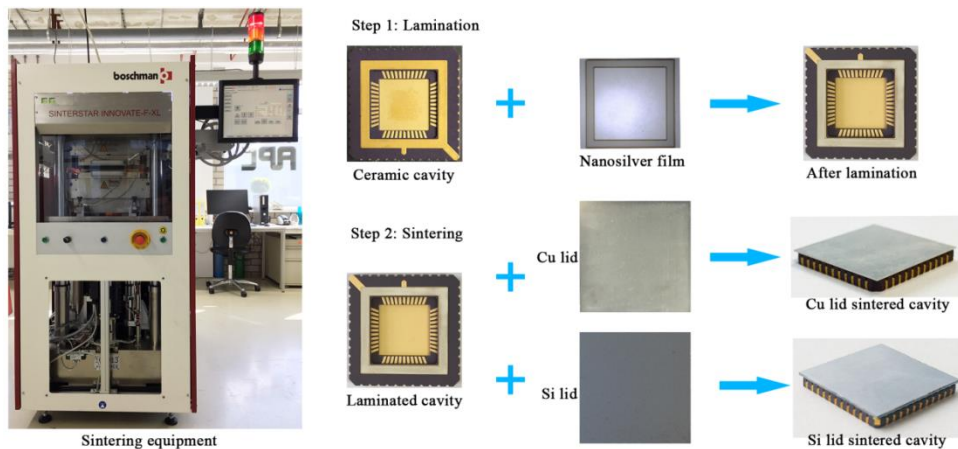


Figure 6.1: Sintering equipment and sample preparation

The whole manufacture process includes two steps: firstly, the Ag film cut by laser was laminated on the gold layer of the cavity at 130°C for 2 min with a pressure of 5 MPa. Secondly, the lid was assembled on the laminated cavity and then the whole cavity was placed in the mold inside of the sintering equipment. Note that the lid was placed on the bottom side and the cavity was placed on the top side. The whole cavity was then directly sintered at 250°C for 5 min by a precisely controlled and monitored system from Boschman Technologies. The sintering process was achieved at the atmosphere. In order to get a dense microstructure and high mechanical strength, a pressure of 10 MPa was applied through the dynamic insert during the sintering process. This dynamic insert can

help to ensure a uniform pressure through a real time feedback system.

After sintering, the sample was taken out from the equipment and cooled down to room temperature for 3 min. The sintered cavity was further detected in X-ray imaging system to check the cracks in the bonding layer. The sintered cavity was also examined through C-SAM test to determine whether delamination existed or not. Finally, the bonding quality of nanosilver sintered cavity was evaluated through the captured images in the two tests.

6.3. SIMULATION METHODOLOGY

The FEA method is used to determine the residual stress in the sintered cavity during sintering process. The structure of the cavity is shown in Figure 6.2, it consists of four layers: lid (Cu or Si), sintered Ag layer, Au coating and cavity (Al_2O_3). During simulation, the package is first heated up to 250°C from room temperature within 1 min and then kept at 250°C for 5 min. The sintered package is cooled down to room temperature within 3 min. The sintering pressure of 5 (or 10, 20, 30) MPa is applied on the back side of the cavity during heating and sintering. The large deflection function is turned on to better predict the deformation of lid. The general material properties used for simulation are summarized in Table 6.1.

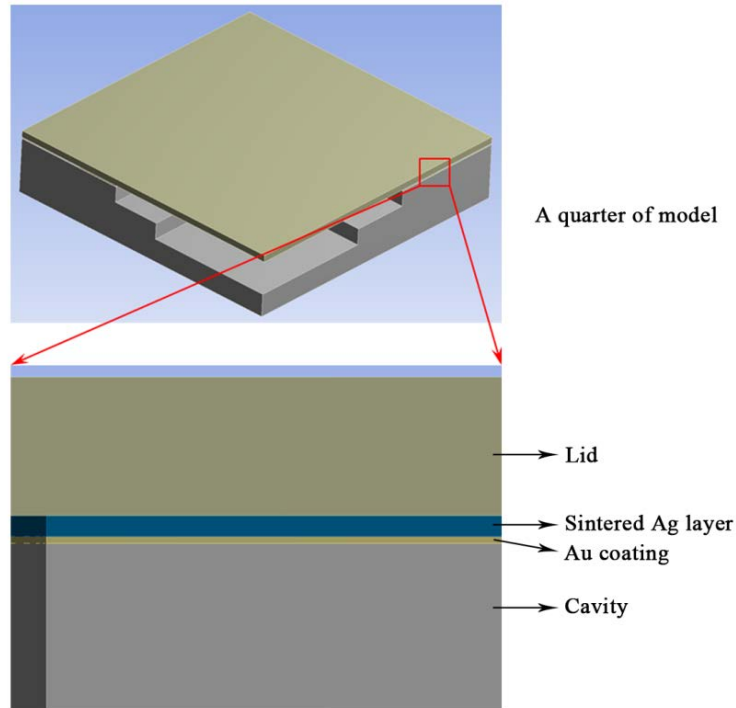


Figure 6.2: 3D structure of a quarter model for simulation

Table 6.1: Material properties adopted in simulation [25-28]

Material	Length (mm)	Width (mm)	Thickness (mm)	Young's modulus (GPa)	Poisson ratio	CTE ($10^{-6} \cdot K^{-1}$)
Si	16.5	16.5	0.52	130.8	0.28	4.2
Cu	16.5	16.5	0.2	110	0.34	17
Sintered Ag	-	0.22	0.03	23°C, 32 100°C, 22 200°C, 12	0.25	20.3
Au	-	0.22	0.01	80	0.30	14
Al ₂ O ₃	16.5	16.5	1.645	370	0.22	6.8

Some assumptions are applied to the 3D model to save computational time without affecting the accuracy of the solution: the 3D model is regarded as a symmetrical one, so only a quarter of the model is built for simulation; the surface coatings on the Cu and Si lid are neglected in the 3D model; the sintered silver layer is considered as a uniform and constant material.

Since the processing temperature is quite high, so the elastic-plastic models are applied for sintered Ag layer and Cu lid. The Garofalo law is a time dependent model, which describes the function between stress and temperature with a sine hyperbolic creep law is used for sintered Ag layer, can be expressed in Eq. (6.1) [25]:

$$\dot{\varepsilon} = A \cdot [\sinh(\alpha \cdot \sigma)]^n \cdot \exp\left(\frac{-E_a}{R \cdot T}\right) \quad (6.1)$$

where $\dot{\varepsilon}$ is the steady state creep rate, σ is the stress in MPa, R the universal gas constant and T is the temperature in K, the other four constants A , α , n , E_a are defined in Table 6.2.

Table 6.2: Constants for Garofalo law [25]

Material	A (s ⁻¹)	α (MPa ⁻¹)	n	E_a (kJ·mol ⁻¹)
Sintered Ag	0.12	0.25	0.9	55.04

The Chaboche model is used to describe the nonlinear kinematic hardening behavior of the Cu lid. The yield function of Chaboche model can be expressed as Eq. (6.2) [29, 30]:

$$F = \sqrt{\frac{3}{2}(s - \alpha)(s - \alpha)} - Y = 0 \quad (6.2)$$

where s is the deviator stress, α is the back stress and Y is the yield stress of material. The back stress α in the Chaboche model can be described as Eq. (6.3) and Eq. (6.4):

$$\alpha = \sum_{i=1}^n \alpha_i \quad (6.3)$$

$$\Delta\alpha_i = \frac{2}{3}C_i \cdot \Delta\varepsilon^{pl} - \gamma_i\alpha_i \cdot \Delta\varepsilon^{pl} + \frac{1}{c_i} \frac{dC_i}{d\theta} \Delta\theta \cdot \alpha \quad (6.4)$$

where ε^{pl} represents the accumulated plastic strain, θ represents the temperature, C_i and γ_i are the material parameters in the Chaboche model, C_i represents the initial hardening modulus, the decreasing rate of hardening modulus with the increase of plastic strain is controlled by γ_i , i represents the number of kinematic models, here $i = 1, 2$. The parameters of the Chaboche model for the Cu lid are given in Table 6.3, and the yield stress of Cu that varies with temperature is described in Table 6.4.

Table 6.3: Parameters for Chaboche model of Cu [29]

Temperature (°C)	C_1 (MPa)	γ_1	C_2 (MPa)	γ_2
20	54041	962	721	1.1
50	52880	1000	700	1.1
150	45760	1100	600	1.1
250	38040	1300	400	10

Table 6.4: Yield stress of Cu at various temperatures [30]

Material	20°C	50°C	150°C	250°C
Yield stress of Cu	210 MPa	208 MPa	201 MPa	170 MPa

6.4. EVALUATION OF BONDING QUALITY

The X-ray and C-SAM tests are conducted to the sintered cavities, and the results are shown in Figure 6.3. The dark hollow square in the X-ray image represents the sintered Ag layer, and the corresponding area can be seen in C-SAM image. Figure 6.3(a) is the Cu lid sintered cavity, and the image in the middle is the partial enlarged view of bottom right corner. Based on the test results, it can be seen that there is no crack observed in the

sintered Ag layer in Cu lid sintered cavity. However, the sintered Ag layer is not flat and it is not continuously connected in the horizontal direction. This result indicates that delamination is quite serious in the sintered Ag layer and it will result in a weak bonding between the Cu lid and cavity. In the contrast, the sintered Ag layer in Si lid sintered cavity is quite smooth and flat, as shown in Figure 6.3(b). There is no visible crack or delamination inside the sintered Ag layer, which implies a good bonding between the Si lid and cavity.

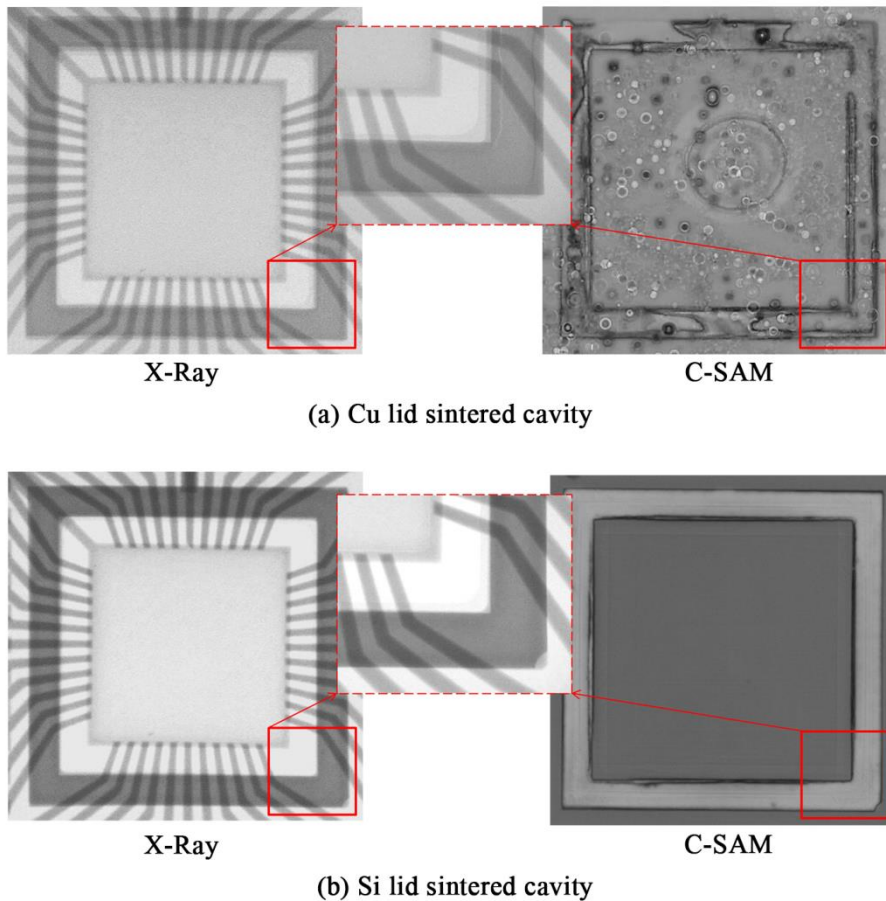


Figure 6.3 X-ray and C-SAM images of nanosilver sintered cavities

In the sintering process, the temperature on lid rapidly rises to 250°C within 60 s. The Cu lid deforms with temperature rising, and the applied pressure (10 MPa) makes the deformation even more serious. During which, the nanosilver particles inside the film begin to coalesce with adjacent particles and form a relatively dense microstructure. This sintered Ag layer has a high Young's modulus and hinders the recovery of deformed Cu lid in the cooling process. Meanwhile, certain stress is also induced in the sintered Ag layer and weakens the bonding quality, and finally results in the delamination. However,

since the Si lid has a much lower CTE than the Cu lid, less residual stress is generated in Si lid during sintering process when comparing with the Cu lid. What's more, the thickness of Cu lid is thinner than the Si lid, which also contributed to the high stress in Cu lid. Hence, the nanosilver sintered Si lid cavity has a better bonding quality than the Cu lid sintered one. In order to further verify the test results, the FEA method is employed to simulate the residual stress resulted from the sintering process.

6.5. STRESS DISTRIBUTION ANALYSIS OF SINTERED CAVITY

In order to furtherly understand how the lid material affects the sintering quality in the sealed cavity bonded by nanosilver, the FEA method is applied to simulate the residual stress distribution in the sintered cavity during sintering process. The Von Misses stress distributions of Cu lid and Si lid sintered cavities after sintering are shown in Figure 6.4 and Figure 6.5, respectively. As shown in Figure 6.4(a), the stress concentration tends to happen in the central part of the Cu lid, and the outer corner area of Cu lid exhibits the lowest stress level. By combining Figure 6.4(b), 6.4(c), 6.4(d) and 6.4(e), the maximum stress of 196 MPa is determined, which locates along the two sides of sintered Ag layer. The sintered Ag layer also has a quite high stress about 109 MPa around the outer corner area and delamination tends to occur at this area, as shown in Figure 6.4(d). What's more, the central part of sintered Ag layer at each side gains the relative low stress and will not greatly decrease the bonding quality of sintered Ag layer. Those results have a good agreement with the X-ray and C-SAM results in Figure 6.3(a). Since the cavity is ceramic (Al_2O_3) based material, only 65 MPa maximum stress is generated because of the high Young's modulus of itself, as seen in Figure 6.4(e).

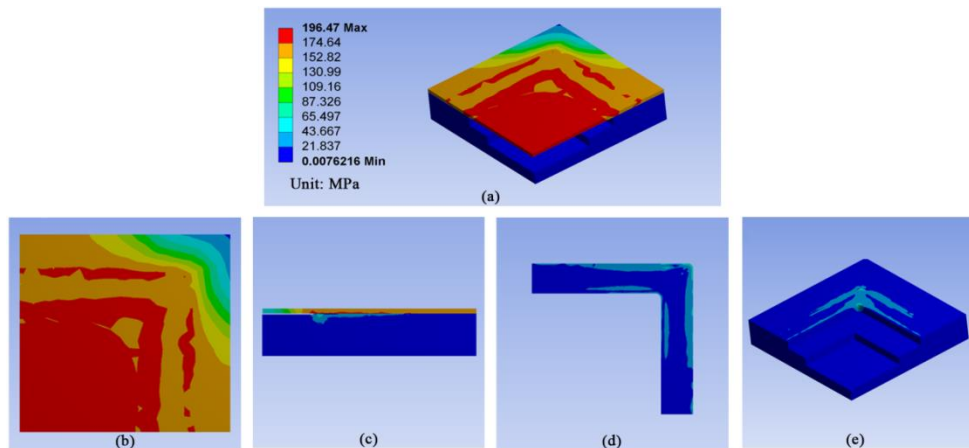


Figure 6.4: Stress distribution of Cu lid sintered cavity, (a) 3D model; (b) top view of Cu lid; (c) cross sectional view of 3D model; (d) top view of sintered Ag layer; (e) 3D view of cavity

While in the Si lid sintered cavity, the stress concentration mainly locates on the corner area of sintered Ag layer on Si lid, as shown in Figure 6.5(a). According to the simulation results in Figure 6.5(b), 6.5(c), 6.5(d) and 6.5(e), the maximum stress of 26 MPa is generated on the top surface of the Si lid and the area of the outer corner of sintered Ag layer. Except the four stress concentration corner areas on Si lid, relative low stress distributes on the whole lid. Similar results are also found in the sintered Ag layer in Figure 6.5(d) and the cavity in Figure 6.5(e).

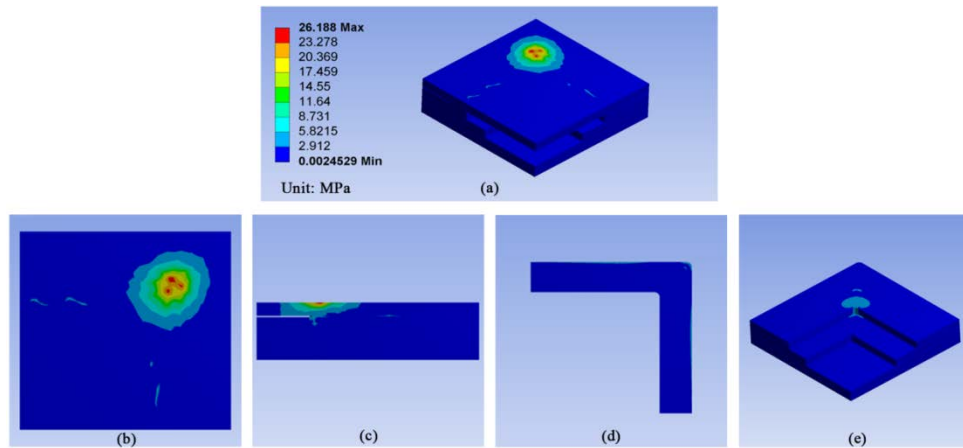


Figure 6.5: Stress distribution of Si lid sintered cavity, (a) 3D model; (b) top view of Si lid; (c) cross sectional view of 3D model; (d) top view of sintered Ag layer; (e) 3D view of cavity

Comparing the stress distribution of Cu lid and Si lid sintered cavities, the maximum stress on Cu lid is much higher than that on Si lid. What's more, the stress distribution area on Cu lid is much larger than the Si lid. Since the Cu lid has a lower Young's modulus and a higher CTE than the Si lid, it is more easily to deform, especially when sintering at 250°C. When cooling down, the recovery of the central part of Cu lid is constrained by the sintered Ag layer and causes the high stress distribution, especially at the two sides of the sintered layer. The high stress level and large stress distribution area on Cu lid will lead to the delamination of sintered Ag layer. Therefore, the Si lid is more suitable for the nanosilver sintered hermetic cavities. Additional simulation works have been done to investigate how the sintering pressure affects the stress distribution on lid.

The sintering pressure can help the sintered Ag layer to get a dense microstructure by increasing the contact area among Ag particles [31, 32]. At the meantime, the sintering pressure will also introduce residual stress and deformation into lid. Figure 6.6 shows the stress distribution of Cu lid under various sintering pressures. With the increase of sintering pressure from 5 MPa to 30 MPa, the stress distribution areas on Cu lid are almost the same. The stress has already reached 196 MPa even when sintered at 5 MPa.

Since the applied pressure is much lower than the generated stress on lid, so the sintering pressure will not greatly affect the stress on lid.

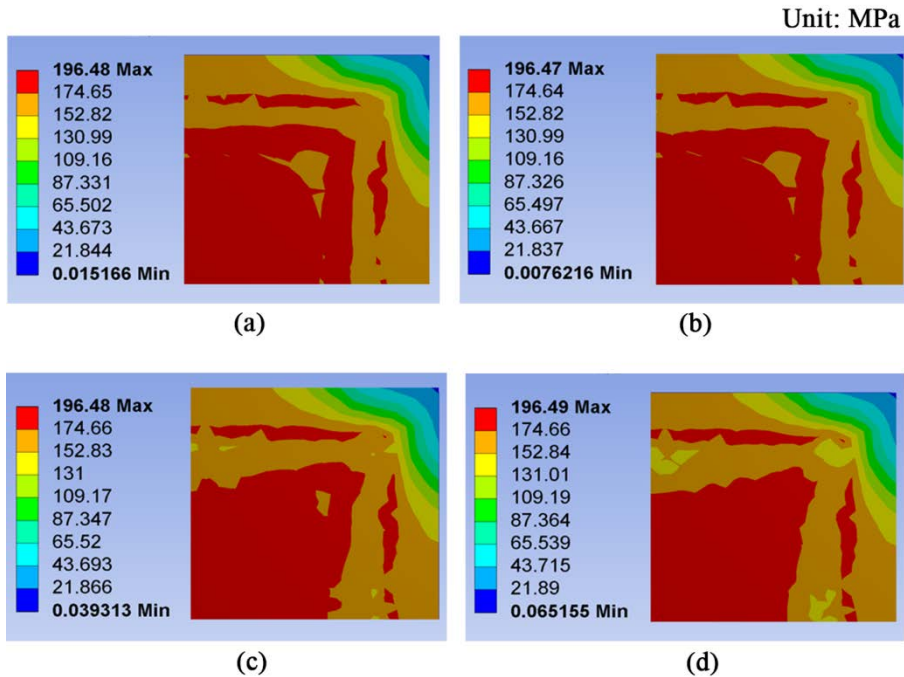


Figure 6.6: Effects of sintering pressure on stress distribution of Cu lid (a) 5 MPa; (b) 10 MPa; (c) 20 MPa; (d) 30 MPa

However, the stress distribution areas on Si lid are mainly located at the corner area of sintered Ag layer, as shown in Figure 6.7. The distribution edge of stress on Si lid tends to stretch along the sintered Ag layer. Once the sintering pressure increases to 30 MPa, the stress distributes around the whole sintered Ag layer area on the Si lid. The maximum stress increases from 18 MPa to 67 MPa when the sintering pressure increases from 5 MPa to 30 MPa.

The maximum stresses on Cu lid and Si lid after sintering at various pressures are shown in Figure 6.8. With the increase of sintering pressure from 5 MPa to 30 MPa, the stress on Cu lid is nearly the same, but the stress on Si lid shows an increasing trend. The maximum stress on Cu lid is much higher than that on Si lid at each sintering pressure. The high stress on Cu lid will decrease the bonding quality of the sintered Ag layer and finally cause the delamination of the sintered Ag layer from both the Cu lid and cavity. Since the Si lid has a lower CTE and a higher Young's modulus than Cu lid, therefore, less deformation and stress will be generated during sintering and cooling process. With the increase of sintering pressure, the deformation of Si lid increases accordingly. The increased deformation of Si lid will further lead to the increase of stress.

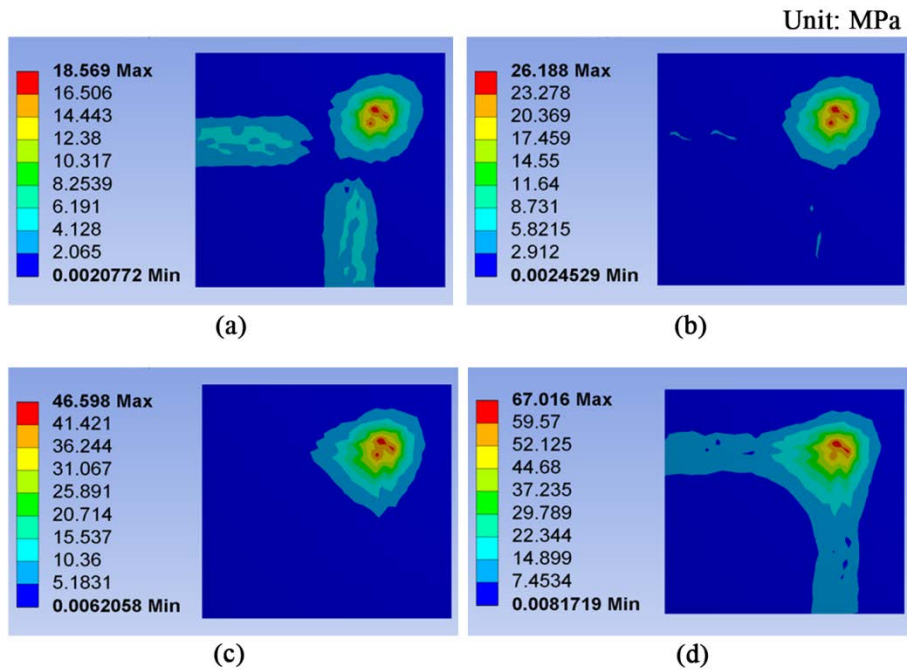


Figure 6.7: Effects of sintering pressure on stress distribution of Si lid (a) 5 MPa; (b) 10 MPa; (c) 20 MPa; (d) 30 MPa

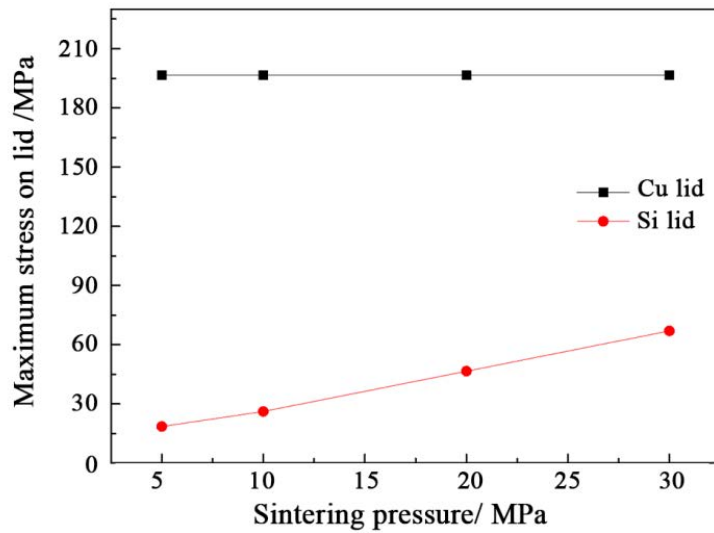


Figure 6.8: Effects of sintering pressure on stress distribution of lid

6.6. SUMMARY

The Cu lid and Si lid can be bonded with ceramic cavity by using nanosilver sintering technology. However, delamination is found in Cu lid sintered cavity. The Si lid sintered

cavity shows good bonding quality and no crack or delamination is detected. After sintering at 10 MPa, the maximum stress areas on Cu lid are mainly located at the central part of lid. While the maximum stress areas on Si lid are located on the top surface of lid and the outer corner area of the sintered Ag layer. However, the Cu lid has a much higher maximum stress than Si lid. There is no significant change in the stress distribution areas on Cu lid with pressure increasing. However, the stress mainly distributes around the corner area of sintered Ag layer on Si lid when the sintering pressure is below 20 MPa. Comparing with the maximum stresses on Cu lid, the maximum stresses on Si lid show increasing trend with the increase of sintering pressure from 5 MPa to 30 MPa.

REFERENCES

- [1] H. Zhang, Y. Liu, L. Wang, J. Fan, X. Fan, F. Sun, and G. Zhang, *A new hermetic sealing method for ceramic package using nanosilver sintering technology*, *Microelectronics Reliability* **81**, 143 (2018).
- [2] K.Y. Au, D.M. Zhi, V. Chidambaram, B. Lin, K. Piotr, and C. KaiLiang, High temperature durable hermetic sealing material selection and reliability comparison for IR gas sensor module packaging, in *IEEE 18th Electronics Packaging Technology Conference (EPTC 2016)*, 2016, pp. 1-5.
- [3] D.R.M. Woo, J.A.K. Yun, Y. Jun, E.W.L. Ching, and F. Che, *Extremely high temperature and high pressure (x-HTHP) durable SOI device & sensor packaging for deep sea, oil and gas applications*, in *IEEE 16th Electronics Packaging Technology Conference (EPTC 2014)*, 2014, pp. 16-21.
- [4] P. Hagler, P. Henson, and R.W. Johnson, *Packaging technology for electronic applications in harsh high-temperature environments*, *IEEE Transactions on Industrial Electronics* **58**, 2673 (2011).
- [5] L.Y. Chen, G.W. Hunter, P.G. Neudeck, G.M. Beheim, D.J. Spry, and R.D. Meredith, *Packaging technologies for high temperature electronics and sensors*, in *Joint Conference 59th International Instrumentation Symposium and Machinery Failure Prevention Technology (MFPT 2013)*, 2013, 20130013849.
- [6] A.K. Panigrahi, T. Ghosh, S.R.K. Vanjari, and S.G. Singh, *Demonstration of sub 150°C Cu-Cu thermocompression bonding for 3D IC applications, utilizing an ultra-thin layer of Manganin alloy as an effective surface passivation layer*, *Materials Letters* **194**, 86 (2017).
- [7] M.V. Taklo, K. Schjolberg-Henriksen, N. Malik, E. Poppe, S. Moe, and T. Finstad,

- Al-Al wafer-level thermocompression bonding applied for MEMS*, in *5th International Workshop on Low Temperature Bonding for 3D Integration (LTB-3D 2017)*, 2017, pp. 11.
- [8] C. Liu, H. Hirano, J. Froemel, and S. Tanaka, *Wafer-level vacuum sealing using AgAg thermocompression bonding after fly-cut planarization*, *Sensors and Actuators A: Physical* **261**, 210 (2017).
- [9] Z. Wu, J. Cai, Q. Wang, J. Wang, and D. Wang, *Wafer-level hermetic package by low-temperature Cu/Sn TLP bonding with optimized Sn thickness*, *Journal of Electronic Materials* **46**, 6111 (2017).
- [10] V. Vuorinen, A. Rautiainen, H. Heikkinen, and M. Paulasto-Kröckel, *Optimization of contact metallizations for reliable wafer level Au-Sn bonds*, *Microelectronics Reliability* **64**, 676 (2016).
- [11] L.C. Wai, V.C. Nachiappan, S. Wickramanayaka, and C. Oetzel, *Chip to wafer hermetic bonding with flux-less reflow oven*, in *IEEE 18th Electronics Packaging Technology Conference (EPTC 2016)*, 2016, pp. 38-42.
- [12] Y. Li, Y. Xiao, W. Wang, L. Yin, and J. Zhang, *Effect of the viscosity of organic carrier on the quality of laser-assisted glass frit bonding*, in *17th International Conference on Electronic Packaging Technology (ICEPT 2016)*, 2016, pp. 1146-1150.
- [13] C. Zhao, J. Wang, S. M. Zhang, and J. B. Zou, *Glass frit as a hermetic joining material for bonding among three wafers with metallic film feed-through*, *Key Engineering Materials* **609-610**, 489 (2014).
- [14] J. Wang, X. He, X. Li, Y. En, and X. Zhang, *Hermetic packaging of Kovar alloy and low-carbon steel structure in hybrid integrated circuit (HIC) system using parallel seam welding process*, in *15th International Conference on Electronic Packaging Technology (ICEPT 2014)*, 2014, pp. 347-351.
- [15] X. Hu, M. Bauscher, P. Mackowiak, Y. Zhang, O. Hoelck, H. Walter, M. Ihle, S. Ziesche, U. Hansen, and S. Maus, *Characterization of anodic bondable LTCC for wafer-level packaging*, in *IEEE 18th Electronics Packaging Technology Conference (EPTC 2016)*, 2016, pp. 501-505.
- [16] X. Wang, Q. Xu, D. Xiao, Z. Hou, Z. Chen, and X. Wu, *Vertical signal feedthrough for sandwich devices based on anodic bonding and after laser trimming*, in *IEEE International Symposium on Inertial Sensors and Systems*, 2016, pp. 81-84.
- [17] A. Rautiainen, H. Xu, E. Österlund, J. Li, V. Vuorinen, and M. Paulasto-Kröckel,

- Microstructural characterization and mechanical performance of wafer-level SLID bonded Au-Sn and Cu-Sn seal rings for MEMS encapsulation*, Journal of Electronic Materials **44**, 4533 (2015).
- [18] H. Xu, V. Vuorinen, H. Dong, and M. Paulasto-Kröckel, *Solid-state reaction of electroplated thin film Au/Sn couple at low temperatures*, Journal of Alloys and Compounds **619**, 325 (2015).
- [19] L. Zhang, B. Jiao, W. Ku, L.T. Tseng, Y. Kong, Y.H. Chien, S. Yun, and D. Chen, *An electrical test method for quality detecting of wafer level eutectic bonding*, Journal of Micromechanics and Microengineering **27**, 015028 (2016).
- [20] E.C. Demir, M.M. Torunbalci, I. Donmez, Y.E. Kalay, and T. Akin, *Fabrication and characterization of gold-tin eutectic bonding for hermetic packaging of MEMS devices*, in *IEEE 16th Electronics Packaging Technology Conference (EPTC 2014)*, 2014, pp. 241-245.
- [21] F. Arabi, L. Theolier, D. Martineau, J.Y. Deletage, M. Medina, and E. Woïgard, *Power electronic assemblies: Thermo-mechanical degradations of gold-tin solder for attaching devices*, Microelectronics Reliability **64**, 409 (2016).
- [22] T.C. Chiu and K.L. Lin, *Current induced rapid phase transformation in Au/Sn reaction couple*, Journal of Alloys and Compounds **712**, 111 (2017).
- [23] S.Y. Zhao, X. Li, Y.H. Mei, and G.Q. Lu, *Study on high temperature bonding reliability of sintered nano-silver joint on bare copper plate*, Microelectronics Reliability **55**, 2524 (2015).
- [24] S.A. Paknejad and S.H. Mannan, *Review of silver nanoparticle based die attach materials for high power/temperature applications*, Microelectronics Reliability **70**, 1 (2017).
- [25] C. Weber, H. Walter, M.V. Dijk, M. Hutter, O. Wittler, and K.D. Lang, *Combination of experimental and simulation methods for analysis of sintered Ag joints for high temperature applications*, in *IEEE 66th Electronic Components and Technology Conference (ECTC 2016)*, 2016, pp. 1335-1341.
- [26] P. Altieri-Weimar, W. Yuan, E. Annibale, S. Schoemaker, D. Amberger, M. Göken, and H. Höppel, *Reliability model of LED package regarding the fatigue behavior of gold wires*, in *17th International Conference on Thermal, Mechanical and Multi-Physics Simulation and Experiments in Microelectronics and Microsystems (EuroSimE 2016)*, 2016, pp. 1-6.

- [27] F. Henaff, S. Azzopardi, E. Woirgard, T. Youssef, S. Bontemps, and J. Joguët, *Lifetime evaluation of nanoscale silver sintered power modules for automotive application based on experiments and finite-element modeling*, IEEE Transactions on Device and Materials Reliability **15**, 326 (2015).
- [28] Y. Wang, W. Zhao, M. Li, M. Chen, and L. Gao, *A simulation of intelligent power module under power cycling condition*, in *15th International Conference on Electronic Packaging Technology (ICEPT 2014)*, 2014, pp. 1015-1020.
- [29] L. Xu, M. Wang, Y. Zhou, Z. Qian, and S. Liu, *An optimal structural design to improve the reliability of Al_2O_3 -DBC substrates under thermal cycling*, Microelectronics Reliability **56**, 101 (2016).
- [30] L. Xu, Y. Liu, and S. Liu, *Modeling and simulation of power electronic modules with microchannel coolers for thermo-mechanical performance*, Microelectronics Reliability **54**, 2824 (2014).
- [31] T.G. Lei, J.N. Calata, G.Q. Lu, X. Chen, and S. Luo, *Low-temperature sintering of nanoscale silver paste for attaching large-area ($>100\text{ mm}^2$) chips*, IEEE Transactions on Components and Packaging Technologies **33**, 98 (2010).
- [32] Z. Zhang and G.Q. Lu, *Pressure-assisted low-temperature sintering of silver paste as an alternative die-attach solution to solder reflow*, IEEE Transactions on Electronics Packaging Manufacturing **25**, 279 (2002).

7

CONCLUSIONS AND RECOMMENDATIONS

7.1. CONCLUSIONS

In this thesis, a comprehensive research is performed on the sintering of silver nanoparticles under various sintering parameters. The pressure assisted nanosilver sintering technology is ideally suited for attaching power chips and serving to meet the demands of high strength and high temperature stability. The research conducted and presented in this thesis aims to provide fundamental knowledge and technical guidance for the application of pressure assisted nanosilver sintering technology in power electronics packaging. Specifically, the major conclusions are summarized as follows:

1. The sintering pressure demonstrates significant effect on enhancing the bonding strength of sintered silver nanoparticles. In this study, the effects of sintering pressure on the shear strength, fracture morphology and bonding mechanism of sintered silver nanoparticles are investigated. When the sintering pressure increases from 5 MPa to 10 MPa, the maximum increase rate of shear strength is obtained, resulting in the increase of shear strength from 44.2 MPa to 69.4 MPa. The further increase of sintering pressure shows limited effect on improving the shear strength in this study. As the sintering pressure increases from 5 MPa to 30 MPa, the fracture area of sintered package changes from the sintered Ag layer and its interface between molybdenum (Mo) to the surface metallization layer on Mo. This result indicates that the bonding strength of sintered silver nanoparticles is greatly enhanced at 30 MPa pressure. However, the sintering temperature and time exhibit insignificant effect on improving the bonding strength of sintered silver nanoparticles because of the assistance of sintering pressure.

Comparing with the pressure free sintering process, the pressure assisted sintering produces more and larger sintering necks, which furtherly lead to a better bonding quality and performance.

2. The increase of sintering pressure improves the resistance to plastic deformation and creep of nanosilver sintered joint. In this study, the nanoindentation test is conducted to investigate the indentation hardness, plasticity and initial creep properties of pressure sintered nanosilver joint at various test temperatures. The strain rate exhibits limited effect on the indentation hardness as it reaches 0.2 s^{-1} . The yield stress of nanosilver sintered joint is improved with the increase of sintering pressure from 5 MPa to 30 MPa. Furthermore, the strain hardening exponent becomes larger in higher pressure sintered nanosilver joint. This result indicates that the resistance to plastic deformation of nanosilver sintered joint can be enhanced by increasing the sintering pressure. The plastic stress-strain constitutive equations of nanosilver sintered joint at different sintering pressures are gained. The maximum indentation depth of nanosilver sintered joint increases when the test temperature increases from 25°C to 200°C . However, the decrease trend is found in maximum indentation depth as the sintering pressure increases from 5 MPa to 30 MPa. The indentation hardness of nanosilver sintered joint decreases with increasing test temperature from 140°C to 200°C , but increases with increasing sintering pressure from 5 MPa to 30 MPa. The evolution of indentation modulus exhibits similar trend as the indentation hardness with increasing temperature and pressure. The initial creep is observed in nanosilver sintered joint at temperatures range from 140°C to 200°C . The maximum creep displacement exhibits increase trend with the increase of temperature. In addition, the difference of maximum creep displacement between 140°C and 200°C becomes smaller in 30 MPa sintered joint when comparing with 5 MPa sintered one. The increase of sintering pressure improves the resistance to creep of nanosilver sintered joint.

3. The designed nanosilver sintering technology is successfully employed in fabricating the double side sintered power package. In this study, the effects of sintering pressure on the sintering behavior of silver nanoparticles and mechanical properties of nanosilver double side sintered power package are investigated. The sintering pressure exhibits obvious effect on enhancing the shear strength of sintered package with increasing sintering pressure from 5 MPa to 20 MPa. The fracture area of 5 MPa sintered package is between the sintered Ag layer and the surface metallization layer on FRD die, which implies a weak bonding. As the sintering pressure increases to 20 MPa, the fracture area changes to the sintered Ag layer and the FRD. This result indicates that the sintering pressure higher than 5 MPa is quite effective on improving the bonding of sintered silver nanoparticles. However, the sintering pressure over 20 MPa is not highly recommended

for the manufacturing process. Besides, three sintering sequences are proposed, namely S(a), S(b) and S(c). In sintering sequence S(a), the power chip is first sintered onto the bottom Mo plate, and then the top Mo plate is sintered onto the chip with the bottom Mo plate. As for sintering sequence S(b), the top Mo plate is first sintered onto the power chip and then they are sintered onto the bottom Mo plate. In sintering sequence S(c), the bottom Mo, the chip, and the top Mo are sintered in one step. Combining the experimental results and the simulations results, the S(a) is highly recommended for the mass production of nanosilver double side sintered power packages. Since the S(a) demonstrates the highest yield rate and also the lowest maximum von Mises stress on chip.

4. The nanosilver sintering process is designed and employed in the ceramic packaging. In this study, the effects of lid material on the bonding properties and stress distribution of nanosilver sintered ceramic package are investigated. The sintered Ag layer in Cu lid sintered cavity shows serious delamination while no visible crack or delamination is observed in Si lid sintered cavity. Since the Si lid has a higher Young's modulus and a lower CTE than the Cu lid, so less residual stress is generated in Si lid and ensures its high bonding quality. Based on the simulation results, the Cu lid sintered cavity has a much higher von Mises stress than the Si lid sintered one. In addition, the stress concentration area on Cu lid is much larger than the Si lid. The simulation results prove the experimental observations. The stress distribution area and the maximum von Mises stress on Cu lid are slightly affected by the increase of sintering pressure. However, as the sintering pressure increases from 5 MPa to 30 MPa, the stress distribution area on Si lid stretches from the corner to the area of the whole sintered Ag layer. Besides, the maximum von Mises stress on Si lid increases with increasing sintering pressure. The Si lid sintered cavity shows a much lower von Mises stress than the Cu lid sintered one at different sintering pressures.

7.2. RECOMMENDATIONS

The work presented in this thesis provides the basis for employing pressure assisted sintering in fabricating the power packages. Although nanosilver films have gained a high popularity in power electronics packaging, significant efforts are still needed to make this promising technology prosperous in a wider range of applications. Thus, recommendations are given as follows:

1. The detailed burnout characteristics and mechanisms of organics inside the nanosilver film are not clear. The thermal decomposition of organics inside the nanosilver film plays an important role in determining the properties of sintered layer,

which could be a concern for the over-time degradation during operation.

2. The volume shrinkage mechanism of sintered silver nanoparticles needs further studies. The shrinkage of silver nanoparticles during sintering may induce stress in chip and increase the failure rate, especially for the pressure free sintering process.

3. Future work should be conducted on the evolution of pores inside the sintered silver layer during service process and its corresponding effect on the reliability.

4. The interfacial reactions and mechanisms between silver nanoparticles and surface metallization layers on substrate/chip are not clear and need to be focused in future investigations.

5. Last but not least, the construction of lifetime prediction models for nanosilver sintered package at various sintering parameters is somewhat lacking though they are expected to be the same as for solder alloys.

SUMMARY

High power electronics with wide band gap semiconductors are becoming the most promising devices in new energy power suppliers and converters. Highly reliable die attach materials, serving as one of interconnections, play critical roles in power electronic packages and modules. Among which, the nanosilver paste/film has become a promising die attach material with main advantages of a high thermal and electrical conductivity, as well as high temperature stability. Previous works are mostly focusing on the pressure free sintered silver nanoparticles. However, some drawbacks, such as low bonding strength and high porosity, have reduced the reliability of sintered joint and limited the wide application of this technology. Alternatively, pressure assisted sintering has exhibited great advantages in enhancing the bonding quality of nanosilver sintered joint. But the sintering properties of pressure sintered silver nanoparticles and the application of this technology in power electronics packaging are still lacking. In this thesis, a comprehensive research is performed on the pressure assisted sintering of silver nanoparticles, and the results are summarized below.

Chapter 1 reviews the mainstream die attach materials and technologies that are used for power electronic packages and modules. Those technologies include lead free soldering, transient liquid phase (TLP) bonding and nanosilver sintering. Firstly, the fabrication of lead free solders, typical soldering technology and several high temperature solder alloys are introduced. Then the formation of intermediate metal layers, bonding process and main material systems for TLP bonding technology is discussed. Next, the synthesis of nanosilver paste, main sintering technology and silver sintering materials are presented. Besides, a comprehensive comparison of these three technologies is summarized by using typical representatives of their own.

Chapter 2 considers the evolution of mechanical properties of the nanosilver sintered sandwich package at various sintering parameters. The shear test is conducted to evaluate the bonding strength of sintered package. The effects of sintering pressure, temperature and time on the improvement of shear strength are discussed respectively. The results reveal that the sintering pressure demonstrates a significant effect on enhancing the shear strength of sintered package. Meanwhile, the bonding mechanism of silver nanoparticles at each sintering parameter is analyzed accordingly.

Chapter 3 focuses on the micro mechanical properties of pressure assisted sintered

nanosilver joint. The effect of strain rate on the indentation hardness is studied and a proper strain is selected for the subsequent tests. The plastic stress-strain constitutive equations of pressure assisted sintered nanosilver joint are obtained at room temperature. Both of the indentation hardness and elastic modulus of nanosilver sintered joint decrease with increasing temperature from 140°C to 200°C, but decrease with increasing sintering pressure from 5 MPa to 30 MPa. Besides, the resistance to creep of nanosilver sintered joint can be enhanced by increasing the sintering pressure.

Chapter 4 focuses on the realization and characterization of nanosilver double side sintered power package. The effects of sintering pressure on the sintering behavior and properties of silver nanoparticles are analyzed. With the help of pressure, the sintered silver nanoparticles show a denser structure when comparing with the pressure free sintered ones. Moreover, the shear strength of nanosilver double side sintered package is improved by increasing the sintering pressure from 5 MPa to 30 MPa. In addition, the change of fracture area with the increase of sintering pressure verifies the enhanced bonding of sintered silver nanoparticles.

Chapter 5 focuses on the stress distribution of nanosilver double side sintered package after different sintering sequences. The experimental test and finite element analysis are used together to validate the optimal sintering sequence employed in this study. The experimental results show that the package sintered by S(a) shows the highest yield rate among the three sintering sequences. Based on the simulation works, the S(a) sintered package has a lower stress distribution on chip when comparing with S(b) and S(c) sintered ones. The experimental results are in good agreement with the simulation results and proves that the S(a) could be the optimal sintering process for the mass production in this study.

Chapter 6 studies on the application of nanosilver sintering technology in ceramic packaging and its corresponding sintering stress analysis. The Cu lid and Si lid are sintered to the ceramic cavity using nanosilver film with the help of sintering pressure. The bonding quality is studied by the X-ray and C-SAM tests. The nanosilver sintered layer in Si lid sintered cavity shows a better bonding performance when comparing with the Cu lid sintered one. According to the simulation results, the stress distribution on Si lid has a much lower value and a smaller stress concentration area. Furthermore, the sintering pressure exhibit limited effect on the stress level and distribution of Cu lid sintered cavity. The von Mises stress on Si lid sintered cavity increases with increasing the sintering pressure, but the value is still lower than the Cu lid sintered one.

In Chapter 7, the general concluding remarks are given. On the other hand, some future challenges and development directions are recommended in this chapter.

SAMENVATTING

Vermogenselektronica van halfgeleiders met een grote bandafstandsenergie worden veelbelovende apparaten in nieuwe energie bronnen en omvormers. Zeer betrouwbare hechtmaterialen voor chips, dienend als een van de verbindingen, spelen een kritieke rol in behuizingen en modules voor vermogenselektronica. Hieronder zijn nano-zilver pasta en films veelbelovende kandidaten geworden als hechtmateriaal voor chips, met de belangrijkste voordelen van zowel een hoge thermische en elektrische geleiding, als een hoge temperatuur stabiliteit. Eerder werk is voornamelijk gefocust op druk-vrij gesinterde zilveren nanodeeltjes. Echter, enkele nadelen zoals een lage bindingskracht en een hoge mate van porositeit, hebben de betrouwbaarheid van een gesinterde verbinding verminderd en het grote toepassingsbereik van deze technologie beperkt. Anderzijds heeft druk geassisteerd sinteren grote voordelen vertoond in het verbeteren van de bindingskwaliteit van gesinterde nano-zilver verbindingen. Echter blijven de sinter eigenschappen van onder druk gesinterde zilveren nanodeeltjes en de toepassing van deze technologie in vermogenselektronica nog steeds achter. Voor dit thesis is een uitgebreid onderzoek uitgevoerd naar het druk geassisteerd sinteren van zilveren nanodeeltjes. De resultaten van de hoofdstukken zijn hieronder samengevat.

Hoofdstuk 1 bespreekt de reguliere hechtmaterialen voor chips en de technologieën welke worden gebruikt voor vermogenselektronica componenten en modules. Tot deze technologieën behoren loodvrij solderen, kortstondig-vloeibaar-fase-hechten (TLP) en nano-zilver sinteren. Ten eerste zijn de fabricage van loodvrije soldeer, typische soldeer technologieën en enkele hoge temperatuur soldeer legeringen geïntroduceerd. Vervolgens zijn de formatie van overgangsmetaal lagen, het bindingsproces en de belangrijkste materiaal systemen voor TLP bindingstechnologie besproken. Hierna zijn de synthese van nano-zilver pasta, de belangrijkste sinter technologie en materialen voor zilver sinteren gepresenteerd. Daarnaast is een uitvoerige vergelijking tussen deze drie technologieën samengevat door gebruik te maken van hun eigen vertegenwoordigers.

Hoofdstuk 2 beschouwt de evolutie van de mechanische eigenschappen van de nano-zilver gesinterde sandwich behuizing bij verschillende sinter parameters. De afschuiftest is uitgevoerd om de bindingsterkte van de gesinterde behuizing te evalueren. De effecten van sinterdruk, temperatuur en tijd op de verbetering van de afschuifsterkte zijn besproken. De resultaten brengen aan het licht dat de sinterdruk een significant

effect heeft op de verbetering van de afschuifsterkte van de gesinterde behuizing. Tegelijkertijd is het bindingsmechanisme van zilveren nanodeeltjes dienovereenkomstig voor elke sinter parameter geanalyseerd.

Hoofdstuk 3 focust zich op de micro mechanische eigenschappen van druk geassisteerd sinteren van een nano-zilver verbinding. Het effect van de reksnelheid op de indringhardheid is onderzocht en een passende rek is geselecteerd voor opvolgende testen. De constitutieve vergelijkingen voor de plastische spanning-rek karakteristiek van druk geassisteerde gesinterde nano-zilver verbindingen zijn verkregen bij kamertemperatuur. Zowel de indringhardheid als de elasticiteitsmodulus van een nano-zilver gesinterde verbinding nemen toe met toenemende temperatuur van 140°C tot 200°C, echter nemen af met toenemende sinterdruk van 5 MPa tot 30 MPa. Daarnaast kan de weerstand tot deformatie van nano-zilver gesinterde verbindingen worden vergroot door een toename van de sinterdruk.

Hoofdstuk 4 focust zich op de realisatie en karakterisatie van een vermogens behuizing welke dubbelzijdig is gesinterd met nano-zilver. De effecten van de sinterdruk op het sintergedrag en de eigenschappen van zilveren nanodeeltjes zijn geanalyseerd. Met behulp van druk vertonen de gesinterde nanodeeltjes een dichtere structuur vergeleken met de drukvrij gesinterde versies. Bovendien is de afschuifsterkte van de dubbelzijdig nano-zilver gesinterde behuizing verbeterd door een toename van de sinterdruk van 5 MPa tot 30 MPa. Verder verifieert de verandering van het breukvlak met de toename van de sinterdruk de verbeterde binding van zilveren nanodeeltjes.

Hoofdstuk 5 focust zich op de spanningsverdeling van de dubbelzijdig nano-zilver gesinterde behuizing na verschillende sinter volgordes. De experimentele test en de eindige elementen analyse zijn in deze studie samen gebruikt om de optimale sintervolgorde te valideren. De experimentele resultaten laten zien dat de behuizing gesinterd door S(A) de hoogste opbrengst van de drie sintervolgordes vertoont. Gebaseerd op de simulatie werkzaamheden, de S(a) gesinterde behuizing heeft een lagere spanningsverdeling op de chip vergeleken met de S(b) en de S(c) gesinterde versies. De experimentele resultaten zijn in goede overeenstemming met de simulatie resultaten en bewijzen dat de S(a) het optimale sinterproces zou kunnen zijn voor de massafabricage in deze studie.

Hoofdstuk 6 bestudeert de toepassing van nano-zilver sintertechnologie in keramische behuizingen en zijn dienovereenkomstige sinter spanning analyse. De Cu deksel en de Si deksel zijn gesinterd naar een keramische uitsparing gebruik makend van een nano-zilver film en met behulp van sinterdruk. De kwaliteit van de verbinding is onderzocht door X-ray en C-SAM testen. De nano-zilver gesinterde laag van Si deksel

naar de gesinterde uitsparing vertoont een betere bindingsprestatie vergelijken met de Cu deksel gesinterde versie. Overeenkomstig met de simulatie resultaten heeft de spanningsverdeling op de Si deksel een veel lagere waarde en een kleinere spanningsconcentratie oppervlakte. Verder vertoont de sinterdruk een gelimiteerd effect op het spanningsniveau en verdeling van de gesinterde Cu deksel. De Von Mises spanning op de gesinterde Si deksel naar de uitsparing neemt toe met toenemende sinterdruk, maar de waarde is nog altijd lager dan de gesinterde Cu deksel variant.

In hoofdstuk 7 zijn de algemene concluderende opmerkingen omschreven. Tevens worden enige toekomstige uitdagen en richtingen voor verdere ontwikkeling aanbevolen in dit hoofdstuk.

ACKNOWLEDGEMENTS

Firstly, I want to express my sincere gratitude to my promotor Prof. Guoqi Zhang for providing me the chance to pursue my doctoral degree in TU Delft. His continuous support and infinite patience help me to achieve each goal in my PhD study. He encourages me to develop the teamwork and leadership awareness when doing my research. These important capabilities benefit me on both scientific research and career development. He is the person to connect academia and industry and bring many valuable thoughts into commercialization. He also provides many opportunities for students to cooperate with technical companies. And I'm the lucky one to work and study in Boschman Technologies, where I initialize my research. I appreciate his great assistance in helping me overcoming each obstacle I have been facing through my research.

My sincere thanks go to my co-promotor Prof. Xuejun Fan, from Lamar University, for enlightening me the first glance of research. I admire his attitude and enthusiasm on scientific research. He is always willing to share his professional knowledge with me during our discussions. He is not only guiding my experimental works, but also helping me in exploring the scientific values of my research. He gives me a lot of valuable and meaningful feedback on modifying my papers. It's my honor to get the chance to study under his supervision.

My special thanks also go to Prof. Fenglian Sun, from Harbin University of Science and Technology. She is the first person who brings me into the field of scientific research and also provides me the opportunity to study with Prof. Guoqi Zhang. She is quite strict in scientific research while she is very kind in daily life. When I get stuck in my study, the sentence first comes to my mind is her inspiration, "I totally believe in you and of course you have the ability to complete the research very well". Great thanks to her for making me become a more confident and open-minded person.

I am grateful to Dr. Yang Liu, from Harbin University of Science and Technology. Notably, he provides me the first courage to start my PhD study in 2015. We have worked together on a same project in the Netherlands. During which, his positive attitude on various kinds of things deeply influences me and gives me the power to achieve the best of myself. He helps me a lot in fabricating the samples used in this thesis and also assisting me in revising my papers.

I am also grateful to Dr. Lingen Wang, from Boschman Technologies. He is an excellent project manager in pressure assisted nanosilver sintering area. He gives me the opportunity to lead a developing project and provides me many technical suggestions. Meanwhile, he helps me to get the financial support on the accommodation during my study in the Netherlands. Moreover, he taught me many experiences on seeking the wisdom in one's life, which has benefited me a lot.

I send my great thanks to my supervisors Dr. Jiajie Fan, Dr. Jing Zhang and Dr. Cheng Qian. They have spent a lot of time in coaching me in my research works. I want to give my appreciations to Dr. Jiajie Fan first. He is very nice and patient on improving my paper writing skills. We also have a lot of long discussions on my research and he always shares his knowledge without reservation. In addition to the scientific research, he is also very kind to help me in solving the problems I met in other aspects. Besides, I'm feeling so lucky to have Dr. Jing Zhang as my daily supervisor. The period that I have worked with him is the fastest stage for me to grow up in PhD development. He helps me to establish the weekly summarization and preparation mechanism, which improves my work efficiency obviously. I also appreciate his selfless help in my experiments. Also, I owe sincere thankfulness to Dr. Cheng Qian for improving my negotiating skills and the scientific writing skills.

I am also grateful to Prof. Willem Van Driel, from TU Delft and Signify. He has a strong sense of responsibility in helping me to finish my thesis writing. His feedback is very quick, and his instructions are insightful.

I also want to send my thanks to my best friends, Mr. Shengxiang Wan from Harbin Institute of Technology, and Mr. Bo Jiang from Harbin University of Science and Technology. They provide me selfless help in many experimental tests in this thesis. Also, they are the trustworthy person for me to rely on when I'm facing difficulties.

My great thanks also go to Mr. Frank Boschman and Mr. Eef Boschman, from Boshman Technologies, for providing me a position in their company, and the financial support on my tests as well as my accommodation. I thank Mr. Mike Hoedemaker for his kind instructions on my mold design. I also want to thank Mrs. Monica Teunissen and Mr. Theo Nijhuis and other colleagues in the company, for providing me a joyful work environment as well as helping me in finishing my works.

I want to thank Dr. Francois Le Henaff, from Alpha Assembly Solutions, for his assistance in fabricating the laser cut nanosilver film and some relevant experiments.

I really appreciate the great helps from Dr. Mingzhi Dong and Dr. Jianlin Huang. They are just like my elder brothers and give me selfless help in many aspects. They also

help me to adapt myself to the life in the Netherlands. I also thank my other BRC colleagues, Hongyu Tang, Yuan Gao, Jianwen Sun, Fengze Hou, Guangjun Lu and Bo Sun. It's my pleasure to meet you all and get the chance to work in a same group.

My sincere appreciation also goes to my colleague Boyao Zhang, from TU Delft. She is an outstanding PhD candidate and also a nice friend. We have many stimulating discussions on our researches. I also want to thank her for helping me fabricating the silicon lids.

I also send my great thanks to Xandra Tober and Marian Roozenburg for helping me in the registration of my PhD as well as visa application. In addition, it's my pleasure to work with so many excellent colleagues in the group of Prof. Guoqi Zhang: Dr. Henk van Zeijl, Dr. Rene Poelma, Dr. Pan Liu, Dr. Pengfei Sun, Dr. Huaiyu Ye, Dr. Zahra Kolahdouz Esfahani, Robert Sokolovskij, Yelena Grachova, Xueming Li, Jian Li, Hengqian Yi, Zhen Cui, Brahim Mansouri, Luke Middelburg, Manjunath Ramachandrappa Venkatesh, Alexandru Prisacaru, Tianyi Jin and Joost van Ginkel.

Many thanks to the international cooperation program of Beijing Research Center of TU Delft. They have provided many accessible resources and chances for students in European and China to learn about the latest knowledge from both academy and industry. Also, I want to thank the China Solid State Lighting Alliance and State Key Laboratory of Solid State Lighting (Changzhou Base, China), for their supporting of my PhD project. I also want to express my thanks to the financial support of the National High-Tech Research and Development Program of China (863 Program, 2015AA033304).

My special thanks also go to Luke Middelburg from TU Delft for his assistance in preparing my Dutch version of the summary and the propositions of this thesis.

I want to thank all the other professors, colleagues and friends who I have worked with, for your selfless contribution to my thesis. I could not imagine how I can finish this thesis so successful without your kind help. Even though I may not get the chance to express my personal thanks, I will remember your help and friendship forever.

At last, I want to express my sincere love and thankfulness to my family. Thanks for their continuous support and encouragement during my PhD study. It's so good to have you all together and you mean a lot to me.

LIST OF PUBLICATIONS

JOURNAL PAPERS

1. **H. Zhang**, Y. Liu, L. Wang, F. Sun, X. Fan, G.Q. Zhang. *Indentation hardness, plasticity and initial creep properties of nanosilver sintered joint*. [Results in Physics](#) **12**, 712 (2018).
2. **H. Zhang**, Y. Liu, L. Wang, F. Sun, J. Fan, M.D. Placette, X. Fan, G.Q. Zhang. *Effects of sintering pressure on the densification and mechanical properties of nanosilver double side sintered power module*. [IEEE Transactions on Components, Packaging and Manufacturing Technology](#), **9**, 963 (2019).
3. **H. Zhang**, Y. Liu, L. Wang, J. Fan, X. Fan, F. Sun, G.Q. Zhang. *A new hermetic sealing method for ceramic package using nanosilver sintering technology*. [Microelectronics Reliability](#) **81**, 143 (2018).
4. Y. Liu, **H. Zhang**, L. Wang, X. Fan, G.Q. Zhang, F. Sun. *Effect of sintering pressure on the porosity and the shear strength of the pressure-assisted silver sintering bonding*. [IEEE Transactions on Device and Materials Reliability](#) **18**, 240 (2018).
5. Y. Liu, **H. Zhang**, L. Wang, X. Fan, G.Q. Zhang, F. Sun. *Stress analysis of pressure-assisted sintering for the double-side assembly of power module*. [Soldering & Surface Mount Technology](#) **31**, 20 (2019).
6. Y. Liu, **H. Zhang**, Z. Li, L. Wang, G.Q. Zhang, F. Sun. *Investigation of the microstructure of pressure-assisted Ag sintering layer by deep-etching method*. [Rare Metal Materials and Engineering](#), **Accepted**, 2018.

CONFERENCE PAPER

1. **H. Zhang**, J. Fan, J. Zhang, C. Qian, X. Fan, F. Sun, G.Q. Zhang. *Reliability optimization of gold-tin eutectic die attach layer in HEMT package*. In [China International Forum on Solid State Lighting \(ChinaSSL 2016\)](#), 2016, pp. 52-56.

CURRICULUM VITÆ

Hao ZHANG

09-02-1993 Born in Changtu, China

EDUCATION

- 2015–2019 PhD in Microelectronics
Delft University of Technology, Delft, the Netherlands
Thesis: Investigation of Pressure Assisted Nanosilver Sintering
Process for Application in Power Electronics
Promotor: Prof. dr. Guoqi Zhang
- 2013–2015 Master in Materials Processing Engineering
Harbin University of Science and Technology, Harbin, China
Thesis: Study on the Modification and Mechanism of
Nanoparticles doped Sn58Bi/Cu Micro Solder Joints
Promotor: Prof. dr. Fenglian Sun
- 2009–2013 Undergraduate in Materials Processing and Controlling Engineering
Harbin University of Science and Technology, Harbin, China

RESEARCH EXPERIENCE

- 2016–2017 Research and Development Engineer
Boschman Technologies, Duiven, the Netherlands
- 2015–2016 Electronic Packaging Engineer
State Key Laboratory of Solid State Lighting, Changzhou, China